UNIVERSITÀ DEGLI STUDI DI BERGAMO

PROCEEDINGS OF THE DIPSI WORKSHOP 2011

Droplet Impact Phenomena & Spray Investigations

Double drop impact onto liquid pool. View from below.

BERGAMO, ITALY, 27TH MAY 2011

UNIVERSITÀ DEGLI STUDI DI BERGAMO

PROCEEDINGS OF THE DIPSI WORKSHOP 2011

Droplet Impact Phenomena & Spray Investigations

BERGAMO, ITALY, 27TH MAY 2011

PROCEEDINGS OF THE DIPSI WORKSHOP 2011
Droplet Impact Phenomena & Spray Investigations

Editors
Gianpietro Elvio Cossali and Simona Tonini
Industrial Engineering Department
Università degli Studi di Bergamo
Viale Marconi 5, 24044 Dalmine, Italy
e-mail: elvio.cossali@unibg.it
simona.tonini@unibg.it

p. 86 - cm 29,7
ISBN – 978 88 97413 03 5

Preface

This CD contains the papers presented at the DIPSI Workshop 2011 on Droplet Impact Phenomena and Spray Investigation, organised by the Università degli Studi di Bergamo on Friday 27th May 2011 in Bergamo, Italy.

This workshop, which is now at its fifth edition, represents an important opportunity to share the recent knowledge on droplets and sprays in a variety of research fields and industrial applications.

The support and sponsorship of the Department of Industrial Engineering of the Università degli Studi di Bergamo, the Italian research program PRIN2007, LaVision GmbH, Luchsinger s.r.l. and all the other participating are acknowledged and appreciated.

Bergamo, October 2011

Prof. Gianpietro Elvio Cossali

Main Sponsors

UNIVERSITÀ DEGLI STUDI DI BERGAMO
www.unibg.it

MIUR
www.prin.miur.it

LAVISION
www.lavision.de

LUCHSINGER
www.luchsinger.it

Contents

EXPERIMENTAL AND NUMERICAL CHARACTERIZATION OF HIGH-PRESSURE SPRAYS FOR GDI ENGINES

L. Allocca (*), A. Montanaro (*), T. Lucchini (°), F. Brusiani (†)

(*) Istituto Motori CNR - Napoli, Italy
(°) Politecnico di Milano - Dipartimento di Energia, Italy
(†) Università degli Studi di Bologna, Italy

ABSTRACT

Direct-injection is now widely applied in spark-ignition engines in combination with turbocharging to reduce the fuel-consumption and the knock risks. This is achieved through the use of multi-hole, high-pressure injectors whose features are rather different with respect to the hollow-cone, low-pressure configurations that were adopted in the last decade. This last aspect has to be taken into account when multi-dimensional simulations of GDI engines have to be performed. In particular, suitable models are needed to describe the spray atomization and the wall-impingement processes.

In this paper experimental investigations were performed using a 6-hole injector in a constant-volume vessel with optical access. Spray images were acquired by a CCD camera and processed to obtain the spray penetration and cone angles for the different tested operating conditions. The effects of injection pressure were evaluated in the range 3.0 – 20 MPa at ambient density of the gas. A flat plate was added to the experimental apparatus for investigation of the spray-wall impingement and liquid-film images were acquired. On the basis of the experimental database, a CFD methodology for gasoline spray simulations was implemented into the Lib-ICE code, developed under the OpenFOAM technology. The evolution of the resulting liquid film was also taken into account by solving the mass and momentum equations on the mesh boundary.

.

INTRODUCTION

In the field of SI-engines, attention is mainly focused on Direct Injection (GDI) because it allows to improve the overall engine thermal efficiency and the engine response during load variations. A significant reduction of the knock tendency is also ensured and this is a relevant aspect when turbocharging is used [1, 2]. GDI technology allows the reduction of HC and CO emissions especially at cold start (warm-up period) and transient modes when the engine works at lean-mixture conditions. To take advantage of all the theoretical benefits derived from GDI applications, it is necessary to work with a large stratification region in the engine map and this requires a strong control of the air/fuel mixing process.

The most widely used GDI injector configuration is the multi-hole mini-sac injector which is used to deliver fuel during the intake and compression strokes, with pressures ranging from 1 to 20 MPa [3]. The fuel/air mixture distribution is the result of complex interactions between the emerging fuel spray, in-cylinder flow field and the combustion chamber geometry [4]. Hence, experimental and numerical investigations are needed to evaluate how the spray evolution is influenced by nozzle design and spray targeting [5], injection pressure [6] and the interaction between spray and cylinder/piston walls [7].

In particular, multi-dimensional models are widely applied to real engine geometries to define suitable injector configurations and strategies for a wide range of operating conditions. The well-known Eulerian-Lagrangian approach is used to model the fuel spray, which is composed by a discrete set of computational parcels and their evolution depends on the exchange of mass, momentum and energy with the continuous gas phase. Additional sub-models are also required to take into account the liquid jet atomization, droplet evaporation, heat transfer, breakup, collision and wall impingement [8].

In this work, experiments and calculations were performed to understand the behavior of a gasoline spray emerging from a six-hole injector mounted on the top of an optically accessible vessel. This investigation was performed to provide a reliable CFD methodology to simulate these jets. Different injection pressures were considered, ranging from 3 to 20 MPa and the injected mass flow rate was measured for each operating conditions. A CCD camera was used to acquire the spray images that were then digitally processed to measure the spray penetration and cone angles. Impinging conditions were also reproduced in the experiments by introducing a plate in the vessel orthogonally oriented with respect to a reference jet.

The proposed CFD approach was implemented by the authors into the Lib-ICE code [9, 10], which is a set of libraries and applications for engine modeling developed under the OpenFOAM® technology [11]. Specific modules are available for the simulation in in-cylinder processes (Diesel and HCCI combustion, motion of piston and valves, complex chemistry with adaptive tabulation, gas and particulate emissions, spray break-up and spray-wall interaction). In previous works, Lib-ICE was applied to simulate the fuel-air mixing process in Diesel and PFI engines [12, 13]. A simplified 1-D model of the nozzle flow was used to estimate the influence of cavitation on the liquid jet diameter and velocity while the primary and secondary liquid jet break-up processes were modeled according to the Kelvin-

(*) corresponding author: l.allocca@im.cnr.it – tel +39 081 7177152 – fax +39 081 2396097

Helmoltz theory. A specific spray sub-model describes the interaction between the fuel spray and the cylinder walls under different impinging conditions and the evolution of the resulting liquid film is also taken into account by solving its mass, momentum and energy equations on the mesh boundary.

EXPERIMENTAL APPARATUS

The GDI injector considered in the present work was the mini-sac six-holes Bosch HDEV 5.1 with solenoid actuation. This injector is characterized by a hole diameter of 0.193 mm and a range of application between 5.13 and 17.1 g/s of delivered fuel for an injection pressure of 10 MPa. On a plane perpendicular to the injector axis, the six jet directions give a spray footprint characterized by a hollow-ellipsoid shape.

To avoid interference and contamination with the surrounding ambient, the fuel was discharged from the injector into a quiescent vessel filled with air kept at atmospheric pressure (0.1 MPa) and room temperature. The high pressure for the injections was generated by a hydro-pneumatic pump, instead of the classic rotating pump, activated by pressured gas (air) ranging from 0.07 MPa to 0.7 MPa. The injector was driven by a Programmable Electronic Control Unit (PECU) able to manage multi-injection strategies with the needle opening time defined through the injector energizing period. The injection flow rate was measured by an AVL Meter operating on the Bosch principle [14,15]. During the experimental tests the injection pressure range from 3 MPa to 20 MPa was considered and it corresponded to a delivered fuel quantity ranging between 10 and 100 mg/stroke.

During the experiments, pictures of the emerging spray were taken using a synchronized CCD camera characterized by 1376x1040 pixels, 12 bit resolution, and 0.5 μs shutter time. A wet seal spherical holder enabled the tilting of the injector in an angular range of +/- 15°, with respect to its axis. It allowed the perpendicular alignment between the direction of one spray and the CCD optical axis, therefore the parallax error was reduced. The spray pictures were taken at different instants starting from SOI and they were post-processed by software to extract the main parameters characterizing the dynamic of the spray: cone angle and liquid penetration. In particular, these quantities were measured only on one of the six jets emerging from the injector. At this scope the jet characterized by the smallest interactions with the other jets was chosen. More details about image post-processing procedure can be found in [16].

Finally, a stainless steel flat plate was introduced into the vessel to reproduce the spray-wall impingement. The plate was located at 40 mm from the nozzle tip thanks to a X-Y-Φ micrometric apparatus. The plate axis was parallel the axis of the less interacting jet, fully framed by the CCD camera. The plate was at same room temperature of the gas filling the vessel. The authors decided to perform also spray impact analysis because, as well known, for GDI engines the wall film liquid formation on the combustion chamber walls during the compression strokes could be a very significant problem because it has a strong influence on the air/fuel mixing process, therefore on the combustion performance and pollutant formation. For this reason a correct prediction of wall film (generation and evolution) is of great importance for GDI engine simulations. For all the experimental tests, a standard (commercial) gasoline was used as fuel.

NUMERICAL MODELS

The modeling requirements that have to be satisfied to perform a spray simulation are quite high because during the injection the jets outgoing the injector nozzles are simultaneously subjected to many phenomena: primary atomization, secondary break-up, collision/coalescence and wall-impingement. In the following sections, the spray sub-models implemented in the Lib-ICE code are presented.

Breakup model

To define the droplet velocity components at nozzle exits, the Huh-Gosman [17] theory was considered. A quasi-dimensional turbulence model was used to compute the turbulent kinetic energy (k_{d0}) and dissipation rate (ε_{d0}) of the emerging liquid jet, which were initialized according to the flow conditions inside the nozzle:

$$k_{d0} = \frac{U_D^2}{8L_{nozz}/D_{nozz}}\left[\frac{1}{C_d^2} - K_c - (1-s^2)\right] \tag{1}$$

$$\varepsilon_{d0} = K_\varepsilon \frac{U_D^3}{2L_{nozz}}\left[\frac{1}{C_d^2} - K_c - (1-s^2)\right] \tag{2}$$

where C_d is the discharge coefficient and K_c - K_ε are two model constants respectively set to 0.47 and 0.23. L_{noz} and D_{noz} are the geometric length and diameter of the injector nozzle. U_d is the droplet velocity at nozzle exit and s the area ratio at the contraction corner.

From k_{d0} and ε_{d0} it was possible to estimate the turbulent length and time scales L_{t0} and τ_{t0} at the time the blob leaves the nozzle:

$$L_{t0} = C_\mu \frac{k_{d0}^{1.5}}{\varepsilon_{d0}},\ \tau_{t0} = C_\mu \frac{k_{d0}}{\varepsilon_{d0}} \tag{3}$$

C_μ is a constant whose value is equal to 0.09. The spray cone angle, α, is then estimated as:

$$\tan\left(\frac{\alpha}{2}\right) = \frac{C_1 \cdot L_{t0}}{C_3 \cdot \tau_{t0}} \tag{4}$$

Where the values of the model constants C_1 and C_3 were set to 2.0 and 1.2 respectively [17].

Since the injection pressure in GDI engines usually ranges from 5 MPa to 20 MPa, the resulting droplet Weber number at the nozzle exit is generally lower than 1000, which was fixed as threshold between turbulence-induced and aerodynamic-induced breakup [12, 18]. For this reason, the Kelvin-Helmoltz instability was chosen to be the dominant mechanism governing both the primary and secondary droplet break-up [19]. The diameter reduction of the injected blobs was computed as:

$$\frac{dD_d}{dt} = -\frac{D_d - D_{new}}{\tau_{BU}} \quad (5)$$

where D_d is the current droplet diameter, D_{new} is the diameter of the child drops and τ_{BU} is the break-up time. These values were computed according to the most unstable growth rate Ω and wavelength Λ:

$$D_{new} = 1.22 \cdot \Lambda \quad (6)$$

$$\tau_{BU} = 3.788 \cdot B_1 \cdot \frac{D_d}{2 \cdot \Lambda \cdot \Omega} \quad (7)$$

where B_1 is a tuning constant, which was set to 6 in this work. The reader is referred to [19, 20] for further details about the Kelvin-Helmoltz breakup model and the calculation of the wavelength and the growth rate.

As well known, high pressure GDI injectors are generally affected by cavitation. In a previous work, the authors studied the cavitation phenomena into a six-hole GDI injector very similar to that considered in the present analysis [21].

Collision model

To model collision in this work, the Nordin approach was adopted [8]. It states that collision between two parcels occurs only if, in the same integration step, their trajectories intersect and the intersection point is reached at the same time. This condition is fulfilled only when two parcels are travelling towards each other and their relative distance is greater than their size. The model accounts for both stretching separation and coalescence [22]. The Nordin model presents a reduced grid-dependency and this aspect is rather important when spray is simulated in unstructured and deforming meshes [8].

Wall-Impingement model

The interaction between the spray parcels and the liquid film is modeled with the approach proposed by Stanton et al. [23]. Generally, the collision between a drop and a wet surface may result in four different regimes: sticking, spreading, rebounding and splashing [24].

The impingement regimes are identified by the Weber number *We* defined as:

$$We = \frac{\rho \cdot V_p \cdot N_w \cdot d_0}{\sigma} \quad (16)$$

Where $\mathbf{V}_P$ is the relative velocity between the droplet and the wall, $\mathbf{n}_w$ is the face normal of the impinging wall, d_0 the droplet diameter and σ is the surface tension. The following transition criteria were used:

- $We < 5$: stick
- $5 < We < 10$: rebound
- $10 < We < We_S$: spread
- $We > We_S$: splash

W_{es} represents the splashing threshold and is given by [25, 26]:

$$We_S = 18^2 d_0 \left(\frac{\rho}{\sigma}\right)^{1/3} \left(\frac{\mu}{\rho}\right)^{1/4} f^{3/4} \quad (17)$$

where ρ, σ, μ, d_0, and f are the drop density, surface tension, dynamic viscosity, incident drop diameter, and frequency of drops impinging on the film.

The splashing process is modeled by introducing three new parcels in the mesh for each impinging droplet. A detailed description of the correlations used for momentum and mass exchange between the droplets and the liquid film in the rebound and splash regimes can be found in [25, 26].

Liquid-Film model

The formation of the liquid film is the result of the interaction between the injected fuel spray and the computational domain walls. For an engine simulation, a good prediction of the liquid film generation and evolution is mandatory because it has a strong influence on the fuel-air mixing process. In the paper, to simulate the wall film a shallow water formulation was adopted for the flow equations, solving for mean thickness, momentum and energy in a conservative manner. The liquid film equations were discretized on a curved 2-D surface in 3-D, accounting for its curvature and motion using the Finite Area Method. Faces of arbitrary shapes are supported, therefore it can be used with complex geometries like IC engines [13].

Adaptive local mesh refinement (ALMR)

ALMR enables a high mesh resolution where the fuel air mixing process takes place, while the overall grid size is weakly increased. The proposed approach works with hexahedral moving meshes. An initial computational mesh has to be provided by the user, whose size should be fine enough to correctly reproduce the geometrical domain to be simulated and the main details of the initial flow-field. Following previous approaches [27, 28], a geometric field is chosen as an error estimator and when its values lie in a user-specified interval the parent cell is split into eight child cells by introducing new nodes at the cell centroid and at the mesh face centers [29]. An arbitrary level of refinements can be chosen by the user as well as a maximum number of cells to control the mesh size. Grid un-refinement is also possible when the values of the error estimator are outside the specified interval. The geometric field used as a refinement criterion is represented by the total fuel mass fraction (liquid and gas) in each cell:

$$Y_{l+g} = \frac{m_{f,l} + \rho \cdot Y_f \cdot V_{cell}}{\rho \cdot V_{cell}} \quad (21)$$

where m_{fl} is liquid mass of all the parcels belonging to the cell, Y_f is the fuel mass fraction in the gas phase, ρ is the gas phase density, and V_{cell} is the cell volume. The consistency of the ALMR approach was verified in previous works for both evaporating and non-evaporating spray [12, 30]. It was shown that, depending on the chosen level of refinements, ALMR provides the same results of a uniform fixed mesh with the same minimum size. The comparison was performed in terms of spray penetrations and equivalence ratio distribution at different distances from the injector.

RESULTS AND DISCUSSION

Experimentally, different injection strategies were tested changing the injection duration, the injection pressure and the total injected mass. All the investigated configurations are collected in Table 1. At constant injection pressure, the injected fuel mass was increased by operating on the electric pulse duration. For each configuration, the injected fuel mass measured by the AVL Meter was compared with the weighted ones obtained by using a precision balance. The discrepancies were always lower than 2%. For each configuration reported in Table 1, the fuel injection rate was extracted from the experiments as the average of one hundred of shots. For example, Figure 1 shows the injection profiles obtained for mass fuel injected equal to 20 and 50 mg/stroke. It is interesting to note as all the profiles were quite similar in the overlapping parts.

Table 1: Time durations of the pulses for the desired fuel amounts at the indicated injection pressures.

t_{inj} [ms]		Total Injected Fuel Mass [mg/stroke]			
		10	20	50	100
P_{inj} [MPa]	3	1,3			
	6	0,9			
	10		1,45	3,6	
	15			2,9	5,8
	20			2,6	5,1

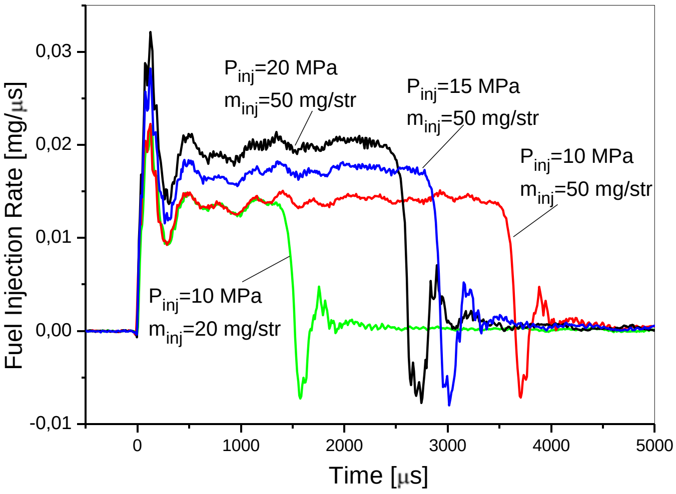

Figure 1: Profiles of the fuel injection rate for different injection conditions.

The evolution of the spray inside the vessel was monitored by the CCD camera synchronized with a flash light. A suitable spatial injector orientation enabled a full view of one of the six injector sprays. The CCD shutter, synchronized with the spray command at different instant from the start of the injection, limited image blurring and time indetermination to 0.5 µs.

Observing the spray from the lateral view, it was possible to evaluate the spray structure evolution and, in particular, the evolution of the interaction between the different jets. For example, Figure 2 shows the spray evolution recorded for the case: P_{inj}=20 MPa and m_{inj}=50 mg/stroke. As showed, during the first injection part the interaction between the jets was almost negligible. At later time (injection time higher than 400 µs) the jet swellings became evident and fuel pockets were generated by the coalescence phenomena. They were clearly visible by the experimental pictures because highlighted by the highest intensity in the scattered light. This was an unambiguous sign of a non-homogeneous fuel distribution inside the spray cloud.

Figure 2: Experimental detection of the GDI spray evolution. P_{inj}=20 MPa and m_{inj}=50 mg/stroke.

Post-processing the spray pictures, for each considered test configuration the time-evolutions of the spray penetration and cone angle were measured. In particular, both these parameters were measured for the jet disposed orthogonally with the CCD camera axis. Figures 3 and 4 show the influence on penetration and cone angle of the injection pressure for a total injected fuel mass equal to 50 mg/stroke. About the penetration evolution (Figure 3), during the first injection part (time lower than 500 µs) all the profiles show a typical linear trend versus time. Only after 500 µs from the hydraulic SOI, the different droplet momentum (linked to the different injection pressure) started to play a role against the gas resistance effect on the droplets. About the single spray cone angle, Figure 4 shows how this parameter was only slightly influenced by the injection pressure. In particular, fixing the total mass injected at 50 mg/stroke, for all the three considered injection pressures the single spray cone angle converged asymptotically to a value near 12°.

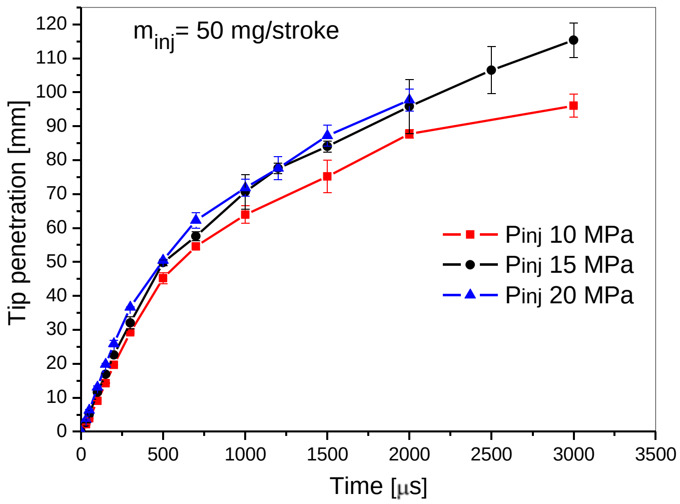

Figure 3: Spray tip penetration at 10, 15 and 20 MPa of injection pressure. Fuel mass injected: 50 mg/stroke.

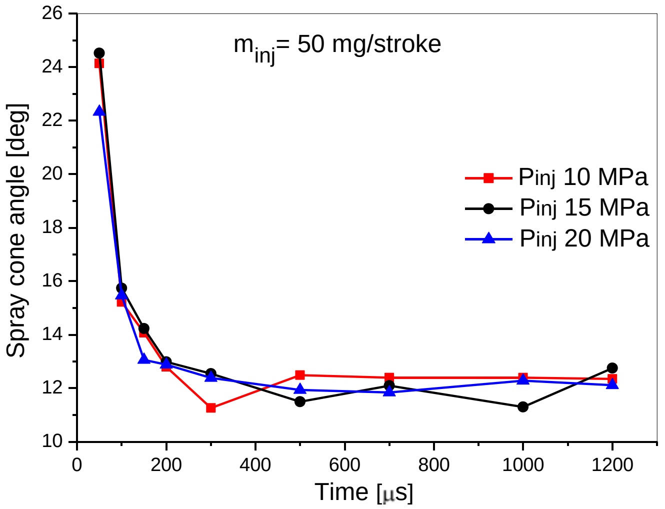

Figure 4: Cone angle at 10, 15 and 20 MPa of injection pressure. Fuel mass injected: 50 mg/stroke.

Image sequences of the spray evolution, taken simultaneously by two synchronized cameras orthogonally disposed, are reported in Figure 5 for the condition 20 MPa of injection pressure, 50 mg/stroke of delivered fuel and at atmospheric backpressure of the gas in the vessel. The frontal view of the sprays (top of the strips) highlights the evolution of the jet plumes coming out of the paper (the axis of the nozzle is parallel to the optical axis of the CCD lens). It shows an independent growth of the sprays up to about 200 µs from the SOI. The propagation of the jets are well defined indicating the fuel distribution inside the vessel. This regularity appears destroyed for the images at 500 and 700 µs where the interference between the single jets appears evident and the single jet evolution cannot be longer followed. Here the fuel figure has to be considered as a single, large and composite spray.

The lateral spray evolution view allows to distinguish the origin of the single jets close to the nozzle exit. Four single, well confined sprays appear in the foreground of the CCD view plane while two sprays are in the background and hidden from view.

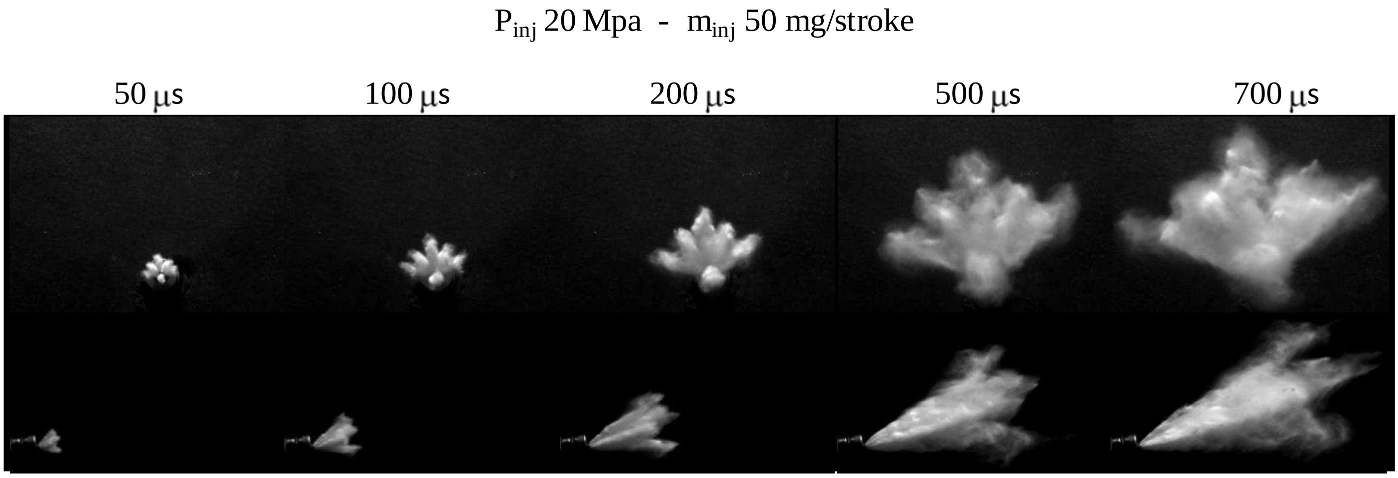

Figure 5: Spray evolution sequences at the indicated conditions taken frontally (top) and laterally (bottom)

As previously introduced, also the wall film generation and evolution was experimentally produced. To this end, the impact between the jets from the GDI injector and a flat plate was carried out. It was made for the working condition characterized by a P_{inj} of 20 MPa and m_{inj} of 50 mg/stroke. Figure 6 presents the picture sequence captured during the experimental test. As showed, the spray advanced freely into the vessel until 400 µs from the hydraulic SOI instant. Obviously, with respect to the same injection configuration previously tested without the plate, no changes were detected about the overall spray behavior until this instant. After 400 µs from hydraulic SOI, the first jet reached the plate surface starting to spread on it. At later time (800 µs) all the jets reached the plate and a uniform layer of fuel compensated the interspaces between the jets. At longest time (1400 µs), the different spray directions, therefore the different rebounding angles, produced a lateral evolution of the film. In particular, a compact fuel film having a uniform height was generated on the right side on the plate while on the left side of the plate the wall film was more curled and higher than on the right side (Figure 6). At the end of the injection process all the fuel was distributed laterally on the flat plate.

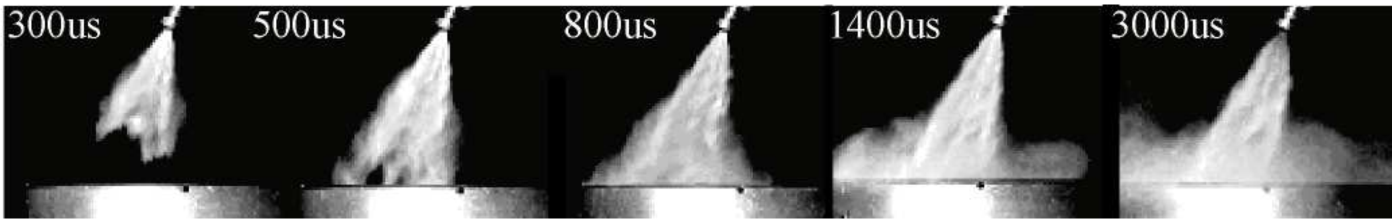

Figure 6: Evolution of the spray impact on the flat plane. P_{inj}=20 MPa and m_{inj}=50 mg/stroke.

CFD Simulations

Table 2 summarizes the injection operating conditions chosen to validate the CFD methodology previously presented. These cases were chosen because both the injection pressure range and the amount of injected fuel mass were typical of multi-hole atomizers usually adopted for GDI engines. Spray computations were subdivided into three steps. To test the proposed atomization model, the spray emerging from a single injector hole was firstly simulated. Then, the complete injector configuration, including all the six sprays, was taken into account to evaluate the effects of the collision model when interactions between multiple jets were present. Finally, experiments of impinging spray on a flat plate were used to validate the liquid film and droplet-wall interaction models. For all the simulations, the gasoline fuel was modeled using the iso-octane liquid properties and droplets were injected according to the experimental mass flow rate profiles. The standard k-ε model was used for turbulence.

Table 2: Simulated operating conditions.

	Injection pressure [MPa]	Injected fuel mass [mg/str]	Injection duration [μs]
1	10	20	1450
2	15	50	2900
3	20	50	2600

The single spray simulations were performed considering the same jet chosen as reference during the experimental campaign. As computational domain, a box with 20 x 20 x 120 mm size was used and it was filled with air at atmospheric pressure and ambient temperature (300 K, 1 bar). The injector tip was placed on the top of the test rig. The computational volume was discretized by a spray-oriented grid having an initial size of 4 mm. During the simulation, the Adaptive Local Mesh Refinement technique was adopted to guarantee a good level of convergence to the simulation. In particular, two refinement levels were used, corresponding to a minimum mesh size of 1 mm. The chosen minimum size represents a good compromise between the CPU time required and the results accuracy. It is important to point out that, when the ALMR method is used in spray simulation, the grid is refined only where the spray evolves. As a consequence, also the computed velocity field in that region is better predicted.

To evaluate the performance of the simulation methodology, the first parameter which was compared to experimental data was the spray penetration. The Figure 7 illustrates that the proposed model is able to reproduce the spray penetration dependency on the injection pressure even if a slight overestimation exists until 500 μs after the hydraulic start of injection. However, the overall behavior of the proposed approach could be considered rather satisfactory and for this reason it was employed in the remainder of the simulations where all the six sprays were taken into account.

The computational domain used to simulate the complete injector configuration consisted in a cubic box of 120 mm size and the collision model was activated. Adaptive Local Mesh Refinement was used also in this case, but it was not possible to keep the mesh spray-oriented because of the different spray patterns. This generally happens also in CFD simulations of GDI engines where unstructured meshes are generally adopted to accommodate complex geometry features like piston bowl, canted valves and cylinder head. Figure 8 shows the comparison between experimental and numerical evolution of the full spray for an injection pressure of 20 MPa (the Lagrangian particles were scaled according to their diameter values). Also in this case, in comparison to the experimental evidence, the spray shape, cone angle and penetration were rather well predicted. The effect of the collision model on the spray evolution was detected in terms of fuel cluster generation along the main spray axis. This aspect strongly influences the spray atomization process and probably the fuel-air mixing process as well. Hence, collision has to be taken into account when the evolution of multiple sprays have to be simulated in GDI engines.

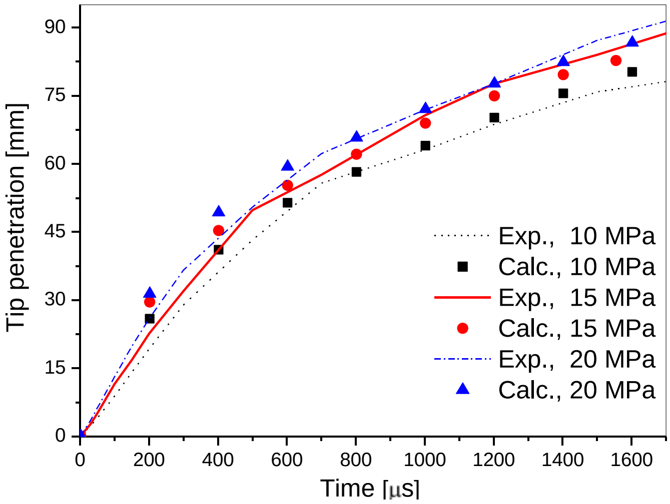

Figure 7: Comparison between computed and experimental spray penetrations as a function of the injection pressure.

(a): Experimental Evolution

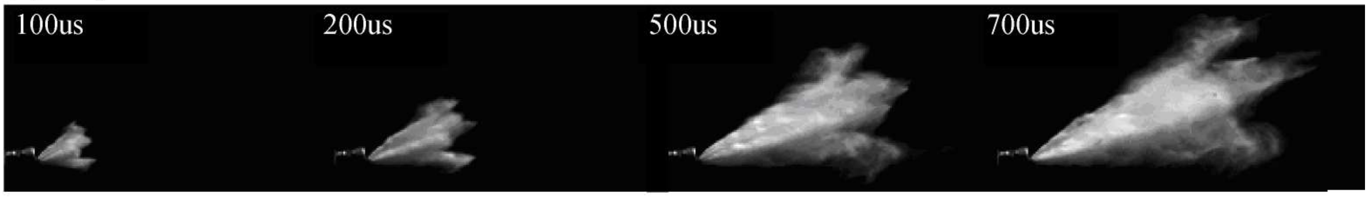

(b): Simulation - Collision Model Off

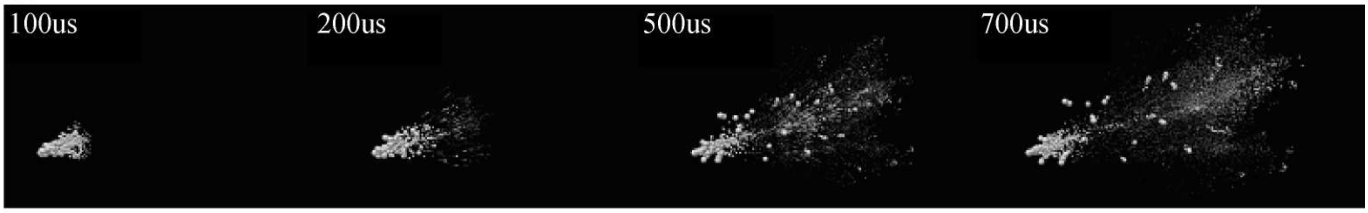

(c): Simulation - Collision Model On

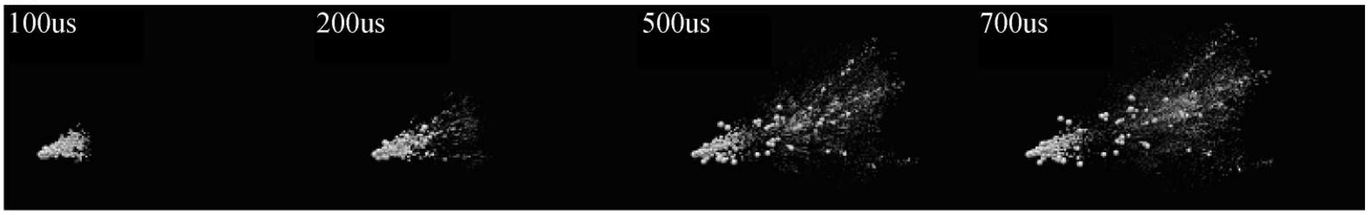

Figure 8: (a) Experimental data of spray evolution at injection pressure of 20 MPa (b) Computed spray evolution without the collision model; (c) Computed spray evolution including the effects of collision and coalescence.

Once a suitable set of spray sub-models was identified to describe fuel atomization and breakup in GDI engines, CFD calculations were performed to verify the droplet-wall interaction and liquid film models. As for experiments, a flat plate was introduced into the computational domain at a distance of 40 mm from the injector tip. The plate was disposed perpendicularly to the jet chosen as reference. For consistence to the experiments, an injection pressure of 20 MPa was chosen.

The computed spray distribution, in combination with the liquid film thickness and velocity field are shown in Figure 9 for different times after the start of injection. The liquid film expands in three different directions that are strictly related to the injector spray patterns. These kind of investigations can be very useful to improve both the injector and the piston bowl design.

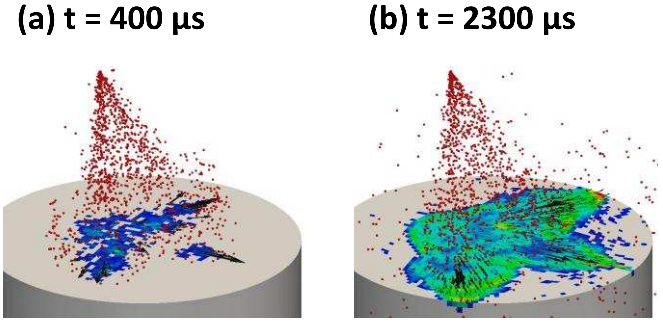

Figure 9: Computed evolution of liquid film thickness and velocity field at 400 and 2300 µs after the start of injection. Liquid film thickness range 0 (blue) to 0.1 mm (red).

In Figure 10, the computed spray evolution is compared to experimental data at impinging conditions. According to the proposed model, impingement starts 300 µs after SOI, which was 100 µs in advance with respect to the measurements. This discrepancy was due to the overestimation of spray penetration, as illustrated in Figure 7. Once impingement was established, the predicted shape of the spray cloud was in rather good agreement with experimental data: two curls were formed on the left and right sides and the first one propagates faster (see Figure 10). The model also seemed to reproduce correctly the maximum value of the wall spray height. For a further validation of the proposed wall-film model, more experiments are required to verify the validity of the droplet-wall interaction model and the influence of the Leidenfrost effects that has to be taken into account because of the high temperatures of the cylinder walls.

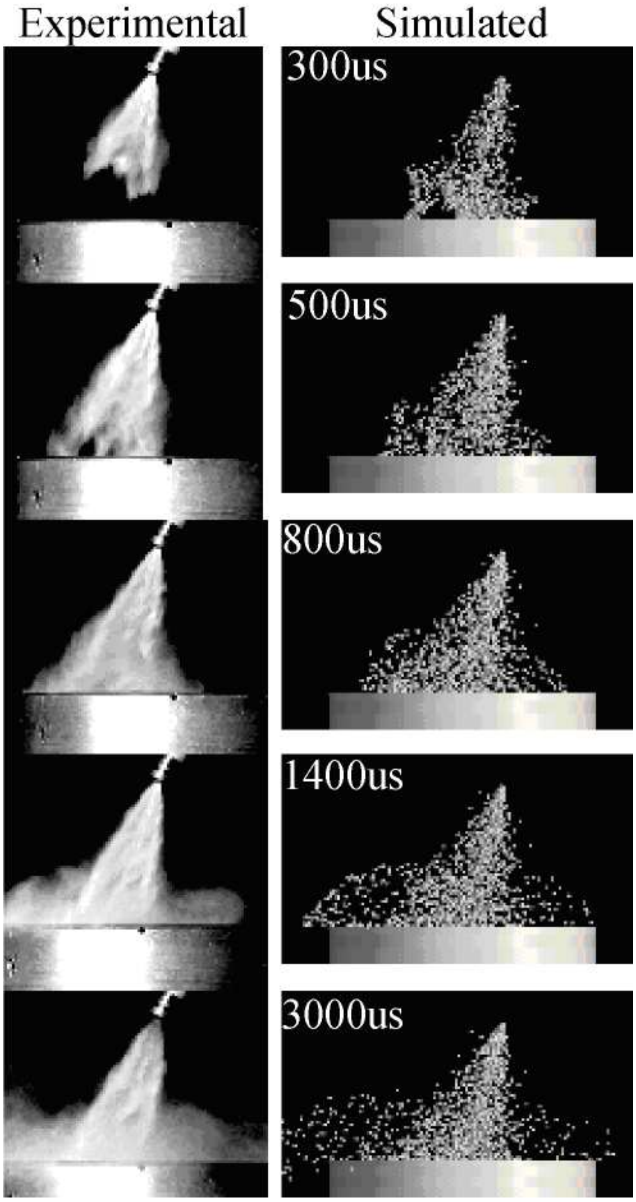

Figure 10: Comparison between computed and experimental spray evolution at impinging conditions.

CONCLUSIONS

Experiments and simulations were carried out to investigate the behavior of non-evaporating sprays emerging from a multi-hole injector designed for GDI applications. Purpose of this work was to define a suitable CFD methodology to model the fuel-air mixing process in GDI engines and, at the same time, to identify a set of experiments and operating conditions that can be helpful to improve the existing numerical models. The proposed CFD approach accounts for the main processes governing cavitation inside the nozzle, fuel atomization, droplet breakup, collision/coalescence and interaction with the walls. Experimental data of spray penetration, cone angle together with optical images were available for validation. The global evolution of the spray was investigated by the imaging technique applying the digital processing of images, acquired by a synchronized CCD camera. The main experimental results can be summarized as:

- The plumes of the single jets develop independent each other for different time from the SOI depending on the injection conditions. At 20 MPa the jets start to interfere at 500 μs,
- Fuel pockets appear in the jet images indicating a non-homogeneous distribution of the fuel inside the spray,
- The injection pressure strongly influences the penetration while total amount of delivered fuel produce negligible effects,
- About the spray cone angle, slight effects come from the injection pressure and no variations are due to the injected fuel amount.

Computed results correctly reproduce the experimental trends in terms of spray penetration dependency on the injection pressure and droplet distribution including also impinging conditions. Despite a rather satisfactory agreement was obtained, calculations revealed the need to perform further experiments in future work to better clarify how spray evolution is influenced by the following phenomena:

- Cavitation inside the nozzle,
- Influence of collision and coalescence on droplet diameter and evaporation rate,
- Effects of the different impinging regimes on the liquid film formation and evolution,
- Influence of the Leidenfrost effect on the liquid film evolution.

To this end, new experimental conditions are being investigated by the authors. In particular, a Phase Doppler Anemometry (PDA) system is now available to measure the droplet size and velocity at different distances from the injector.

NOMENCLATURE

D_d: droplet diameter.
d_0: droplet diameter before impingement.
L_{nozz}: injector nozzle length.
L_{t0}: liquid turbulent length scale at the nozzle exit.
V_{cell}: cell volume.
V_p: droplet velocity at impinging conditions.
We: droplet impact Weber number.
We_s: Weber number defining splashing conditions.
Y_{l+g}: total fuel mass fraction in each computational cell.
Y_f: fuel vapor mass fraction in a computational cell.
α: spray cone angle.
ε_{d0}: turbulent kinetic energy dissipation rate at the nozzle exit.
μ: liquid dynamic viscosity.
Ω: growth rate.
ρ: gas density.
σ: liquid surface tension.
τ_{t0}: liquid turbulent time-scale at the nozzle exit.
K_c,K_ε,B_1,C_1,C_3: model tuning constants.

REFERENCES

[1] Zhao, F. Q., and Lai M., “A Review of Mixture Preparation and Combustion Control for Spark-Ignited, Direct-Injection Gasoline Engines,” SAE Technical Paper 970627, 1997.

[2] Shahed, S. M., and Bauer K. H., “Parametric Studies of the Impact of Turbocharging on Gasoline Engine Downsizing,” SAE Int. J. Engines (2):1347-1358, 2009.

[3] Rivera, E. A., Mastro, N., Zizelman, J., Kirwan, J., Ooyama, R., “Development of Injector for the Direct Injection Homogeneous Market using Design for Six Sigma, “ SAE Technical Paper 2010-01-0594, 2010.

[4] Adomeit, P., Weinowski, R., Ewald, J., Brunn, A., Kleeberg, H., Tomazic, D., Pischinger, S., Jakob, M., “A New Approach for Optimization of Mixture Formation on Gasoline DI Engines,” SAE Technical Paper 2010-01-0591, 2010.

[5] Matsumoto, A., Moore, W, Lai, M., Zheng, Y., Foster, M., Xie, X., Yen, D., Confer, K., Hopkins, E., “Spray Characterization of Ethanol Gasoline Blends and Comparison to a CFD Model for a Gasoline Direct Injector,” SAE Technical Paper 2010-01-0601, 2010.

[6] Nauwerck, A., Pfeil, J., Velji, A., Spicher, U., Richter, B., “A Basic Experimental Study of Gasoline Direct Injection at Significantly High Injection Pressures”, SAE Technical Paper 2005-01-0098, 2005.

[7] Abart, M., Schmidt, S., Schoegl, O., Trattner, A., Kirchberger, R., Eichlseder, H., Jajcevic, D., “Basic Investigations on the Prediction of Spray-Wall and Spray-Fluid Interaction for a GDI Combustion Process”, SAE Technical Paper 2010-32-0030, 2010.

[8] Nordin N., “Complex Chemistry Modeling of Diesel Spray Combustion,” PhD thesis, Chalmers University of Technology, Department of Thermo Fluid Dynamics, Goteborg, 2001.

[9] Lucchini T, D'Errico G., Brusiani F., Bianchi G. M., "A Finite-Element Based Mesh Motion Technique for Internal Combustion Engine Simulations," presented at COMODIA 2008, Sapporo, Japan, July 27-31, 2008.

[10] Montenegro G., Onorati A., Piscaglia F., D'Errico G., " Integrated 1D-MultiD Fluid Dynamic Models for the Simulation of I.C.E. Intake and Exhaust Systems," SAE Technical Paper 2007-01-0495, 2007.

[11] OpenFOAM, “The Open-source CFD toolbox,” http://www.openfoam.org/, September 2010.

[12] Lucchini, T., Ettorre, D., D’Errico, G., Brusiani, F., Bianchi, G., Montanaro, A., Allocca, L., “Experimental and Numerical Investigation of High-Pressure Diesel Sprays with Multiple Injections at Engine Conditions”, SAE Technical Paper 2010-01-0179, 2010.

[13] Lucchini, T., D'Errico, G., Brusiani, F., Bianchi G. M., Tukovic Z.,Jasak, H. “Multi-dimensional modeling of the air/fuel mixture formation process in a PFI engine for motorcycle applications,” SAE Technical Paper 2009-24-0015, 2009.

[14] Bosch, W. "The Fuel Rate Indicator: a New Measuring Instrument for Display of the Characteristics of Individual Injection", SAE Paper 6607496, 1966

[15] Wallace: I. “ Injection Rate Gauge: Pass Off Information and User Instructions” - Fuel & Engine Management Systems, Graz - December 2002

[16] Alfuso, S., Allocca, L., Caputo, G., Corcione, F.E., Montanaro, A., Valentino G.,: “Experimental Investigation of a Spray from a Multi-jet Common Rail Injection System for Small Engines” SAE_NA 2005-24-9

[17] Huh, K. Y., Gosman, A. D., “A Phenomenological Model of Diesel Spray Atomization,” Proceedings of the International Conference on Multiphase Flows, September 24-27, Tsukuba, Japan, 1991.

[18] Bianchi, G. M., Pelloni, P., “Modeling the Diesel Fuel Spray Breakup by Using a Hybrid Model,” SAE Technical Paper 1999-01-0226, 1999.

[19] Reitz, R. D. “Modeling Atomization Processes in High-Pressure Vaporizing Sprays,” Atomization and Spray Technology (3): 309–33, 1987.

[20] Reitz, R.D., Bracco, F. V., “Mechanisms of Breakup of Round Liquid Jets,” In Encyclopedia of Fluid Mechanics, Gulf Pub, (3):233–249, 1986.

[21] Brusiani, F., Falfari, S., Forte, C., “The Role of Cavitation inside High Pressure GDI”, ATI Technical Paper ATI09-11-009, 2009.

[22] Qian J., Law K., “Regimes of Coalescence and Separation in Droplet Collision,” J. Fluid Mech (331):59–80, 1997.

[23] Stanton, D., Lippert, A., Reitz, R. D., Rutland, C.J., “Influence of Spray-Wall Interaction and Fuel Films on Cold Starting in Direct Injection Diesel Engines,” SAE Technical Paper 982584, 1998.

[24] Kolpakov, A. V. et al., ”Calculation of the Rebound Condition for Colliding Drops of Sharply Different Sizes,” Kollodn. Zh. (47), 1985.

[25] Stanton D., and Rutland, C.J., “Modeling fuel film formation and wall interaction in diesel engines,” SAE Technical Paper 960628, 1996.

[26] Yarin, A. L., and Weiss, D. A., ”Impact of Drops on Solid Surfaces: Self-Similar Capillary Waves, and Splashing as a new Type of Kinematic Discontinuity,”. Journal of Fluid Mechanics (283), 1995.

[27] Senecal, P. K., Richards, K. J., Pomraning, E., Yang, T., Dai, M. Z., McDavid, R. M., Patterson, M. A., Hou, S., Shethaji, T., “A New Parallel Cut-Cell Cartesian CFD Code for Rapid Grid Generation Applied to In-Cylinder Diesel Engine Simulations,” SAE Technical Paper 2007-01-0159, 2007.

[28] Lippert A. M., Chang S., Are S., Schmidt D.P, “Mesh Indipendence and Adaptive Mesh Refinement For Advanced Engine Spray Simulations,” SAE Technical Paper 2005-01-0207, 2005.

[29] Jasak H., “Error Analysis and estimation for the finite volume method with applications to fluid flows,” Ph.D. thesis, Imperial College of Science, Technology and Medicine, London, 1996.

[30] Lucchini, T., Ettorre, D., D’Errico, G., Ferrari, G.,” Numerical Investigation of Non-Reacting and Reacting Diesel Sprays in Constant-Volume Vessels,” SAE Int. J. Fuel and Lubr. (2):966-975, 2009.

DIPSI Workshop 2011 on Droplet Impact Phenomena & Spray Investigation
May 27, 2011, Bergamo, Italy

EXPERIMENTAL ANALYSIS OF THE DISTRIBUTION OF DROPS IN THE LOW PRESSURE AREA GENERATED BY TWO SPRAY

A.Amoresano*, F. Langella*, F. De Domenico°,

*Mechanical and Energetic Engineering Department, Via Claudio 21 80125 Naples
°Spatial and Aeronautic Engineering Department, Piazzale Tecchio 80 80125 Naples

ABSTRACT
In order to obtain an appreciable effect of extinction of the heat from a heat source (eg a fire) it is necessary that the water flows are high (20- 30 liters per minute) and the droplet diameters are between 20 and 100 microns. To achieve both of these two features are the nozzles of the type used multi hole and supply pressures exceed 80 bar. In these conditions there are strong interactions between the individual holes that generate particular phenomena such as entrainment' s air and the generation of areas where the drops tend to stagnate. To understand the physics of this second phenomenon, in this paper the interaction of two spray is studied . It defines the regions of interaction between the two sprays and then these are characterized using a PDA system.

INTRODUCTION

A spray is generally considered as a system of drops immersed in a gas continuous phase. Most practical atomizers generate drops in the size range from a few micrometers up to around 500 μm. Owing to the heterogeneous nature of the atomization process, the threads and the ligaments formed by the various mechanisms of jet and sheet disintegration vary widely in diameter, and the resulting main drops and satellite drops vary in size correspondingly. Practical atomizers do not produce sprays of uniform drop size at any given operating condition; instead, the spray can be regarded as a spectrum of drop sizes distributed about some arbitrarily defined mean value. In addition to mean drop size, another important parameter of importance in the definition of a spray is the distribution of drop sizes it contains.

A simple method of illustrating the distribution of drop sizes in a spray is to plot a histogram where each ordinate represents the number of droplets whose dimensions fall between the limits D-ΔD/2 and D+ΔD/2.As ΔD is made smaller, the histogram assumes the form of a frequency distribution curve. Because the graphical representation of droplet size distribution is laborious and not easily related to experimental results, many workers have used to replace it with mathematical expressions and their parameters can be obtained from a limited number of drop size measurements. The most widely used expression for drop size distribution is Rosin –Rammler, it may be expressed in the form

$$1\text{-}Q = \exp[-(D/X)^q]$$

Where Q is the fraction of the total volume contained in drops of diameter less than D, and X and q are constants that are determined experimentally; the exponent q provides a measure of the spread of drop size. The higher the value of q, the more uniform the spray. If q is infinite, the drops in the spray are all the same size. For most practical sprays the value of q is between 1.8 and 3.0.From analysis of a considerable drop size data obtained with pressure-swirl nozzles, Risk and Lefebvre rewritten the Rosin-Rammler equation in the form

$$1\text{-}Q = \exp[-(\ln D/\ln X)^q]$$

Mean Diameters

In many calculations of mass transfer and spray evaporation it is convenient to work only with mean or average diameters instead of the complete drop size distribution. One of the most common mean diameters is D10 [1].

$$D_{10} = \frac{\sum_{i=1}^{N} D_i}{N}$$

The most important mean diameter for combustion applications is the Sauter mean diameter, which is usually abbreviated to SMD or D32. This diameter is a number used to express the average droplet size in terms of the average ratio of volume to surface area of the droplets:

$$D_{32} = \frac{\sum_{i=1}^{N} N_i D_i^3}{\sum_{i=1}^{N} N_i D_i^2}$$

So:

$$D_{ab} = \left[\frac{\sum_{i=1}^{N} N_i D_i^a}{\sum_{i=1}^{N} N_i D_i^b} \right]^{1/(a-b)}$$

where *i* denotes the size range considered, Ni is the number of drops in size range *i*, and Di is the middle diameter of size range *i*. For example, D30 is the diameter of a drop whose volume, if multiplied by the number of drops, equals the total volume of the sample.

Characterization Pressure Swirl Atomizers

Pressure swirl atomizers [2] rely on the conversion of pressure into kinetic energy to achieve a high relative velocity of the liquid and the surrounding gas. In pressure swirl atomizer, a swirling motion is also imparted to the liquid so that, under the action of centrifugal force, it spread as a conical sheet as soon as it leaves the orifice. There are two basic types of pressure nozzles. In the first one, the *solid-cone pressure atomizer,* the spray is consists of drops that are distributed fairly uniformly throughout its volume (Figure 1) the second one, the *hollow-cone pressure atomizer,* produces a hollow-cone spray, in which most of droplets are concentrated at the outer edge of a conical spray pattern. The main drawback of solid-cone nozzle is a coarse atomization, the drops at the center of the spray being larger than those near the periphery. Hollow-cone nozzles provide better atomization and their radial liquid distribution is also preferred for many industrial processes, especially for combustion applications. The simplest design of the hollow-cone nozzle is the simplex atomizer Liquid is fed into a swirl chamber through tangential ports that give it a high angular velocity, thereby creating an air-cored vortex. The outlet from the swirl chamber is the final orifice, and the rotating liquid flows through this orifice under both axial and radial forces to emerge from the atomizer with the shape of a hollow conical sheet, the actual cone angle being determined by the relative magnitude of the tangential and axial components of exit velocity.

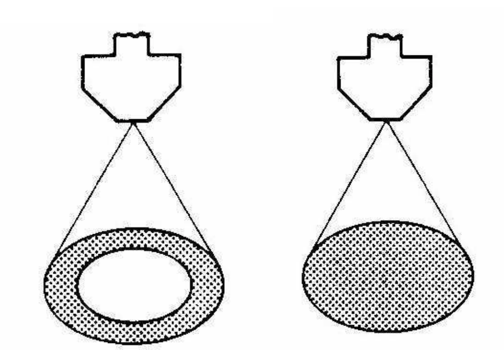

Figure 1- Spray produced by pressure-swirl atomizer: a) hollow cone, b) solid cone

The main drawback of solid-cone nozzle is a coarse atomization, the drops at the center of the spray being larger than those near the periphery. Hollow-cone nozzles provide better atomization and their radial liquid distribution is also preferred for many industrial processes, especially for combustion applications. The simplest design of the hollow-cone nozzle is the simplex atomizer.

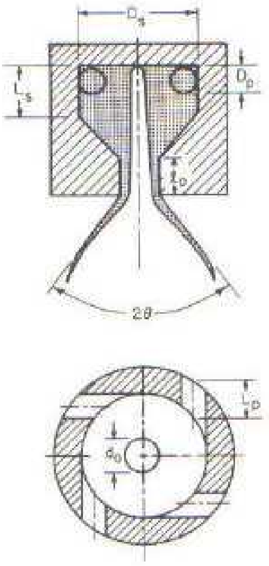

Figure 2 - Schematic view of a simplex swirl nozzle

Since Sauter mean diameter deals with surface area, it is a good way to describe a spray that is to be used for processes involving evaporation. Because of the complexity of the physical phenomena involved in atomization by pressure swirl nozzles, the study of atomization has been performed principally by empirical methods, resulting in correlations for SMD of the following general form:

$$SMD = 2.25\sigma^{0.25}\mu_L^{0.25}\dot{m}_L^{0.25}\rho_A^{-0.25}\Delta P_L^{-0.5}$$

where:
σ is the surface tension.
ν is the kinematics viscosity.
m L is the mass flow rate.
ΔPL is the injection pressure differential across nozzle.

This formula takes no account of spray angle, which is known to affect mean drop size. To overcome some of the deficiencies of this relation, and to explain some of the apparent anomalies that careful measurements often reveal, Lefebvre has proposed an alternative form equation for the mean drop sizes produced by pressure-swirl atomizers. This equation is not the result of a mathematical treatment of the subject, but is based on considerations of the physical process involved in pressure swirl atomization. Several different mechanisms have been proposed to describe the atomization process, it is generally agreed that the disintegration of a liquid jet or sheet issuing from a nozzle is not caused solely by aerodynamics forces, but must be result of turbulence or other disruptive forces within the liquid itself. These disturbances are very important for the sheet disintegration, especially in the first stage of atomization. Subsequently, the relative velocity between the liquid and the surrounding air has a profound effect on atomization through its influence on the development of waves on the initially smooth surface. Any increase in this velocity causes a reduction in the size of the ligaments that disintegrate and become smaller drops. The process of atomization in pressure swirl atomizer is complex so it is useful to divide it into two main stages. The first represents the generation of surface instabilities due to the combined effects of hydrodynamic and aerodynamic forces. The second stage is the conversion of surface protuberances into ligaments and then drops.

INTERACTION BETWEEN TWO SINGLE HOLE SPRAY

When droplets are expelled at a high velocity by a spray, a strong vertical air jet is induced throughout which the smallest droplets are dispersed (their Reynolds numbers associated with their relative motion being small). In our analysis we focus on the interaction between quiescent air and this spray jet. The impulsive ejection of the liquid phase is due to the conversion of the pressure energy in kinetic energy causes the pressure reduction close to the boundary layer in the region far from the tip of the spray. The atomizing characteristics investigated in this research include the spray droplet size distribution and behavior out the boundary layer between liquid phase and quiescent air.

The atomizer are used in a lot of industrial field [5] like gas turbine, internal combustion engine, agricultural. In several of these fields the atomizer used are multi hole atomizer. In the fight fighter field a typical multi hole atomizer is shown in the fig 3.

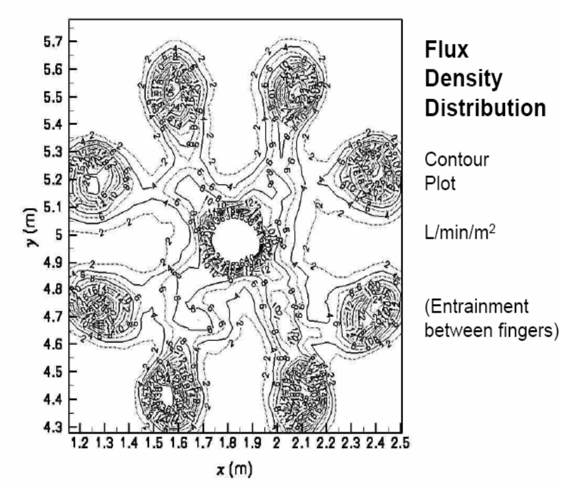

Fig.3 Flux density distribution in a multihole watermist pressure swirl atomizer

The picture represents the flux density distribution and the lines between the central hole and each periferical hole show the presence of regions where the dristibution of the droplets depends on the fluidodynamics field created by their intereaction.

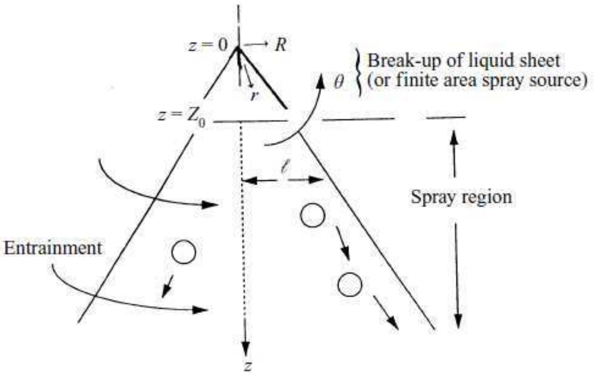

Fig. 4 Gas liquid interaction in the liquid break-up region of Twin-fluid atomization [3]

The figure 3 and 4 shows the dynamic mechsanisms repectively theoretical and experimental that arise when a single hole pressure swirl nozzle is used . The liquid film generates a drop of static pressure close to the boundary layer of a liquid phase. In this region it is possible that some droplets detach from the liquid boundary layer and are call back from the exteral region. If a secondary singlehole exists will arise an interaction between the two sprays. This interaction depends on the the supply pressure of the atomizers and on the distance of the holes.

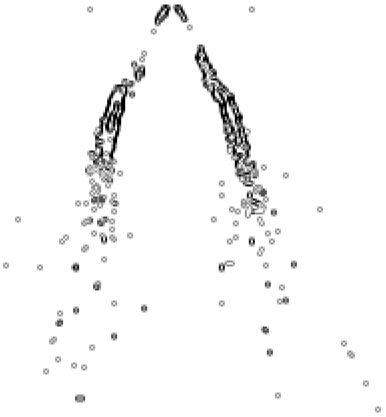

Fig 4. Experimental image of gas liquid interaction in the liquid break-up region of a single hollow cone nozzle

In this paper will be studied and characterized the behavior of the droplets along the regions generated by the fluid dynamics of the interaction of two sprays

EXPERIMENTAL APPARATUS

Two Danfoss pressure swirl atomizer 7 l/min 60° HC 7 bar supply pressure are been used to create the interaction between two sprays like shown in fig.5

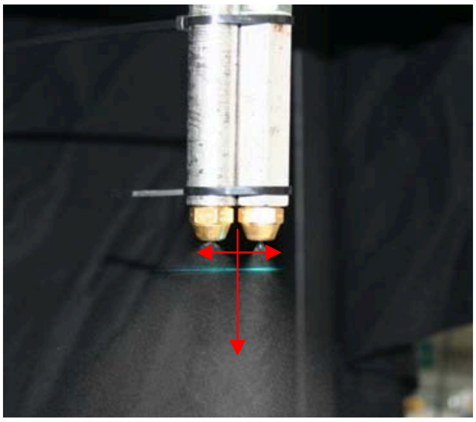

Fig.5 Nozzles interacting

The configuration of the two sprays gives the following schematic distribution of the interaction of the two sprays Fig 6.

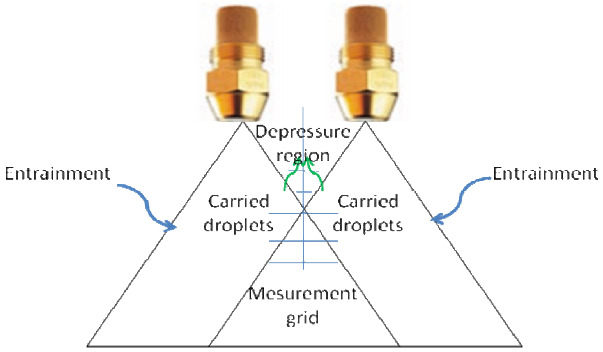

Fig 6. Schematic flow field generated by the interaction of two nozzle

The figure shows that the interaction of two sprays, or two holes of a spray head, creates three region. The first is situated between the two tips of the nozzles and it's called depressure region or empty region. The second region is also called "free zone". In these part of space the nozzle can be analyzed like a single nozzle because the fluxes don't between them . The third region is called "intersection zone" because the overlapping of the two spray. The figure 6 shows also that the grid of the measurements crosses through the all three regions.

Depressure or empty zone.

The depressure zone is far from the tip of the nozzle about 12 mm. This region develops itself along the break-up of liquid sheet length like shown in fig. In this space two phenomena arise. The first phenomenon is due to the interaction of the two phases liquid and gaseous. Close to the tip of the nozzles the energy of pressure is quickly converted in kinetic energy so the liquid injected interacts with the surrounding quiescent gas (air) and the breakup of the ligaments begins. The interaction of the two phases creates, on the their boundary layers, e shear stress and some droplets leave the liquid phase and are callback by the depressure generated between the two nozzles.

Intersection zone

In the intersection zone the droplets generated by the two nozzles interacts among them and can coalesce. In this region we will expect droplets with large diameter due to the interaction o droplets in a low velocity flow field.

Free zone

It is the region where the n behavior of the spray is the same of the single spray.

Devices and Controls

The tests to characterize the droplet distribution are carried out using the apparatus shown in the following figures:

The volumetric Haskel pump has been used to have a constant supply pressure. The volumetric pump is supplied by compressed air in a range of 1-10 bar corresponding to a pressure of the liquid phase of 10-350 bar. In the fig. 7 the air line (supply circuit of the pump) and spray line (supply circuit of the atomizer) are shown.

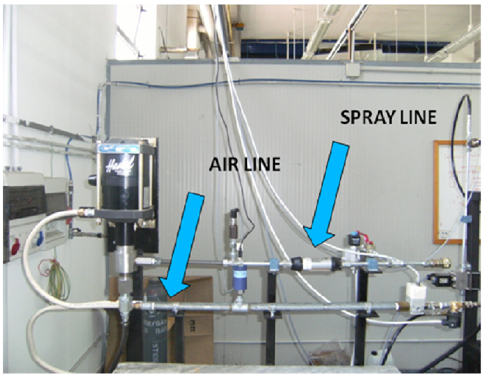

Fig.7 Volumetric pump, air and spray line

The test bench and it's sensors are controlled by a data acquisition system. The fig. 8 shows the control panel designed in Labview language

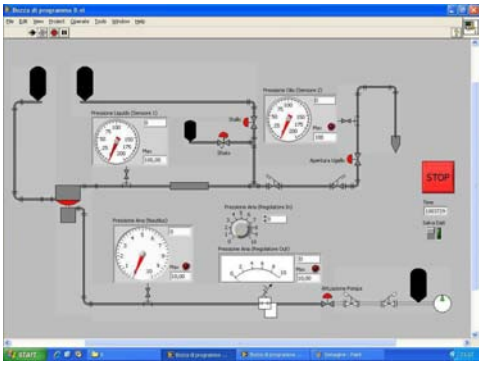

Fig. 9 Remote control panel and data acquisition system

The atomizer is set up on a vertical test stand which allows the atomizer itself to translate both in vertical and horizontal directions relative to a fixed. control volume to within 0.1 mm, in order to make the measurement possible in several points in the vertical plane. Liquid, coming from a storage tank, and it is vertically injected into the environment.

Droplet sizes and velocities as well as drop concentration have been measured by two component phase Doppler anemometer [7] [8] [9][10] [11][12][14] The latter is composed of a Ar- ion laser, as a light source, and a PDA system (Dantec) which includes a Bragg cell, transmitter and receiver probes, and BSA flow to analyze the signals and to acquire the interested output quantities. As said previously, the Bragg cell is used to shift the Doppler frequency, in particular the frequency imposed is 40 kH. The focal length is 310 mm. The laser power was typically 25 mW per beam. The laser beams wavelength is 514.5 nm and 488 nm, for the vertical and horizontal component of the velocity measurement, respectively. Drop sizes assuming spherical particles have been measured in first order refraction.

RESULTS AND CONCLUSIONS

The measurements start from the centre of the two nozzle and move in horizontal and vertical direction. The first valid line of the measurement is the one where the geometrical and spherical validation [14] of the PDA was realized . The validation limit has been chosen when the droplets processed by the PDA were about 30.000. In fig. 9 is represented the D10 [4] [15][16] diameter along the entire field of measurements. On the x axis the zero point represents the origin of the coordinates like shown in fig.5. The colored lines represent the distance from the tip of the nozzles. The fig. 10 represents instead the SMD. It is possible to divide the diagram in three diagrams representing the three regions, empty, intersection and free zone

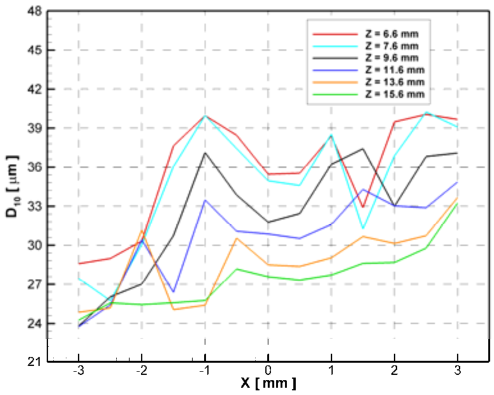

Fig. 9 Representation of the mean diameter to several radial and axial coordinates

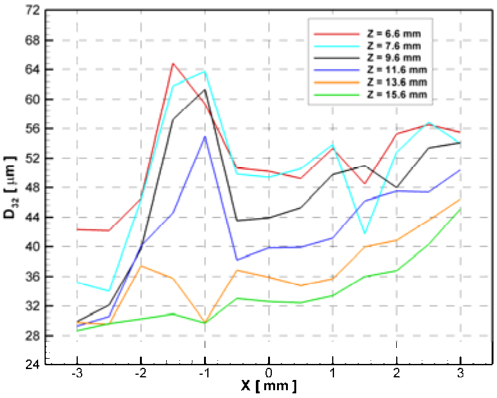

Fig. 10 Representation of the SMD to several radial and axial coordinates

The figure11 represents the characterization of the empty zone only. It shows that in the empty zone are present some droplets coming from the boundary layer of the two atomizers. In particular the diagram shoe the trend represented by the dashed line. The dashed line represents the D_{10} of a perfect symmetrical position of the two sprays.

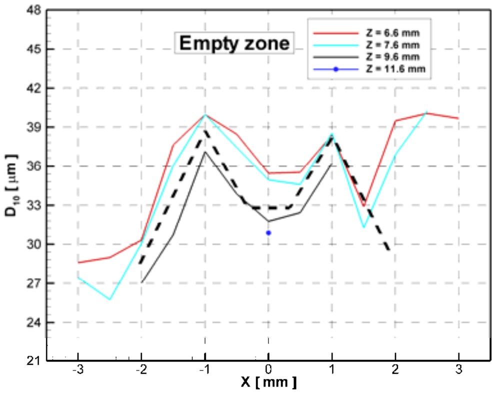

Fig. 11 Representation of the mean diameter to several radial and axial coordinates in the empty region

The value of the common mean diameter is low close to the boundary layer and it increase along the horizontal direction and achieves a minimum on the 0 point of the x axis. This trend is the same for each distance from the y axis.

In fig the trend of the D_{32} is represented. Also in this diagram the SMD diameters increase coming from the gas liquid interface and achieves a maximum before of the x=0. In this point all the D_{32} distributions achieve a minimum and then have another maximum going to the other gas liquid interface.

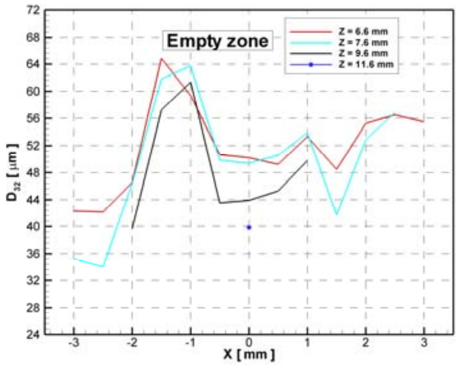

Fig. 12 Representation of the SMD to several radial and axial coordinates in the empty region

The measurements done and the related diagrams have put in evidence that the empty zone interacts with the two spray and in the region between the two spray arises a “fog” due to the callback of the droplets from the gas liquid interface that has kept suspended by the depressure inside the empty zone.

These statements are supported by the following diagrams where the volume fraction distribution is represented.

The fig 13 shows the volume fraction distribution of the droplets in the empty region measured in the three points, x = -1,5 mm, x=0mm, x=1.5mm and far from the tip of the nozzles 7,6 mm. This distribution show that most of the droplets have a diameter between 55 and 100 µm and only few small droplets (10-15 µm).

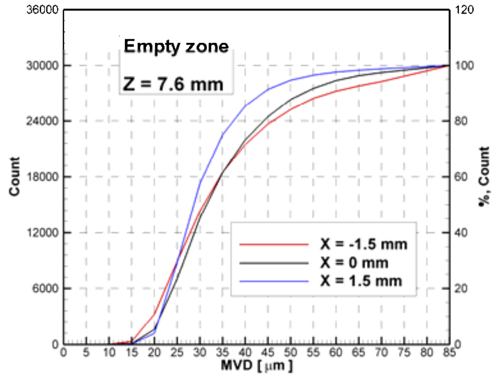

Fig. 13 Volume fraction distribution in the empty region

It is interesting to compare the distribution of drops of the empty region with that of the other two regions defined in the publication. The fig.14 shows the MVD inside the free region that is the same distribution of a single spray.

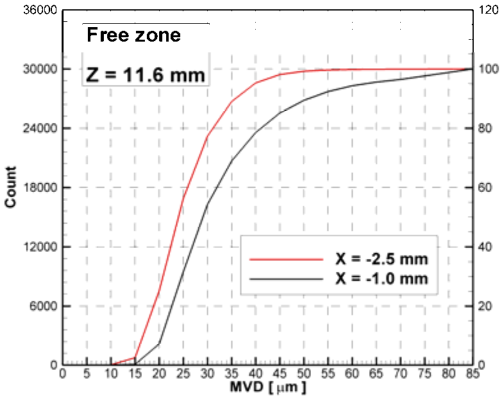

Fig. 14 Volume fraction distribution in the free region

The diagram shows that at x=2,5mm the most of the droplets has a diameter between 50 and 80 µm. The following picture represent the volume fraction inside the intersection zone.

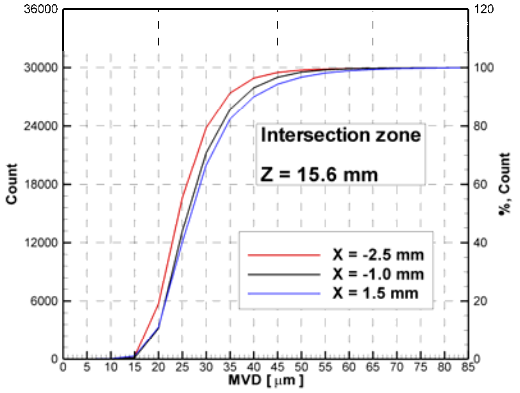

Fig. 15 Volume fraction distribution in the intersection region

It is interesting to note that the, in this case, volume fraction distribution is quite independent of the radial coordinate. The most of the droplets has a diameter between 50 and 85 µm. This is due mainly to the exchange of momentum and to the phenomenon of coalescence among the droplets.

REFERENCES

[1] Nasr, G. G., Yule, A. J., Bendig, L., *Industrial Sprays and Atomization*, Springer,2002

[2] Lefebvre, A. H., *Atomization and Sprays*,

[3] U. Shavit, *Gas liquid interaction in the liquid break-up region of Twin-fluid atomization*, “Experiment in fluids 31 (2001), 550-570

[4] Wang, X., Lefebvre, A. H., Mean Drop Sizes from Pressure-Swirl Nozzles, Journal *R.Clift, J.R.Grace, M.E. Weber.* - Bubbles, Drops and Particles

[5] *G.G. Nasr , A.J. Yule, L. Bending.* - Industrial Sprays and Atomization Design, analysis and applications.

[6] *Lars, Landing, Graham, Wigley, Preben, Buchhave* - Optical Diagnostics for flow processes..

[7] *N. Damaschke, H. Nobach, N. Semidetnov, C.Tropea* Optical Particle Sizing in Backscatter.

[8] *W.D. Bachalo, M.J. Houser* - Phase Doppler spray analyzer for simultaneous measurements of drop size and velocity distributions.

[9] Dantec Particle Dynamics Analyzer: installations and User’s Guide.

[10] *Albrecht, Borys, Damaschke, Tropea* - Doppler and Phase Doppler Measurement Techniques.

[11] *B. Esposito* - Advances in Phase Doppler Measurements For Aircraft and Laboratory use.

[12] *Alfieri* - Caratterizzazione di Spray Simili mediante Anemometria Phase Doppler

[13] Icing Wind Tunnel CIRA: User Manual.

[14] *G. Brenn, J. Domnick, F. Durst, C. Tropea, T.H. Xu* - Phase Doppler Arrangements with Minimized Gaussian Beam Effect and Slit Effect.

[15] *T.Marchione* - Atomization and Dispersion of Sprays for Lean Premixed Prevaporized.

[16] *B. Esposito, M. Marrazzo*, “Application of PDPA System with Different Optical Configuration to the IWT Calibration”, Reno, NV, 2007, AIAA, AIAA 2007-1094

IMPACT OF A HIGH TEMPERATURE SODIUM SPRAY ON A TARGET: PDA PRELIMINARY CHARACTERIZATION.

Lucio ARANEO*, Fabio COZZI*, Giuseppe TORSELLO°, Leonardo NERICCIO°

*Politecnico di Milano, Dipartimento di Energia, via Lambruschini 4, 20156 Milano, Italy
°RSE SpA, via Rubattino 54, 20134 Milano, Italy

ABSTRACT
The behaviour of high temperature sodium when spread into air is not well known, although of capital interest in preparing safety systems in plants that use large amounts of it. A new set-up was built to produce high temperature liquid sodium sprays and jets, that were observed when produced in nitrogen inert atmosphere and in air. Sodium sprays were produced by sub-millimetric nozzles simulating a small leakage, while a rupture diaphragm of 30 millimetres diameter simulated a more severe failure. Sodium was pressurised up to 9 bar, and heated up to 550°C, while the surrounding gas, nitrogen or air, was kept at atmospheric conditions. High speed cinematography was used to observe the liquid macroscopic behaviours, while Phase Doppler Interpherometry was used to measure the sodium droplets velocity and size, when possible. Particular care was put in preparing this new experimental set-up, because of the partially unknown and potentially dangerous phenomena involved, requiring double confinement of the spray set-up and remote controlled operations. Spray macroscopic shape and some granulometric characteristics could be measured, and are reported together with occurrence of ignition.

INTRODUCTION

Liquid Sodium is already used in some applications and studied as cooling fluid for high temperature applications like in the nuclear IV Gen and fast reactors thanks to its favourable physical characteristics. Nevertheless it strong chemical reactivity requires extreme care for its use. Its liquid state temperature range is wide and quite convenient for mid and high temperature cycles, its density and viscosity are much lower than those of other low melting metals or salts, and close to water's ones, and its thermal properties values are quite attracting.

Melting Temperature	371 [K]
Boiling Temperature	1155 [K]
Density at 800 K	828 [kg m^{-3}]
Dynamic viscosity at 800 K	$2.27 \cdot 10^{-4}$ [Pa s]
Heat Capacity at 800 K	1260 [J kg^{-1} K^{-1}]
Thermal conductivity at 800 K	62.9 [W m^{-1} K^{-1}]

Table 1: Sodium physical properties, from [1]

On the other hand, sodium reacts strongly with water and oxygen, so a small leakage from a liquid sodium duct or vessel is potentially dangerous, but information about its behaviour when spread in air is quite limited or not available. Hence the present work aimed to gain basic knowledge on the evolution of a sodium jet or spray above 500°C, its shape, characteristics, granulometry, with injection pressure up to 9 bar, both in nitrogen, to avoid combustion, and in air, to observe if ignition occurs.

EXPERIMENTAL SET-UP

The injection systems

The injection systems used in the present experiment were purposely designed at RSE since commercial systems for this peculiar application do not exist. Four similar devices where built, each composed by a small pressurized recipient, a valve with a pneumatic actuator, and each one with a different nozzle.
.

Figure 1: The injection system after its use. The heater had been removed and is not shown.

All hot components are manufactured with stainless steel and can be heated up to 550°C by an electric heater controlled by a PID system connected to a thermocouple immersed into the liquid metal. The recipient has the inner volume of about 200 cm^3 containing the molten sodium, and can be pressurized up to 9 bar by nitrogen. The valve is connected directly below the recipient, and its pneumatic actuator is mounted with a spacer to keep it at lower temperature. The nozzle is nitrogen flushed while not in use to avoid its clogging. The available nozzles had 0.25, 0.40 and 0.50 mm diameter, used to produce small jets or sprays. The last system instead of the nozzle had a rupture diaphragm with 30 millimetres diameter and rupture pressure 6 bar.

The three nozzles were not designed to produce a jet or spray with specific granulometric requirements, but to generate different kinds of jet to have different characteristics to be tested.

The targets

Two different targets were used. The first target for spray testing is a flat disk (diameter 20 centimetres, thickness 2 centimetres) composed of concrete, with the aim of testing the material resistance to the sodium chemical attack at high temperature. The second target is a concrete pan (diameter 15 centimetres, thickness 2 centimetres), whose primary aim was to collect the large sodium ejection of the rupture disk test and avoid its spreading in the test cell, and at the same time to test the concrete resistance.

The controlled atmosphere test cell

A controlled atmosphere test cell was designed by RSE and used to host the experiment. It is shaped as a cube with side length 80 cm, made in stainless steel, with two large, opening and transparent observation windows, facing each other on two sides of the cube, equipped with double layer safety glasses (70x70 cm, total thickness 20 mm). Other two smaller circular window (D=100 mm, thickness 50 mm) are located on one side of the cell and are used for laser diagnostics, being equipped with high quality optical glasses already tested in combustion environment. The test cell is equipped with temperature sensors, oxygen sensor, venting lines to flush it continuously with nitrogen or air; it is not designed to withstand over pressures. Preliminary extinction tests with nitrogen showed that the oxygen content can be lowered from atmospheric condition to less than 10% in less than 20 seconds.

Figure 2: The test cell. The injection system is mounted to spray downward. The concrete target lays on the cell floor.

The "Chamber Vent Explosion" facility

The test cell and most of the measurement instrument were installed in a the "Chamber Vent Explosion" facility available at the University of Pisa, Italy. It is a large chamber designed for deflagration tests, cubic shaped with 3 meters side, built with iron walls and large safety windows. It is designed to withstand over-pressures up to 300 mbar, above which two lateral walls are detached and the chamber results fully vented to the atmosphere. The chamber is mounted on rail to translate it easily outside of the laboratory building to allow its use in open field. All operations are remoted in the control room inside the laboratory.

Figure 3: The "Chamber Vent Explosion" inside the laboratory.

The high speed recording system

To record the experiment, the high speed video camera available at the Politecnico di Milano, Department of Energy, was used. It is a Phantom V5.1 camera, equipped with a 1.2 Mpixel CMOS sensor, capable of a frame rate up to 1200 Hz at full resolution, with tuneable exposure time. It has 4 GB of on board memory to temporary store the images, and a GLan connection to transfer the data to a PC.

High speed imaging requires illumination with high power and stability, the risk being to observe the 100 Hz light fluctuation caused by the 50 Hz mains supply. Lighting was provided by one 800W 220V halogen lamps, having a large filament with sufficient thermal inertia to attenuate the 50 Hz oscillation, and two 100 W 12V DC halogen lamps. All lamps were switched on few seconds before the experiment to avoid window overheating.

A traditional video recorder and closed circuit TV are used to monitor and record the tests from the control room.

LDV and PDA instrumentation

A combined LDV + PDA system set-up was used for this experiment.

The laser source used is a continuous Melles Griot 43 series Argon-ion laser used at its maximum power of 300 mW. The optic hardware is made by Dantec, and comprises a Bragg cell and beam splitter system, a Fiber LDV transmitting optic with integrated back-scatter receiving optic, a Fiber PDA receiving optic, a 58N70 Detector Unit with the photomultipliers, an additional external photomultiplier, a 2D BSA P60 Flow and Particle Processor, and a PC with the acquisition software. The optics were mounted on a traverse system for easy and remote positioning of the measurement point.

The sprays to be analysed were not known a-priori, and it was not know if spherical particles had to be expect, allowing to measure their diameter by the PDA, or other kind of particles of which only the velocity could be measured. In any case, the tests were limited, so all possible data had to be acquired to obtain better statistics. Form this last point of view a back scatter LDV system has a larger measurement volume, the whole two beams intersection region, while the PDA optics uses only a narrow section of it [2, 3], thus decreasing the sampled data. The strategy was to implement both systems at the same time.

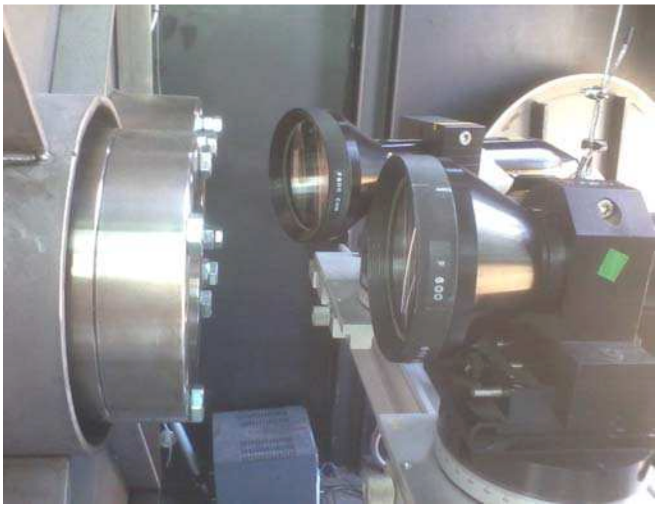

Figure 4: The optics: in front the PDA receiver, behind the LDV transmitter.

A traditional PDA system was set-up; with its receiving optics and detector unit. The spray axial velocity is measured a first time by the acquisition channel 1 (1st photomultiplier and 1st FFT processor board); the channels 2 and 3 are used together with channel 1 to measure and verify the particle diameter. A fourth external photomultiplier and the processor 4th board, normally used to measure a different velocity component, were here used to measure the axial velocity component from the particles seen by the back-scatter lens of the transmitting optics. In the following text, the two measured velocity will be called LDV-velocity (or LDA-1 by the Dantec software, from Laser Doppler Anemometry board 1), and PDA-velocity (or LDA-4); they are in principle the same axial velocity component of the particle seen by the two optics, with lower probability to detect particles by the PDA system, and also lower validation because non spherical particles are discarded.

Table1: LDV and PDA set-up

Laser: argon-ion, used on the green line (514.5 nm), for axial velocity component and diameter measurement
Bragg cell frequency (frequency shift): 40 MHz
Transmitting (and LDV receiving) optic focal length: 600 mm
Beam separation at the frontal lens: 38 mm
Nominal beam diameter ($1/e^2$) at the frontal lens: 1.35 mm
Nominal measurement volume size 290 290 9000 μm
Velocity range: -10 ÷ 30 m/s
PDA Receiving optic focal length: 600 mm
Scattering angle: 150º
Sensor order: reflection
Sensor aperture: mask A
Diameter range: up to 900 μm,

EXPERIMENTAL RESULTS

Preliminary test with water

To acquire some preliminary information about the jet brake-up pattern, few preliminary test were conducted at the Politecnico di Milano Department of Energy, on the three available nozzles, using water as test fluid. Since liquid sodium rheological properties are quite similar to water's ones, it can be expected that similar patterns, particle or droplet with similar velocity and diameters will be produced when using liquid sodium.

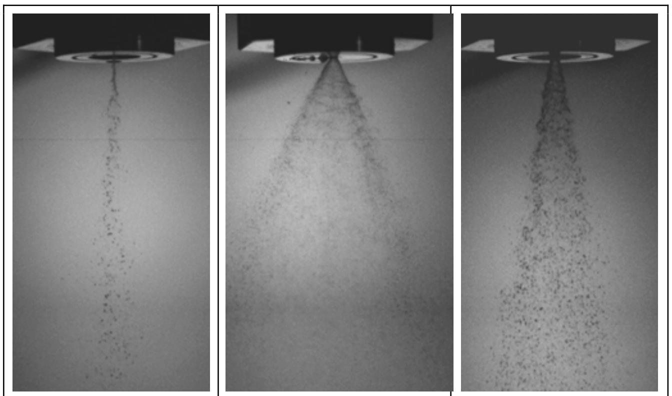

D=0.25mm, 3 bar | D=0.40mm, 9 bar | D=0.50mm, 9 bar

Figure 5: The three nozzles tested with water at different pressures. The nozzle cylindrical body has external diameter 20 mm

The PDA measurement volume was located along the geometrical injector axis, 80 millimetres downstream of the nozzle.

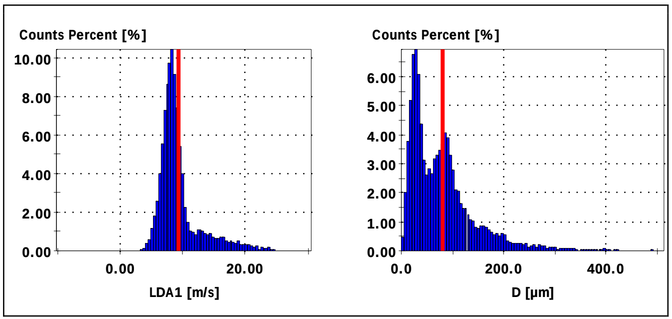

Figure 6: Nozzle D=0.50mm: example of velocity and diameter histogram with water at 9 bar.

Test with liquid sodium, overview

Five test were conducted on the four available injectors. The ambient gas, nitrogen or air, was always at atmospheric pressure and temperature (25-35°C).

Nozzle 0.25 was tested in nitrogen, with sodium at 550°C, 3 bar gauge (relative) pressure.

Nozzle 0.50 was tested in nitrogen with sodium at 550°C, 9 bar gauge pressure.

Nozzle 0.40 was tested in air, with sodium at 550°C, 9 and 6 bar gauge pressure.

The rupture diaphragm was tested in air, with sodium at 500°C, 6 bar gauge pressure. Ignition occurred only in this test.

For each test condition the results presented, are still images to observe the spray or jet pattern, LDV and PDA results, if available, and some comments and comparison with water results. The PDA measurement volume was located along the geometrical injector axis, 80 millimetres downstream of the nozzle. This distance is different from that of the water tests since the optical windows aperture of the test cell limited the accessible region of the spray.

Nozzle 0.25, in nitrogen, sodium at 3 bar

This nozzle was quite small, and got clogged quite soon. The jet produced showed a break-up process in the Rayleigh regime, with few particles produced with size comparable or larger than the nozzle diameter. PDA measurement gave no results since the few droplet produced did not cross the measurement volume. Few LDV results measured few particles at 15 to 20 m/s (where Bernoulli limit is 27 m/s), and a dozen of nearly standing particles.

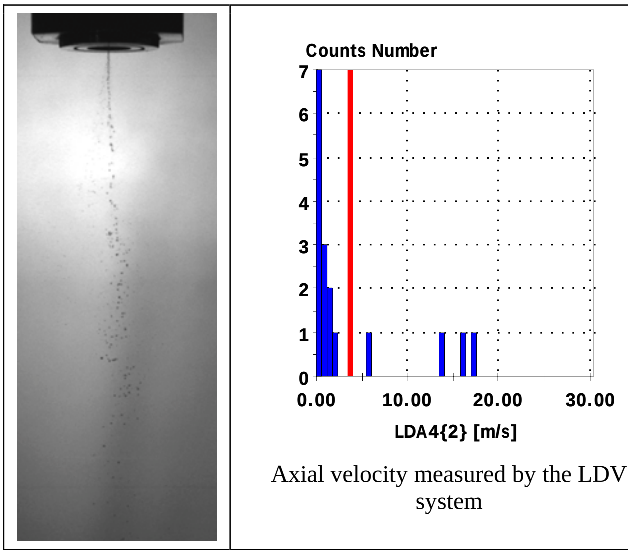

Axial velocity measured by the LDV system

Figure 7: Results from Nozzle 0.25 mm, in nitrogen, sodium at 3 bar.

The atomization pattern is quite similar to the one obtained with water, with larger particles and poor atomization. No immediate chemical reactions were observed on the concrete target.

Nozzle 0.50, in nitrogen, sodium at 9 bar

The spray produced in this test was successfully measured with all the techniques used. The initial liquid break-up generated a conical sheet and then a spray; after few seconds the atomization became poor and switched to the Rayleigh break-up regime [4].

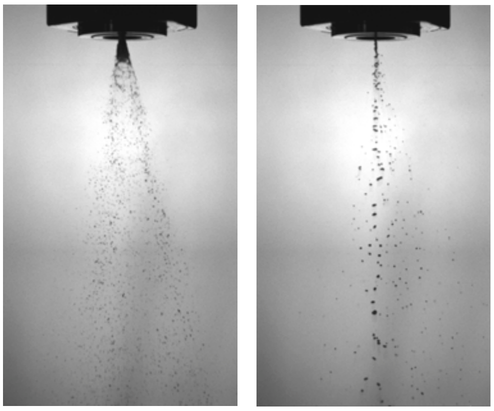

Figure 8: Two images from Nozzle 0.50 mm, in nitrogen, sodium at 9 bar. Initial spray (left) and after few seconds (right)

The LDV and PDA systems sampled enough droplets to calculate meaningful statistic values, presented by histograms. Axial velocity ranged up to 30 m/s, with the average value around 12 m/s. Droplet diameter show the typical spray log-normal distribution, here with a peak around 120 microns and maximum measured value up to 900 microns. The average calculated moments are: D_{10} = 177 µm, D_{20} = 240 µm, D_{30} = 301 µm, D_{32} = 472 µm (for a definition of droplet moments refer e.g. to [4, 5, 6]).

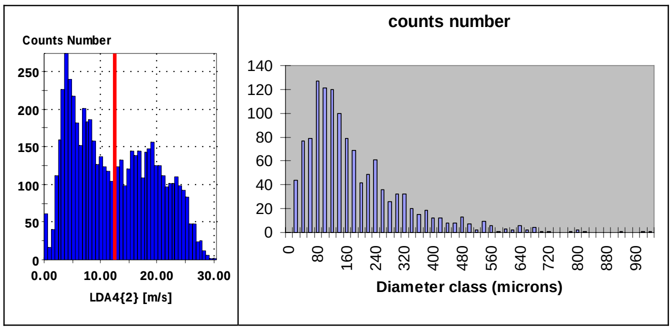

Figure 9: Velocity (LDV) and Diameter (PDA) histograms from Nozzle 0.50 mm, in nitrogen, sodium at 9 bar.

The initial spray angle is similar to that obtained with water, but with larger particles, then the nozzle probably started to get clogged.

Nozzle 0.40, in air, sodium at 9 and 6 bar

The break up pattern of this jet showed the typical behaviour of a swirled spray development. Compared to water, the spray angle is narrower and the particles are larger. The particle shape is not always spherical, probably the fast cooling in cold air is affecting the liquid viscosity and surface tension.

The sodium pressure was then lowered to 6 bar without interruption, and the spray kept stable for a few seconds, but no images are available since the camera memory was full. Later the nozzle started clogging, and the shape of the jet turned to something similar to an extrusion of high viscosity liquid, with a residual swirl, as shown by the following figures.

Figure 10: Images from Nozzle 0.40 mm, in air, sodium at 9 bar. initial spray development

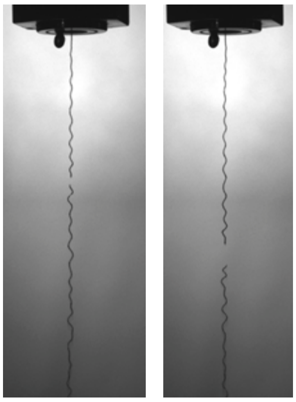

Figure 11: Images from Nozzle 0.40 mm, in air, sodium at 6 bar. Nozzle getting clogged. A small leakage is also visible close to the nozzle.

The LDV system collected sufficient data during the spraying stage, with velocity ranging from 0 to 25 m/s. The time evolution clearly shows the velocity decrease when passing from 9 to 6 bar; in the histograms this appears as two peaks around 16 and 25 m/s.

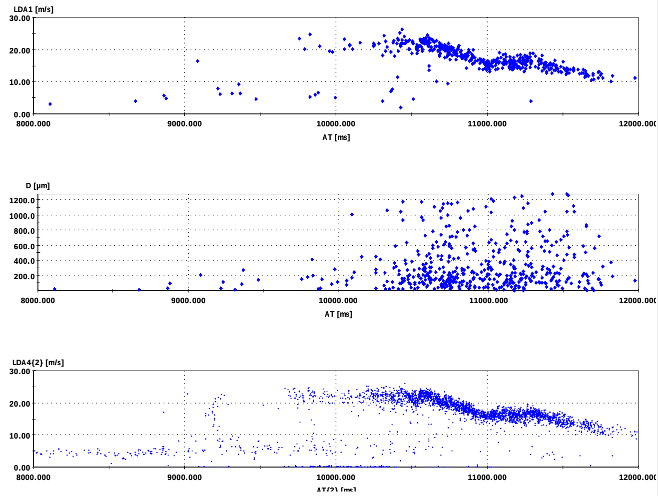

Top; PDA velocity (m/s)
Centre: PDA Diameters (µm)
Bottom: LDV velocity (m/s)

Figure 12: Results from Nozzle 0.40 mm, in air, sodium at 9 and 6 bar. Velocity and diameter time evolution. Each dot is one detected particle.

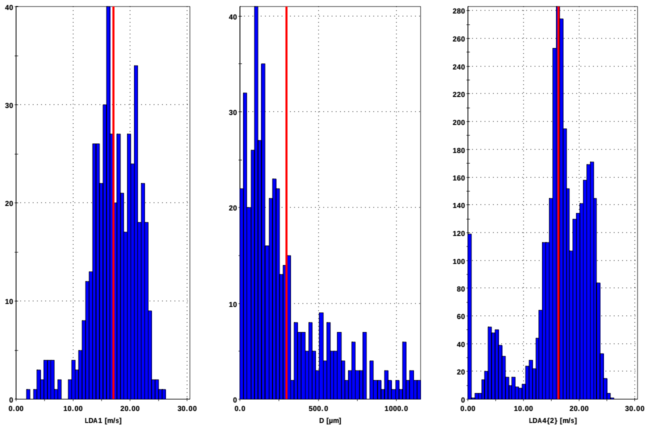

PDA velocity (m/s) PDA Diameters (µm) LDV velocity (m/s)

Figure 13: Results from Nozzle 0.40 mm, in air, sodium at 9 and 6 bar. Velocity and diameter histograms

The velocity data form LDV and PDA are well matching, with LDV data being 10 times more numerous. Diameters went slightly out of range, so accurate average values can not be calculated

It is important to note that no ignition occurred in this test in air.

Rupture diaphragm, in air, sodium at 6 bar

For this test the LDV-PDA system was removed, since no particles suitable for this instrument can be expected, while the large amount of sodium to be ejected at once would have exposed the instrument to useless risks.

The collecting pan placed below the injector was also surrounded by glass-wool to reduce possible spreading of sodium droplets toward the observation windows.

Ignition started already from a small leakage before reaching the target temperature of 500°C. When pressure was applied and the diaphragm broke, ignition occurred in many point of the jet before it could reach the collecting pan, that is in less than 10 ms. After 20 ms the ignition had propagated to most of the jet. After 30 ms all the ejected sodium was burning, the video camera was completely saturated and could not deliver useful images for 1 second, after which a flame was clearly visible inside the collecting pan, but image quality was lowered by the deposition of smoke on the observing window. Than the cell was purged with nitrogen up to flame extinction.

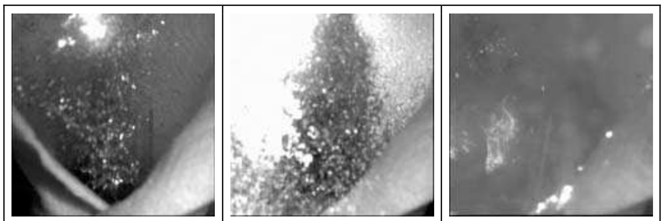

10 ms, first ignition points
20 ms, ignition spreading
1 s: flames inside the collecting pan

Figure 14: Images from the Rupture Diaphragm, in air, sodium at 6 bar. Time is given approximatively after the rupture.

CONCLUSION

A first test was performed on liquid sodium with high speed cinematography and Laser Doppler and Phase Doppler measurements. The procedure and the measurement systems were successfully implemented, with a new peculiar

LDV+PDA implementation that can be easily obtained with the commercial existent instruments. The results show that the molten sodium in some condition behaves like water as regard the break-up patterns, but poorer atomization and larger particles. Velocity and size of sodium droplet are measured for the first time. About the ignition, it did not occur when the injected sodium flow was quite small, while it occurred immediately and strongly when a large amount of sodium was delivered at once.

ACKNOWLEDGMENT

This work has been financed by the Research Fund for the Italian Electrical System under the Contract Agreement between RSE S.p.A. and the Ministry of Economic Development - General Directorate for Nuclear Energy, Renewable Energy and Energy Efficiency stipulated on July 29, 2009 in compliance with the Decree of March 19, 2009

The authors would like to thank the University of Pisa, Prof. Carcassi, for hosting the test on liquid sodium in their laboratory, and the University of Bergamo, Prof. Cossali and Prof. Marengo, for providing many components of the PDA system.

REFERENCES

[1] Fink, J. K., Leibowitz, L., *Thermodynamic and transport properties of sodium liquid and vapor*, Argonne National Laboratory Report ANL/RE--95/2, DOI 10.2172/94649, 1995.

[2] Albrecht H. E., Damaschke N., Borys M., Tropea C., *Laser Doppler and Phase Doppler Measurement Techniques*, Springer 2003, XIV, ISBN: 3-540-67838-7

[3] Dantec Measurement Technology A/S; *Particle Dynamics Analyser, Installation & User's guide*, Publication n. 9040U1101, Dantec MT A/S, Skovlunde, Denmark, 1999.

[4] Lefebvre A. H., *Atomization and Spray*, Hemisphere Publishing Corporation, 1989.

[5] Sauter J., *Die Grössenbestimmung der in Gemischnebeln von Verbrennungskraftmaschinen vorhandenen Brennstoffteilchen* VDI-Forschungsheft Nr. 279 (1926) and Nr. 312 (1928).

[6] Mugele R. A., Evans H. D., *Droplet Size Distribution in Sprays*, Ind. Eng. Chem., 1951, 43 (6), pp 1317–1324, DOI: 10.1021/ie50498a023.

DIPSI Workshop 2011 on Droplet Impact Phenomena & Spray Investigation
May 27, 2011, Bergamo, Italy

DROP IMPACTS IN POOLS: A COMPARISION BETWEEN HIGH SPEED IMAGING AND NUMERICAL SIMULATIONS

S. Fest-Santini*, M. Guilizzoni°, M. Santini*, G.E. Cossali*

* Department of Industrial Engineering, University of Bergamo, viale Marconi 5, 24044 Dalmine (BG), Italy
° Department of Energy, Politecnico di Milano, via Lambruschini 4, 20156 Milan, Italy

ABSTRACT
A feasibility study is done aimed at verifying the capabilities of the open source CFD package OpenFOAM® to predict the dynamic crater evolution and accompanying phenomena during drop impact into deep pools in the cratering regime. Two experimental test cases are chosen, whose crater evolutions are in one case influenced and in the other not influenced by wall effects, so that 2D and 3D domain geometries are respectively required. OpenFOAM® seems to be a promising tool to predict drop impacts already with standard solver settings, even if the finest and most dynamic accompanying phenomena, which also can affect the crater shape, could not be correctly predicted. This may be due to limits in the implemented models and to memory and, thereby, mesh limitations with the present numerical set-up.

INTRODUCTION

The cratering regime with his manifold characteristics like micro-entrapments [1], primary entrapment which could lead to the trampoline phenomena [2], vortex rings [3], micro-jetting [4] and thick jets [5] is chosen as a study case for a comparison between high speed imaging and numerical simulations. This study is aimed at verifying the capabilities of CFD software packages as they are, with simple settings and performing simulations on a common personal computer without the need for a cluster. The OpenFOAM® open source CFD package was selected because of its large community of users and successful examples of use of its two-phase *interFoam* solver in the fields of drop splashing and impact as reported in literature [6-9].

Two characteristic drop impacts which feature micro-entrapments, primary entrapment and trampoline phenomena are selected as test cases. Hereby, the impact points are varied. One impact point is fixed far enough from the pool walls that the latter have no influence on the crater evolution. On the contrary in the second test case, the distance between the impact point and the camera-facing pool wall is reduced, so that wall effects on the crater evolution can only be neglected for the initial stage of drop impact. The benefit of the reduced distance between impact point and wall is that it allows a much more detailed observation of the phenomena happening within the droplet, as shown in fig. 1.

Figure 1: Differences in the experimentally obtained level of detail for the two test cases: crater evolution without (left) and with (right) wall effect for later stage of drop impact.

MATERIAL AND METHODS

Experimental procedure

Drop impact experiments are carried out at the Department of Industrial Engineering, University of Bergamo, whereby the high-speed visualisation techniques with continuous back-light illumination is used to observe droplet impacts into a pool of the same liquid. Water droplets of millimetric size are produced with an on-demand droplet generator. Droplets exiting the generator are accelerated by gravity and impact in the pool, whose horizontal alignment is achieved by a 6-jack platform with precision of ±10 μrad.

Special accuracy is required in the alignment of pool's water level and camera position in relation to the water level. Otherwise, refractive and alignment distortions or black stripes within the images due to liquid interfacial phenomena with the pool walls (meniscus) appear. It is worth noting that the dimension of black stripes depends also from the thickness of the pool walls and can only be avoided by a correct and constant water level in the pool. Thereby, the pool is connected to a level water container mounted on a micrometric stage. The micrometric stage allows a precise regulation of the water level, whereby the large surface area of the level pool guaranties its constancy during experiments. Additionally, the camera is mounted on a tilting, rotating and movable platform, so that its lens axis can be independently adjusted.

The recorded images are post-processed to obtain the crater interface as function of time. Hereby, the algorithm comprises background subtraction, contrast enhancement, image cleaning and edge detection using the Laplacian of Gaussian (LoG) method and feature detection. The contrast enhancement including lower and high upper limits of the intensities setting and the intensification factor are adapted to the detected information. Each experimental investigation is analysed by extracting the following information: (a) impact velocity and diameter using the frames before drop impact, (b) crater interface contour as function of time and (c) the contour of entrapped air bubbles as a function of time. The extracted crater interfaces are used to calculate crater depths and widths for each recorded time step after impact. Velocity trajectories of the micro-entrapments, which are detected during the early stage of drop impact, are calculated from their extracted contours.

Numerical simulations

Numerical simulations are performed at the Department of Energy, Politecnico di Milano, using the finite volume two-phase solver *interFoam* of the OpenFOAM® 1.7.1 open source CFD toolbox distributed by OpenCFD® Ltd. The solver implements an improved Volume of Fluid (VOF) model based on a two-fluid approach, with the continuum surface force (CSF) model to include surface tension at the interface. Interface compression is performed to get a sharper contour between the phases. Coherently with the scope of this work, standard solver setting and no adaptive grid refinement are used. The surrounding air, the drop and pool water are assumed Newtonian and incompressible and the flow laminar. For each phase the values of all relevant thermophysical properties are taken at the respective temperature measured during the experiments. Initial positions and conditions of the two phases are fixed using the *setFields* and *funkySetFields* OpenFOAM® utilities.

2D axisymmetric simulations are performed in the study of the case without wall effects and 3D domains are considered - exploiting symmetry planes where possible - for the second study case, where wall effects need to be taken into account during the later stage of drop impact. For axisymmetric simulations, the drop is let fall from a height corresponding to the experimental one. To reduce the domain dimensions, in 3D simulations the drop is on the contrary directly placed near the free surface of the pool with an initial velocity equal to the one it would reach falling from the corresponding experimental height (neglecting air drag).

In both cases the mesh is structured, made by rectangular hexahedra in the 3D case, by wedges in the axisymmetric case. The number of cells and the average cell volume (cell area in the axisymmetric case) are reported in tab. 1.

In general, the mesh is graded at least in one direction, so that the cell volume is not uniform. Different meshes are tested to analyse the sensitivity of the solution to the mesh size and their details are summarised in tab. 1.

Table 1: Mesh details for the 2D axisymmetric and 3D domains. The colours correspond to the ones used to trace the boundary between the phases in figs. 3 and 5.

Case code	Cell. Number $(\cdot 10^{-6})$	Domain extension [m] (D x W x H)	Domain volume [m^3]	Avg.cell. volume [m^3]
3D-C	4.200	0.040 x 0.030 x 0.014	1.68e-05	4.00e-12
3D-I 3D-I	4.608	0.018 x 0.012 x 0.012	2.59e-06	5.62e-13
3D-F	5.400	0.015 x 0.009 x 0.009	1.22e-06	2.25e-13
2D	1.000	0.020 x 0.025	5.00e-04	5.00e-10

The boundary conditions are defined as followes:

- wall boundary for the front, back, bottom and external sides of the pool;
- open boundary for the top of the domain (“atmosphere”);
- axial symmetry for the axis in the axisymmetric case and
- symmetry plane for the internal “side” of the mid-pool in the 3D case.

The time step is adapted by the solver to keep the Courant number under 0.5 and to output the solution at the desired time intervals matched to the experimental time steps.

Figure 2 shows the two domains with the corresponding initial configuration of the phases.

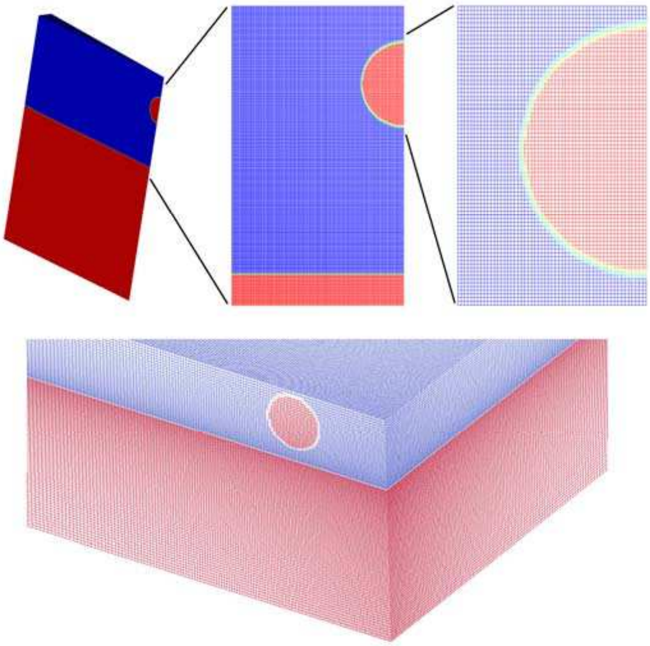

Figure 2: Mesh and initial configuration of the phases for the two investigated test cases

RESULTS

Crater evolution without wall effect

In fig. 3, the phase contours of the numerically simulated axisymmetric drop impact are superposed to the experimentally obtained images, showing a quite good qualitative agreement. While the crater is formed in the target liquid, a swell rises up on its base and propagates on the liquid surface. This quite thick rim is slightly overestimated in terms of initial height and elongation. The elongation overestimation becomes more pronounced with increasing time after impact. On the contrary, the crater contour is well described at the initial and final stage of drop impact, whereas the intermediate stage of the crater evolution dynamic is affected by the trampoline phenomena. A series of capillary waves propagates up the impacting drop and converges at its top, pinching off a smaller secondary drop. As shown in more detail in fig. 5, the secondary drop falls onto the bottom of the crater and is then ejected by the receding crater. This phenomenon could not be captured by the simulations and consequently the simulated crater contour does not reflect the characteristic crater shape. In preliminary simulations of other cases, secondary drop ejection was obtained. Therefore the failure in the present case may be due to the rough capture of the crater shape at the end of its deepening, which influences its retraction and trampoline behaviour.

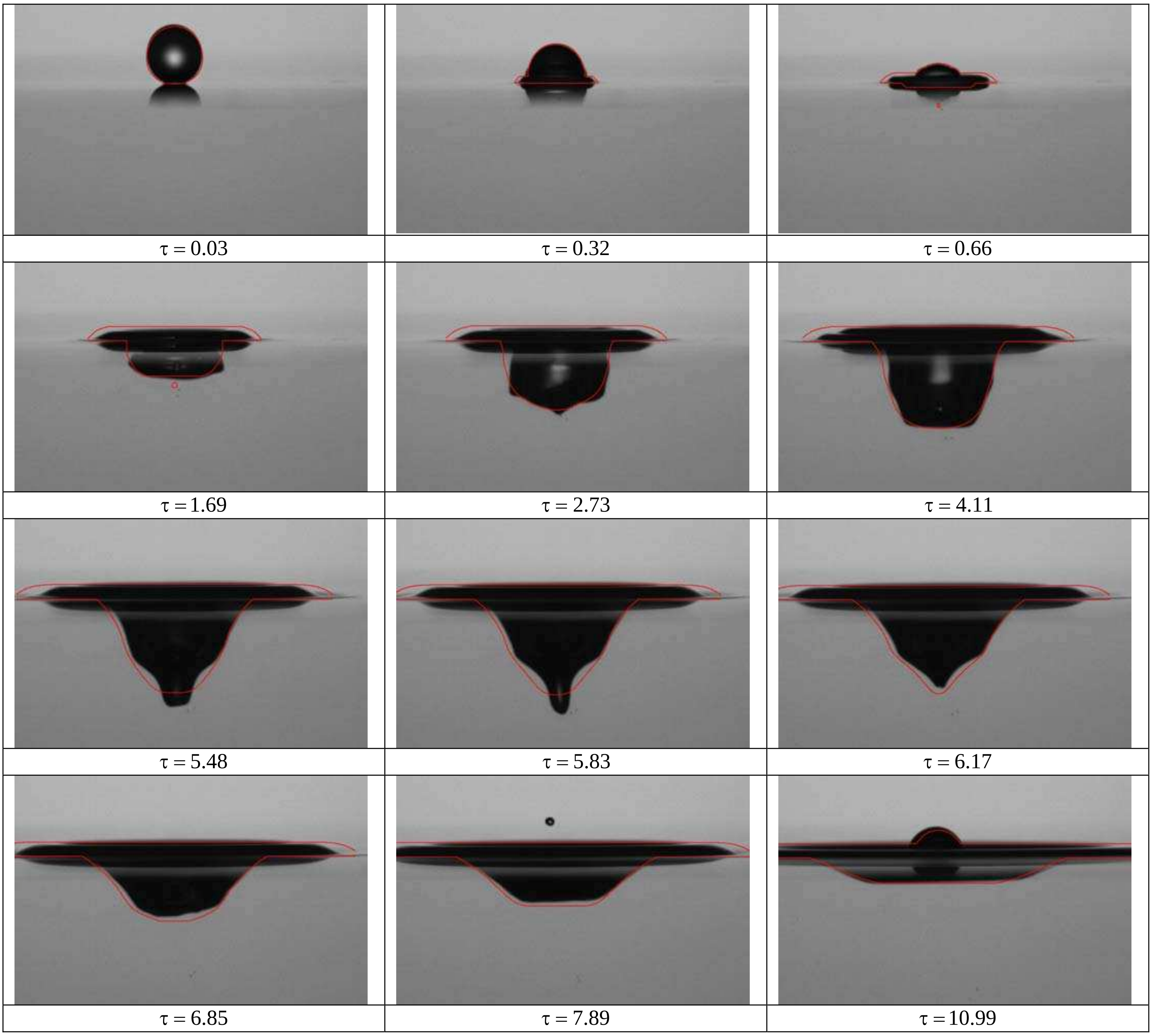

τ = 0.03 τ = 0.32 τ = 0.66

τ = 1.69 τ = 2.73 τ = 4.11

τ = 5.48 τ = 5.83 τ = 6.17

τ = 6.85 τ = 7.89 τ = 10.99

Figure 3: Superposition of experimentally [2] and numerically obtained dynamic crater evolution in the cratering regime (d = 2.8 mm, v = 1.24 m/s, We = 54, Fr = 52).

The final stage of drop impact, which is characterised by the formation of a dome, is described in well agreement with the experimental data.

Crater evolution with wall effects

The distance between the wall and the drop impact point is reduced to be able to capture in the experimental images more details about the phenomena within the drop. As already mentioned, the crater evolution is influenced by the presence of the camera-facing pool wall, as it is shown for example in fig. 4. A 3D-simulation approach is required and consequently, more computer resources are needed. Thereby, different domain sizes, cell sizes and cell numbers are analysed as reported in tab. 1. With decreasing cell size, the required time step becomes smaller to respect the limit on the Courant number, so that the simulation time suffers from a significant increase. Simulations with finer mesh are therefore performed only for initial stage of drop impact, whose solution depends significantly from the mesh. For example, the coarser mesh - indicated in blue in fig. 5 - does not capture the entrapped micro-bubbles.

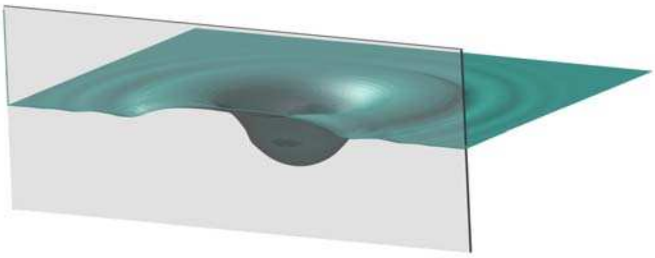

Figure 4: A simulated frame (rendered using POV-Ray®) showing the influence of the camera-facing pool wall on the crater evolution.


τ = 0
τ = 0.23
τ = 0.93
τ = 1.39
τ = 1.85
τ = 2.32
τ = 2.78
τ = 3.24
τ = 3.71
τ = 4.17
τ = 4.63
τ = 5.10
τ = 5.56
τ = 6.02
τ = 6.49
τ = 6.95
τ = 9.03
τ = 10.19

Figure 5: Superposition of experimentally and numerically obtained dynamic crater evolution influenced by camera-facing pool wall in the cratering regime ($d = 3.35$ mm, $v = 0.81$ m/s, $We = 31$, $Fr = 20$). Different mesh sizes are used as summarised in Tab. 1.

As already reported for the 2D simulation, the trampoline phenomena could not be predicted. Thereby, the numerically obtained crater shape differs in terms of depth as well as rim height with respect to the pool surface. In summary, all the different meshing strategies lead to an underestimation of the maximum crater depth and an overestimation of the maximum crater width. For a correct evaluation of the simulation performances, it must be also underlined that a significant problem is the correct superposition of the numerical results on the experimental frames. Difficulties arise from different refraction indexes between air and water and results in different scales of the droplet in air and water. Moreover, a major issue is that synchronization is done manually by measuring the distance of the drop from the pool free surface in a suitable picture and converting it into a distance which is used for initialization of the drop position in the simulations. The same principle holds for the determination of the drop diameter and shape. Unfortunately, a small error in these parameters has a significant influence on the results: as an example, for case H40I the red and the orange contours represent results from the same simulation but the latter shows the contours half an experimental time step after the red ones.

Figure 6 shows the comparison between the experimentally detected and numerically predicted crater width and depth. It can be noticed how the agreement reflects the above mentioned considerations and is fairly good in the case of the axisymmetric simulation, while for the 3D larger deviations are observed.

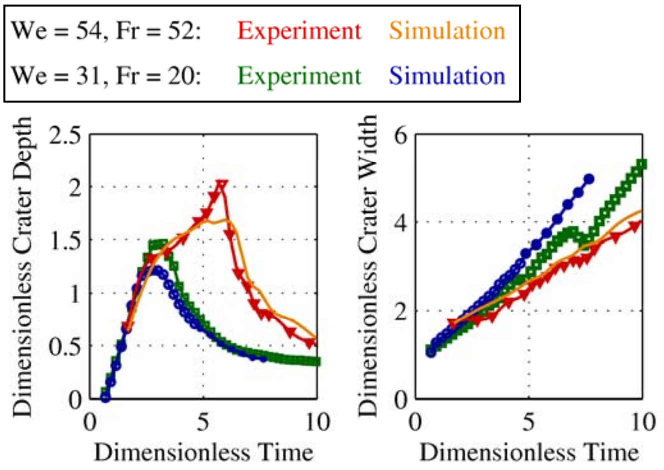

Figure 6: Comparison between the experimentally detected and numerically predicted crater width and depth.

Micro-entrapment

At the initial stage of drop impacts, micro air bubbles can be formed, when a thin air sheet remains entrapped between the two contacting liquid surfaces. For the dimensionless time step $\tau = 0.23$ of fig. 5, the two observed micro-bubbles are highlighted in fig. 7. They feature an average size of $0.03\,\mathrm{mm}^2$. In fig. 7, their droplet contours and the corresponding velocity vectors are plotted with respect to their impact point . The upper micro-entrapment, pointed out in blue, seems to be influenced by the crater evolution; the lower bubble, marked in green, may be decelerated by the bulk liquid. The propagation direction of both is properly affected by a vortex ring visible dying the impacting drop [2].

The phenomena of entrapment and rupture of a thin air sheet is also captured in the 2D and 3D simulations, even if the agreement with the experimental observations is only qualitative. Figures 8 and 9 show how air is trapped under the drop and the dynamics of the resulting bubble, “chased” by the crater which in the end reaches and captures it. The simulation may offer an insight of what happens (fig. 9): the thin film of trapped air, stretched during the impact, retracts due to surface tension thus creating an initially "eight-shaped" bubble. If the bubble neck becomes too thin, fragmentation in two bubbles occurs. Otherwise the bubble evolves towards more spherical shapes.

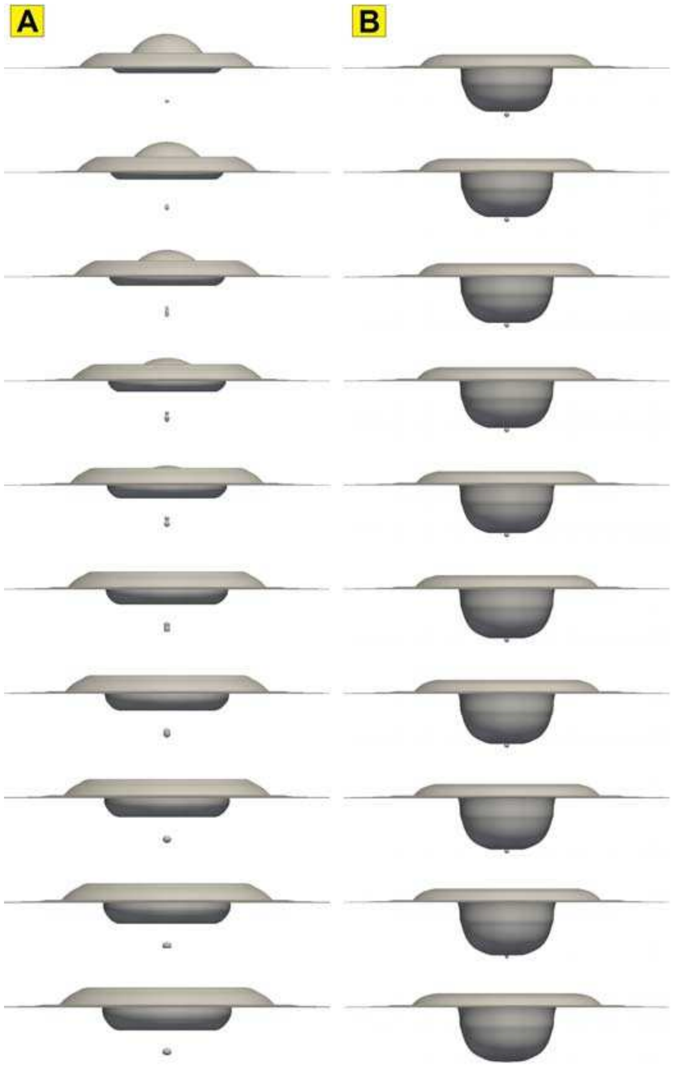

Figure 8: Dynamics of the air trapped under the crater, which at the end is reached and captured by it. The time step between the frames in each sequence is $1e^{-4}$ s.

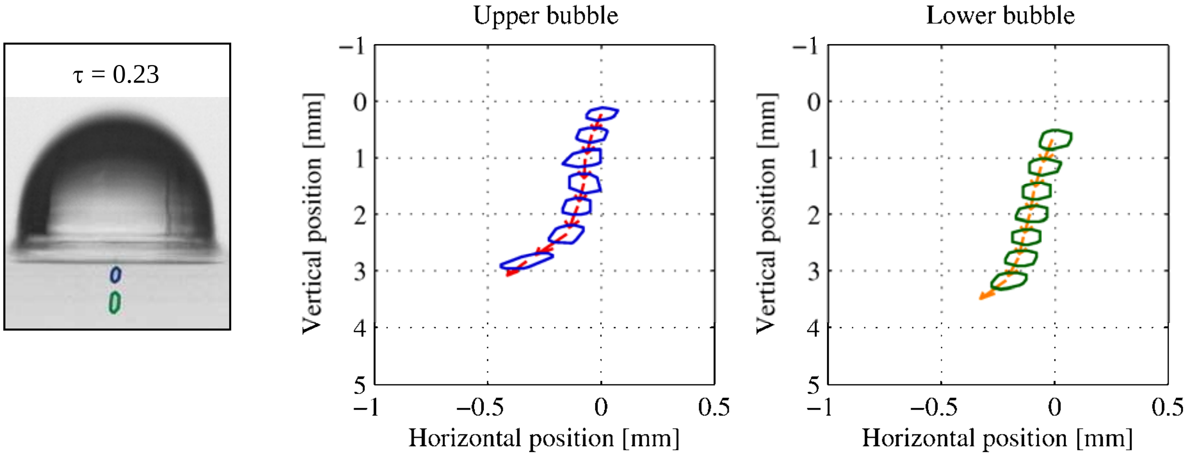

Figure 7: Contour and velocity vector of micro-entrapments at the initial stage of drop impact

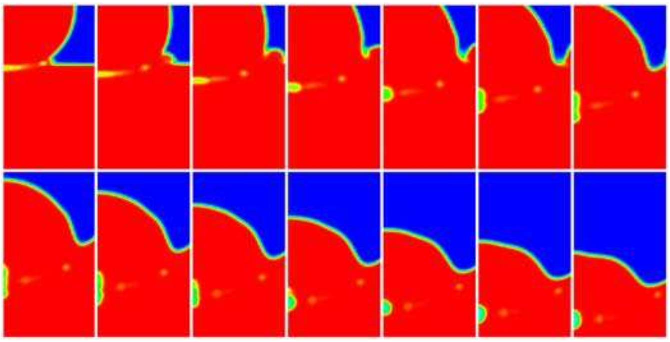

Figure 9: Details of the air dynamics (green region) in the first instants after the drop impact. The time step between the frames is $2e^{-4}$ s.

CONCLUSIONS

A comparative study of experimentally and numerically obtained drop impacts into deep pools in the cratering regime was performed. The feasibility of the use of the *interFoam* solver of the OpenFOAM® CFD toolbox was tested using “default” solver settings, basic meshing of the domain and a standard personal computer. The *interFoam* solver seems to be a very promising tool for the simulation of drop impacts into pools, although the highly dynamic processes like the trampoline phenomena could not be numerically predicted. Probably, the description of these phenomena requires a finer mesh, whose size was actually limited by the available memory. Thereby, it is planned to refine statically or adaptively the mesh geometry and to use a cluster. Furthermore, the analysis will be extended to the influence of the impacting drop shape.

NOMENCLATURE

Symbol	Quantity	SI Unit
d	diameter	m
Fr	Froude numer	-
v	velocity	m/s
We	Weber number	-
τ	dimensionless time	.

REFERENCES

[1] S.T. Thoroddsen, T.G. Etoh, K. Takehara, Air entrapment under an impacting drop, *J. Fluid Mech.*, vol. 478, pp. 125–134, 2003

[2] A. Bisighini, Single and double drop impact onto a deep and thick liquid layer, Ph.D. Thesis, University of Bergamo, 2009

[3] F. Rodriguez, R. Mesler, The penetration of drop-formed vortex rings into pools of liquid, *J. Coll. Int. Sci.*, vol. 121 (1), pp. 121-129, 1988

[4] M. Rein. The transitional regime between coalescing and splashing drops. *J. Fluid Mech.*, vol. 306, pp. 145–165, 1996.

[5] J.L. Liow, Splash formation by spherical drops, *J. Fluid Mech.*, vol. 427, pp. 73–105, 2001

[6]. Berberović, N.P. van Hinsberg, S. Jakirlić, I.V. Roisman, C. Tropea, Drop impact onto a liquid layer of finite thickness: Dynamics of the cavity evolution, *Phys. Rev. E 79*, 036306, 2009

[7] A.B. Costa, R. Graham Cooks, Simulated splashes: Elucidating the mechanism of desorption electrospray ionization mass spectrometry, *Chemical Physics Letters*, vol. 464, pp. 1-8, 2008

[8] I.V. Roisman, C.M. Weickgenannt, A.N. Lembach, and C. Tropea, Drop impact close to a pore: experimental and numerical investigations, *23rd Annual Conference on Liquid Atomization and Spray Systems*, Brno, Czech Republic, September 2010

[9] E. Berberović, Investigation of Free-surface Flow Associated with Drop Impact: Numerical Simulations and Theoretical Modeling, Ph.D. Thesis, TU Darmstadt, 2010

DROP IMPACT ON POROUS MEDIA

A.N. Lembach, I.V. Roisman and C. Tropea

Center of Smart Interfaces
Institute of Fluid Mechanics and Aerodynamics
Technische Universität Darmstadt, Petersenstr. 32, 64287 Darmstadt, Germany
lembach@csi.tu-darmstadt.de, +49 6151 16 6606

ABSTRACT

This experimental study describes a drop of liquid impacting onto a porous substrate. The interest is on the drop behavior above the surface and especially underneath. There are several applications where this phenomenon plays a major role, like ink jet printing or spray coating. There are already several studies available [1-13], looking at the final state of an absorbed droplet, or simulating the process numerical. For the first time it is now possible to observe the liquid motion above and underneath simultaneously. The liquid has the same refraction index as the porous medium. This, and a small porous depth in the light path gives a clear image of the filled volume inside. This parametric study is comparing the penetration with the Washburn equation[14] and is describing general tendencies. It is shown that different wetting regimes exist and influence the penetration.

INTRODUCTION

Ink jet printing, penetration of rain into walls of a building, needle less injection, coating of porous materials, irrigation of fields, these are all examples for applications which include a drop impacting on a porous media. In Fig. 1 a sketch of the general outcome is shown. The drop spreads on impact, resulting in a thin film with a thick rim, just like an impact on a flat impermeable substrate. If the impact velocity reaches a critical limit, several droplets will emerge through splash [15]. Depending on the porous medium the drop will penetrate fast or slow. This study gives some new insight into this process. Until now only Magnetic Resonance Imaging or X-ray were possible options to see inside the porous medium, but these are either too slow or don't provide enough resolution to observe an impacting drop. A new method is presented in the study at hand. In Fig. 2 a typical series of images obtained in this study is shown.

The Washburn equation [14] is probably the first description of a liquid drop penetrating the substrate without any impact beforehand.

$$= \frac{\sigma \cdot \qquad \cdot}{\cdot \mu} \qquad (1)$$

Where L is the penetration length, σ the surface tension, D_{Pore} the pore diameter, t the time and μ the dynamic viscosity.

POROUS TARGETS

The porous targets used in this study are made from microscope slides and glass beads. A slit of 1.2 mm is formed with the microscope slides and filled with the glass beads. The slides are glued with 'Thermokitt' a ceramic two component glue, which can withstand high temperatures. The glass beads are filtered to obtain only spherical beads and a small range of diameters. Inside the slit the beads are shaken with an ultrasonic vibrator in order to obtain almost perfect packing. This procedure results in a porosity of $\phi = 0.36$. Since only spheres are used for the target production, the porosity is the same for the different sizes. To prevent any movement of the beads during the experiments the targets are sintered. Due to the liquid-glass-transition it is not easy to maintain the right combination of temperature-time curve. With constant 735 °C for one to two hours and a cool down for several hours, it is achieved to connect the beads just at the contact points, while keeping them almost perfectly spherical. Most critical is the cool-down. If done too fast, the immediate result is cracking of the microscope slides. Due to the short sintering the microscope slides will not melt together, but will bend if not supported. The exact time and temperature values depend on the oven used and on the target and glass bead size. In Fig. 3 a typical target is shown.

EXPERIMENTAL PROCEDURE

A sketch of the experimental setup can be seen in Fig. 4. Drops are released from a syringe in different heights resulting in different impact velocities. The impact on the porous targets is illuminated with a LED light source. The light is parallelized with a lens, resulting in a perfectly white background for shadowgraphy. On the other side of the target, the process is captured by a high speed camera at about 10kfps. This way the impact process is captured above and underneath the surface at the same time. Only the perfect brightness setting can be different for above and underneath, since the porous media refracts some light.

It is possible to observe a drop impact of purified water, but the images are far from perfect. Examples can be seen in Fig. 5. Much better results are obtained by using a mixture of Toluene and Diiodomethan. With this mixture it is possible to perfectly match the refraction index. The impacting droplet is bigger than the porous slit. This results in a complete filling of the porous medium between the microscope slides. The areas filled by the liquid stop refracting the light at the glass beads. This results in a perfect transparency of this area. As shown in Fig. 2, this area is seen completely white, showing a sharp edge for the advancing liquid front. In this parametric study, the liquid, the drop size, the impact velocity, the pore size and the wettability are varied. The hydrophobic and hydrophilic characteristics are achieved with dip coatings from Company Evonik: 'Tego Top 210' and 'No drop'. The Toluene mix removes these coatings, that is why still a lot of measurements with water are used, even if the image processing is more difficult. An overview of the parameters is shown in table1. For the water the typical properties are measured: surface tension σ = 73 mN/m; viscosity μ = 0.96 mPas; contact angle(glass) Θ = 20°±5°; The Toluene- Diiodomethan mix is also measured: surface tension σ = 23 mN/m; viscosity μ = 0.66 mPas; contact angle(glass) Θ = 3°±1°;

IMAGE PROCESSING

The images obtained by the high speed camera are analyzed in the next step by a routine written in Matlab. In Fig. 5 two results of the automatic detection of the liquid front inside the porous media are shown. The penetration width and depth is measured.

RESULTS AND DISCUSSION

In Fig. 6 a typical measurement is shown. The penetration width is higher than the penetration depth in most cases. Three phases can be observed for the penetration, they are separated by the vertical lines. The first phase is simultaneous with the first spreading above the surface and shows a quick penetration. The second phase still shows penetration, but at a much lower penetration rate. In this phase the drop on the surface is performing some oscillations. The oscillations above can also excite oscillations underneath. The drop inertia of the impact movement is all transformed or dissipated already. Only the Laplace pressure [16] can be still considered as driving from above the surface.

$$\Delta \quad = \sigma \cdot \left(\frac{}{} \cdot \frac{}{} \right) \tag{2}$$

In the third phase the drop is completely penetrated into the substrate and the penetration comes to a halt. Only at these small time intervals this seems to be a real halt. On a longer time axes it can be seen that the decrease due to evaporation starts immediately. The first phase results in less penetration depth than width, but the second phase is longer for the depth, resulting in a caching up. The slope for the different phases is measured, as it is the penetration rate, or penetration velocity. In Fig. 6 the Washburn curve is shown for comparison. The first phase is often in the range of the measured values, but from the second phase on, the difference becomes only bigger. This is, of course because the Washburn curve does not account for a limited drop on the substrate. The predicted penetration is even faster than the measured. Since the impact pressure should help the penetration compared to the still drop in the Washburn case, the measured value is expected to be higher than the Washburn curve.

A big difference to most measurements is observed with the 'No drop' coating, which is highly wettable for water. One example is shown in Fig. 7. It can be clearly seen that the second phase of slow penetration is much longer and also resulting in much higher values. The initial drop radius r = 1.04 mm results in a Liquid Volume of:

$$= \frac{}{} \cdot \quad \cdot \pi = \tag{3}$$

With the penetration ½ width of 8mm at 70sec, the volume would, at complete filling, allow a depth of:

$$= \frac{\cdot}{\pi \cdot \quad \cdot \quad \cdot \phi} = \tag{4}$$

Assuming the penetrating liquid front has the shape of an ellipse with b = 8mm. The width of the porous slit is b_{slit} = 1.2mm and the porosity ϕ = 0.36. But the measured penetration depth is more than 6 mm. This implies that the measured area is not filled completely anymore.

To explain why suddenly, with a different wettability the liquid penetration changes dramatically it is necessary to take a look at the work of Seeman et. al [18]. Their main result is shown in Fig. 8. They show that for an open channel for different aspect ratios and wettabilities, completely different wetting regimes occur. The corresponding droplet shapes can be seen on the right. Of course the case F-/cW is wetting a much larger area compared to case D. What is observed in the study at hand, has to be a similar effect. Also it can be seen that the filled area is not as transparent as in the other measurements. This also shows that there is no complete filling of the pores.

ACKNOWLEDGMENT

This work is supported by the Center for Smart Interfaces, TU Darmstadt. The help of the company Evonik is acknowledged. Special thanks go to Christian Schäfer and Alexander Nees.

NOMENCLATURE

Symbol	Quantity	SI Unit
a	ellipse axis 1	[mm]
b	ellipse axis 2	[mm]
b_{slit}	width of the slit	[mm]
D_{Pore}	pore diameter	[mm]
L	penetration depth	[mm]
r	initial drop radius	[mm]
$R1$	curvature radius 1	[mm]
$R2$	curvature radius 2	[mm]
t	time	[s]
V	Volume	[mm^3]
ϕ	porosity	[ ]
μ	dynamic viscosity	[mPa s]
π	pi	[rad]
Θ	contact angle	[°]
σ	surface tension	[mN/m]

REFERENCES

[1] K. Wallace, K. Yoshida, *Journal of Colloid and Interface Science*, vol. 63-1, p.164-165, 1978.

[2] S. Chandra, C.T. Avedisian, *Int. J. of Heat and Mass Transfer*, vol.35-10, p.2377- 2388, 1992.

[3] F.A.L. Dullien, Porous Media. Fluid Transport and Pore Structure, 2nd edition, Academic Press Inc., 1992.

[4] F. Oliver, *Tappi journal*, vol.67-10, p. 90-94, 1984.

[5] W. Cooper, L. Edwards, F. Hardaway, *U.S. Army Aberdeen Providing Ground Report* No.CRDEC-TR-112, 1983.

[6] N.C. Reis, R.F. Griffiths, M.D. Mantle, L.F. Gladden, *Int. J. of Heat and Mass Transfer*, vol.46-7, p.1279-1292, 2003.

[7] K. Hapgood, J. Litster, S.R. Biggs, T.Howes, *J. of Col. and Interface Science*, vol.253-2, p.353-366, 2002.

[8] T. D'Onofrio, H. Navaz, B. Markicevic, B.A. Mantooth, and K.B. Sumpter, *Langmuir*, 26-5, p.3317, 2010.

[9] A. Clarke, T. D. Blake, K. Carruthers, and A. Woodward, *Langmuir*, 18-8, p.2980–2984, 2002.

[10] N. Allenborn, H. Rasziller, *Chemical Engineering Science*, vol.59, p. 2071-2088, 2004.

[11] N. Reis, R. Griffiths, J. Santos, *Applied Mathematical Modelling*, vol.32, p.341-361, 2008.

[12] P. Alam, M. Toivakka, K. Backfolk, P. Sirviö, *Chemical Engineering Science*, 62, p.3142 – 3158, 2007.

[13] C. Batz-Sohn, A. Lembach, L. Nelli, A. Müller, I. Roisman, C. Tropea, *NIP26 26th International Conference on Digital Printing Technologies and Digital Fabrication*, Austin Texas USA, sept. 2010.

[14] Edward W. Washburn, *Physical Review*, 17-3, p.273, 1921.

[15] A. Gipperich, A. N. Lembach, I. V. Roisman and C. Tropea, *23rd International Conference on Liquid Atomization and Spray Systems*, Brno, Czech Republic, September 2010.

[16] P.S. Laplace, Mécanique céleste, Supplement to the tenth edition, 1806.

[17] A.N. Lembach, C. M. Weickgenannt, S. Goertz, I.V. Roisman and C. Tropea, *Atomsation and Sprays* (submitted 2011)

[18] R. Seemann, M. Brinkmann, E. J. Kramer, F. F. Lange, and R. Lipowsky, *Proc. Nat. Acad. Sci.*, vol.102, p.1848, 2005.

Table 1. Parameter variation

Pore sizes	small: 36µm		mid: 90 µm		big: 202 µm	
Fluids	distilled Water			Toluene- Diiodomethan		
Drop Size (water)	2.71mm		2.11mm		2.08mm	
Drop Size (toluene..)	2.01mm		1.65mm		1.55mm	
Release height	~0cm	1cm	5cm	20cm	50cm	1m
Wettability (water)	(0°) No drop		(165°) Tego Top 210		(20°) plain glass	

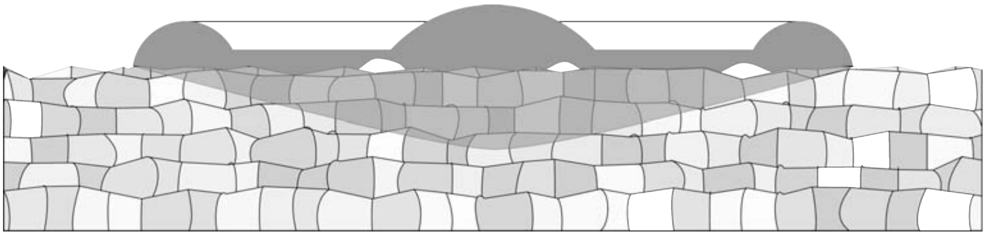

Figure 1. Sketch of drop impact on porous media

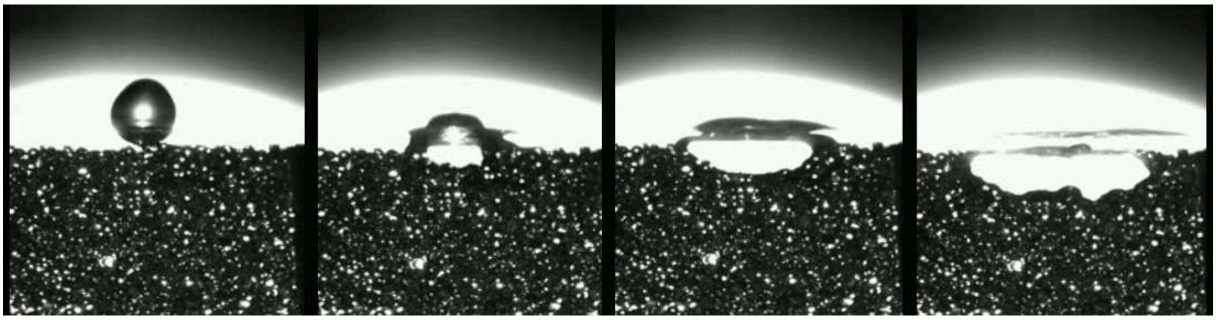

Figure 2. Typical result of a millimeter size drop impacting on a porous substrate (0.01sec total)

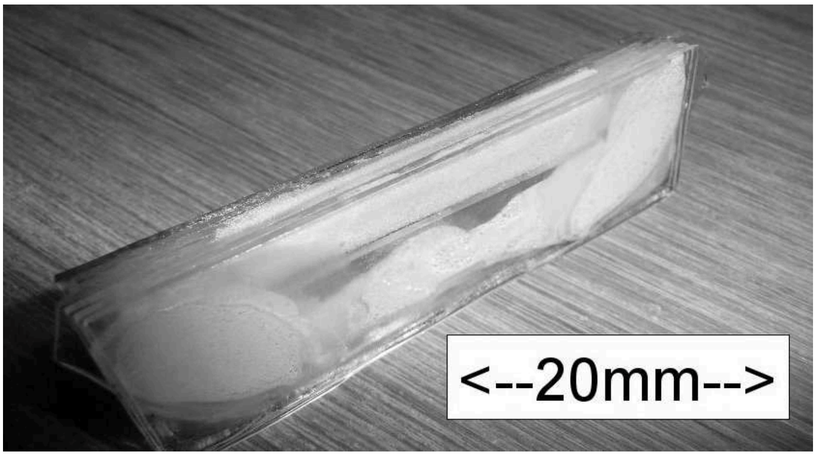

Figure 3. A porous target – glass beads sintered in slit

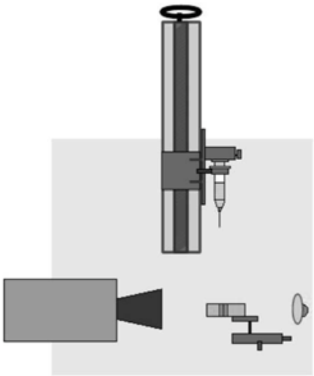

Figure 4. Experimental Setup

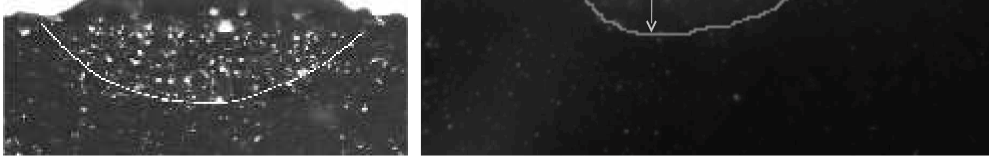

Figure 5. Two results of automatic detection of liquid front in porous medium for water

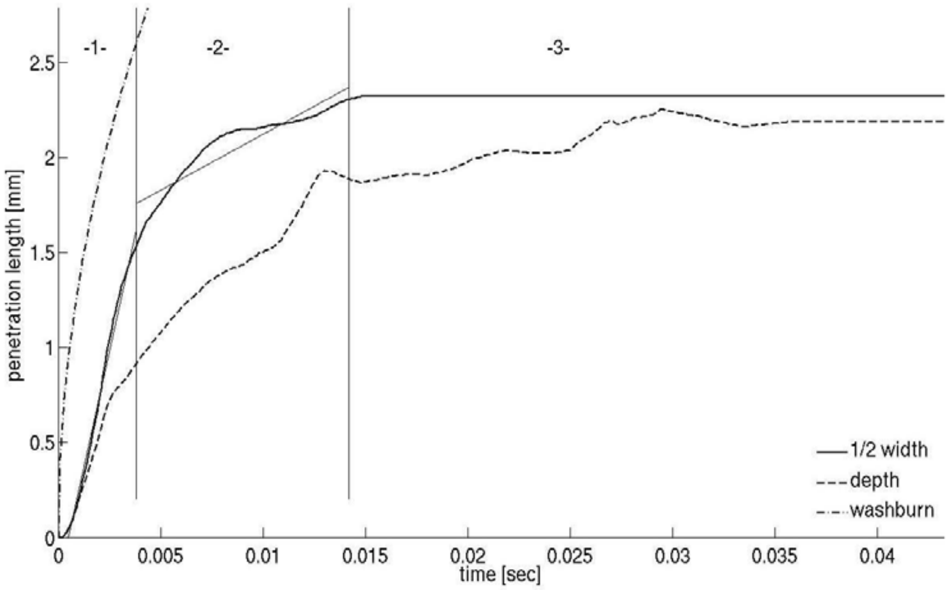

Figure 6. Penetration depth and ½ width over time compared with Washburn
(Toluene-mix; 2.01mm drop diameter; 0.5m/s impact velocity; 202μm pore size)

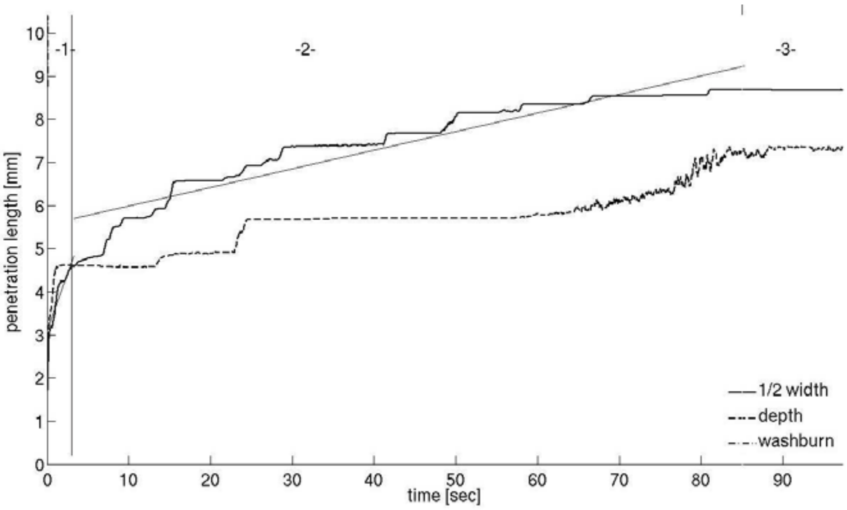

Figure 7. Penetration depth and ½ width over time compared with Washburn
(Water; 2.08mm drop diameter; 0m/s impact velocity; 202μm pore size, 3° contact angle)

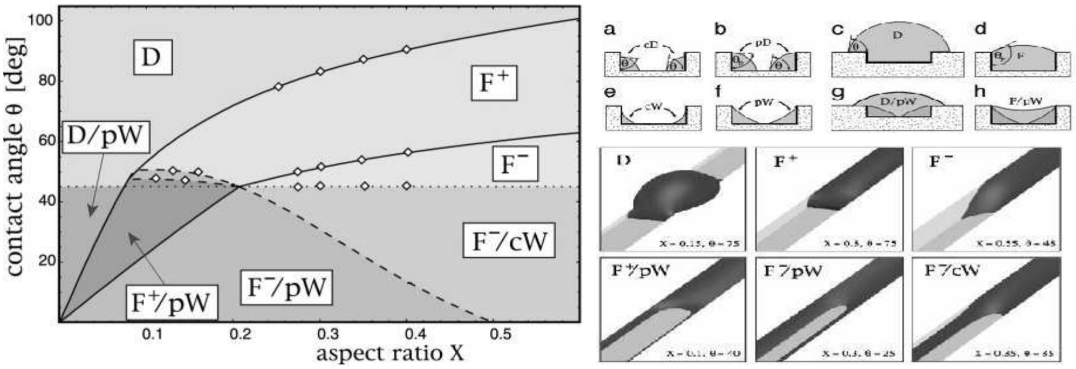

Figure 8. Wettability and channel aspect ratio affect the wetting regimes as shown on the right [18]

DIPSI Workshop 2011 on Droplet Impact Phenomena & Spray Investigation
May 27, 2011, Bergamo, Italy

CAVITATION INSIDE ENLARGED AND REAL-SIZE FULLY TRANSPARENT INJECTOR NOZZLES AND ITS EFFECT ON NEAR NOZZLE SPRAY FORMATION

N. Mitroglou, M. Gavaises*, J.M. Nouri and C. Arcoumanis

Energy and Transport Research Centre
School of Engineering and Mathematical Sciences, City University London, UK
*corresponding author email: m.gavaises@city.ac.uk

ABSTRACT

The effect of string cavitation in various transparent Diesel injector nozzles on near nozzle spray dispersion angle is examined. Additional PDA measurements on spray characteristics produced from real-size transparent nozzle tips are presented. High-speed imaging has provided qualitative information on the existence of geometric and string cavitation, simultaneously with the temporal variation of the spray angle. Additional use of commercial and in-house developed CFD models has provided complimentary information on the local flow field. Results show that there is strong connection between string cavitation structures and spray instabilities. Moreover, elimination of string cavitation results in a stable spray shape that is only controlled by the extent of geometric-induced cavitation pockets. Finally, PDA measurements on real-size transparent nozzle tips have confirmed that such nozzles reproduce successfully the sprays generated by production metal nozzles.

INTRODUCTION

The role of the fuel injection system in modern direct-injection Diesel engines is paramount and well recognised as a means of controlling their performance and meeting the ever more stringent emission regulations. Electronic common-rail injection systems employ a variety of nozzle designs and engine optimisation injection strategies to cover a wide range of operating conditions that modern Diesel engines are expected to perform. Increasing injection pressure, piezo-controlled mechanisms for achieving fast response of the needle valve and multiple injections are among the methods explored and known to improve combustion and engine performance. However, under such operating conditions, cavitation phenomena are present inside the nozzle and become the dominant and frequently uncontrolled flow characteristics that affect fuel system durability and the properties of the near-nozzle emerging spray. Success of modern Diesel direct-injection fuel equipment is based on their ability to control accurately timing, duration, rate and number of injections, as well as, shaping of the spray pattern to match piston-bowl geometry and enhanced cyclic variability behaviour employing a number of different nozzle designs. Investigations over the years have demonstrated that Diesel injector nozzles generate cavitation [1-3] under typical operating conditions, a fact that complicates further the already complex design of high-pressure Diesel injection systems. As demonstrated in [4-6], two distinct forms of cavitation have been identified inside injection nozzles, geometrically-induced and vortex or string cavitation. Geometric-induced cavitation is the most common form of cavitation and it has become gradually a well-understood phenomenon; it initiates at sharp hole inlet corners due to the abrupt acceleration of the fuel flow as it enters the nozzle holes. This increase of velocity creates a pressure drop which induces cavitation at the core of the recirculation zone formed at the hole inlet; this is more pronounced with sharper rather than rounded inlet hole geometries achieved through hydro-grinding. On the other hand, string or vortex cavitation structures have been observed in the bulk of the liquid inside sac, mini-sac and valve covering orifice (VCO) nozzles, where the formed internal volume allows for formation of relatively large-scale vortical structures [7-9]. Vortex cavitation is commonly found in propellers, hydraulic turbines and hydrofoils as explained in [10-13] However, recent studies have confirmed similar behaviour in multi-hole nozzles for high-pressure direct-injection gasoline engines and low-speed two-stroke Diesel engines [7, 14-17].

Cavitation is linked to undesirable effects such as sharp reduction in engine performance, increase in noise and vibrations, as well as surface erosion [15]. In most cases of practical interest, cavitation bubbles survive until the nozzle hole exit [4]. Therefore, it is generally accepted that cavitation promotes fuel atomisation, which is desirable for enhanced air fuel mixing. However, some studies [18] have indicated that cavitation may also be associated with hole-to-hole and cycle-to-cycle variations. Appropriate design of the inlet hole curvature and the non-cylindrical shape of the holes as [19, 20] showed, alter cavitation inception and development characteristics; at the same time, careful system optimisation is found to achieve reduction of engine exhaust emissions while maintaining similar performance standards [7, 15]. Until recently, different cavitation regimes have been addressed independently. However, there is evidence [5] that geometric-induced and vortex cavitation possibly interact in various ways. Additionally, recent investigations have concluded that inception of string cavitation is dramatically enhanced and owes its existence to sources of vapour already present inside the nozzle volume [8]. These latest findings indicate that interaction of co-existing different cavitation structures possibly require further investigation, particularly at low and intermediate needle valve lifts where, needle-seat cavitation may also exist.

Experimental investigations for obtaining real-time in-nozzle flow measurements in production FIE systems, during an injection event, are rendered difficult and, in most cases, impossible to be conducted. Therefore, majority of the reported experimental studies involve configurations simulating Diesel engine operating conditions. A number of investigations have examined the development of cavitation in transparent large-scale nozzle replicas, as presented in [21-24]. A limited number of studies have also demonstrated dynamic flow similarity based on, simultaneous, matching of Reynolds and cavitation numbers. The latter allows for comparison between the two-phase flow regimes formed inside real-size and enlarged nozzles of identical scaled-up geometric characteristics [3, 25]. Simulations reported for real-size and scaled-up models using a variety of cavitation models [26] have confirmed that similar flow regimes are formed despite obvious differences in the micro-scale level of bubble formation and development The latter is effectively the effect of a large number of cavitation bubbles that coalesce and form the macroscopically observed cavitation cloud.

Following the well-established large-scale, steady-state nozzle flow studies, significant effort has been made towards manufacturing of real-size transparent nozzles. The motivation and driving force behind these efforts is summarised in the need to confirm the existence of the afore-mentioned cavitation structures and to gain insight of the highly transient flow developing during an injection event. Until recently, the majority of manufactured real-size nozzles have been simplified single-hole geometries that generally confirm the presence of geometric-induced cavitation [2, 27]. The research group at City University London were the first to substitute one of the holes of a production nozzle with a quartz window of identical geometric characteristics; an experimental breakthrough that provided valuable information on flow and cavitation structures inside a real-size multi-hole injector under realistic operating conditions [3, 28, 29]. A step forward is realised in [19], where a 3-hole, real-size, fully transparent Diesel nozzle is presented and optical access inside the sac volume is also granted.

The advances in internal nozzle flow studies under fully transient and realistic operating conditions have provided valuable information and validation data for CFD cavitation models capable of predicting the various forms of cavitation; for example see [30-32]. Experimental validation of numerical CFD models is rendered essential and supplementary to understanding the flow processes in complicated nozzle geometries and ultimately, to the design of new nozzle designs. However, the difficulty associated to manufacturing of real-size, transparent nozzles that are exact replicas of real nozzle geometries impose simplifications to the design of the nozzle itself and the transient operation of the needle. Moreover, complications related to the physical properties and the quality of the working fluids imposes additional difficulties. Furthermore, the scarce data available in real-size transparent nozzles are limited to pressures an order of magnitude lower than those currently used in modern Diesel engines. Increase of the injection pressure beyond 2000bar in the forthcoming future [33] is expected to affect fuel properties and thus, cavitation, as recently reported in [34]. More importantly, highly transient flow dynamics caused by fast needle response times give rise to the formation of vortical structures and therefore, to string cavitation [8]. Transient effects have also been correlated to increased probability of surface erosion damage [35], which is attributed to both, hole and string cavitation. Nevertheless, combination of experimental data obtained in both, large-scale and real-size injector nozzles are considered valuable for the development and validation of cavitation models applicable for fuel injectors.

The present paper represents a continuation of the work presented recently in [8, 17, 36]. Main investigations focus on the effect of string cavitation in various Diesel injectors on near nozzle spray dispersion angle both, in large-scale and real-size transparent nozzle tips. Near nozzle spray vicinity is defined at a distance of about one injection hole length downstream the nozzle exit plane. Acquired data and thorough investigations are based on a number of fully transparent nozzle replicas, as well as, real-size nozzle tips that provide unobstructed optical access of the nozzle sac volume, injection holes and sprays formed at the nozzle exit. Image collection over sufficient duration periods, for steady-state experiments and adequate imagining frame rates, for transient operating conditions, have provided qualitative information on the existence of geometric and string cavitation, simultaneously with the temporal variation of the spray angle. Investigated designs include 6-hole nozzle configurations of valve-covering orifice (VCO), mini-sac, as well as a new prototype nozzle design that promises to eliminate string cavitation and produce steady spray shapes. Simultaneous use of two synchronised high-speed cameras allowed for visualisation of all forms of cavitation inside the nozzle volume, as a function of needle lift and operating condition. At the same time, use of commercial and in-house developed CFD models has provided complimentary information on the local flow field of the tested nozzles. Finally, assessment of real-size transparent nozzle tips is achieved in terms of emerging spray characterisation through the use of PDA measurements. The latter aims to demonstrate that such real-size transparent nozzle tips reproduce adequately the internal flow and spray characteristics of real-size metal nozzles. Then the various results obtained are presented while the most important findings are summarised at the end.

EXPERIMENTAL SET-UP

Presented results in following sections have been obtained in both, enlarged and real-size transparent nozzle models. Figure 1 illustrates the two basic nozzles where studies are based on. An additional nozzle design is used for the large-scale experimental and computational cases.

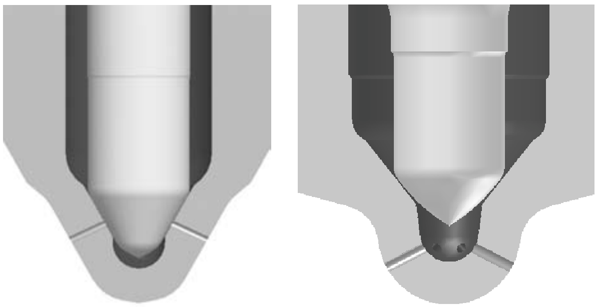

Figure 1: Investigated nozzle geometries. (a) valve-covering orifice (VCO) and (b) sac type nozzles with a 6-hole configuration.

The main characteristics of its configuration include elimination of sac volume and independent flow path for all six injection holes; as a result, flow interconnection among the holes is eliminated. All transparent nozzles (large-scale and real-size) were manufactured from a clear, acrylic material. The scaling factor of the enlarged models was chosen to be ten (x10) times the real-size nozzle. All nozzles share injection holes of cylindrical shape. All designs feature sharp hole entries, and their diameters vary from 136×10^{-6} m to 300×10^{-6} m in real-size dimensions. The large variation in injection holes diameters among all nozzles is attributed to their field of operation; low diameter values represent nozzles that operate in engines fitted on passenger vehicles, while large injection hole diameters refer to injectors for large power production units installed on land or on marine applications. In the following sections the experimental set-up for both large-scale and real-size investigations is presented.

Enlarged Model Test-Rig

A schematic overview of the experimental setup with the incorporated large-scale model is shown in Figure 2. Two different variations of this rig have been utilised; the first one is a closed-loop flow circuit and injection takes places in to liquid. Dynamic flow similarity to realistic operating conditions is achieved based on Reynolds and cavitation numbers. Such flow similarity assists in interpretation of cavitation flow regimes formed inside the transparent nozzle relative to a real-size case. The second variation incorporates injection against atmospheric quiescent environment exhibiting open-loop circuit (variation presented in Figure 2).

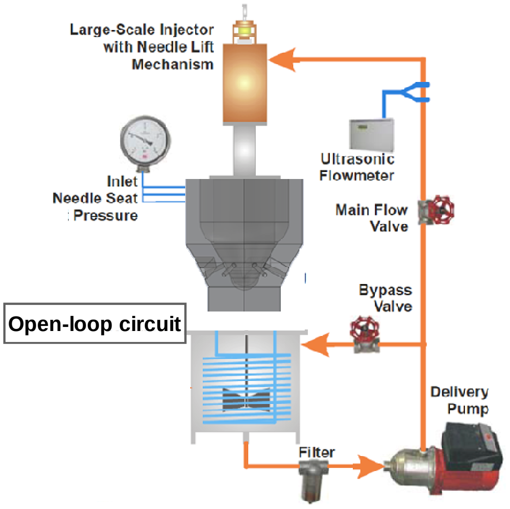

Figure 2: Schematic of the enlarged model test-rig. The open-air injection variation is presented.

The latter has proven to be a promising solution to simultaneous visualisation of in-hole cavitation structures and emerging spray shape. The present system is not expected to represent exact flow fields encountered in a real injection event. Firstly, it is a steady-state experiment, thus it does not account for transient needle movement. Moreover, realistic flow conditions cannot be matched, therefore, dynamic flow similarity to real-size flow fields assists in gaining physical understanding of the specific nozzle flow characteristics and validation of simulation results. Additionally, acquired information is rendered useful, as it is explained in following sections, since it allows for internal nozzle flow structures to be linked to the near nozzle spray stability.

The flow rate through the nozzle is controlled by a valve fitted downstream the liquid delivery pump and measured by an ultrasonic flow meter. In the case of injection in to liquid (closed-loop variation of the rig), simulation of sub-atmospheric chamber pressure conditions and therefore, high cavitation numbers, is achieved by a suction pump. The latter is installed on the drain side of the circuit. Reynolds number is defined on the basis of mean flow rate through the nozzle and average hole diameter, while the definition of cavitation number is as follows in Eq. (1):

$$CN = \frac{\left(P_{inj} - P_{back}\right)}{\left(P_{back} - P_{vapour}\right)} \qquad (1)$$

The working fluid is water and its temperature is kept constant at 25°C.

Flow through a multi-hole nozzle, and especially through the injection holes, is known to be highly turbulent. Although the experiment was run under steady-state conditions, all flow features and, in particular, cavitation structures, are expected to behave transiently and to exhibit short time scales. This dynamic behaviour is captured by an advanced high-speed digital imaging technique at frame rates varying from 20k – 50k frames per second.

Real-Size Transparent Tip Test-Rig

Investigations of internal flow and cavitation formation inside a real-size nozzle operating under highly transient realistic conditions are achieved by replacement of the nozzle tip with an exact replica transparent cap. The technique has been developed and presented thoroughly in [36, 37]. A brief description of the required modifications is illustrated in Figure 3. Finally, the clamping mechanism of the transparent tip on to the metallic nozzle body is shown in Figure 4.

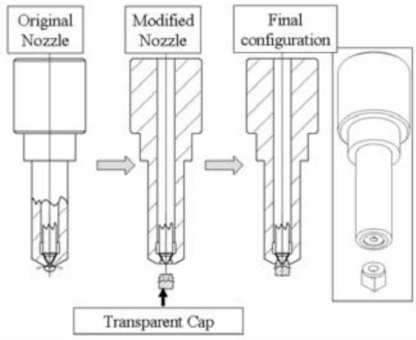

Figure 3: Nozzle modifications and transparent tip assembly [36].

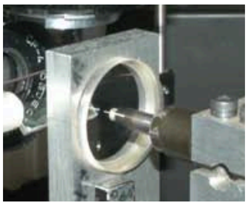

Figure 4: Clamping mechanism of transparent nozzle tip.

The experimental set-up used to capture the effect of cavitation on the emerging fuel spray involved a dual, high-speed imaging technique. First, high-speed imaging provided information on the onset and development of cavitation inside the injection hole, while, at the same time, the emerging fuel spray was captured on a second high-speed camera that was focused on the first 2mm downstream of the exit of the injection hole. As illustrated in the set-up schematic in Figure 5, the real-size dimensions of the nozzle did not allow for the two cameras to lie on the same horizontal plane, thus necessitating a complex setup utilising a 50-50 wideband beam splitter that allowed one camera to access the in-hole flow through the beam splitter and the second to utilise the built-in mirror feature of the splitter on the vertical plane. The selected light source for best possible illumination was a high-power (~20W) pulsed laser. An advantage of the selected illumination source was the pulse width of the laser used, as it determines the image exposure duration, and it was of the order of 150-180 ns; an exposure duration that cannot be matched by any high-speed camera available. The drawback in that system has been its inability to perform at pulse frequencies greater than 6 KHz. The latter has limited the maximum possible imaging frame rate to 6000 frames per second.

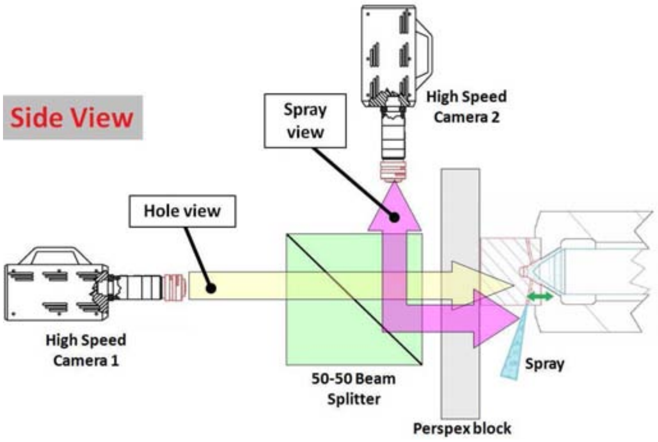

Figure 5: Dual imaging set-up schematic.

Detailed phase–Doppler anemometry (PDA) measurements completed the real-size, transparent nozzle tip experiments. The PDA system setup chosen for this investigation is illustrated in Figure 6. The system is a 2-dimensional PDA system where the vertical (u) and horizontal (v) velocity components are measured simultaneously for each droplet. PDA is a point measurement technique and selection of the measurement plane and grid are essential. It is well accepted that the closer the measured points to the nozzle exit are, the better the understanding of the nozzle performance; however, given the high injection pressures of Diesel nozzles (above 300bar is considered to be a high injection pressure for this type of measurement), fuel jets tend to have a significantly dense liquid core as soon as they exit the nozzle which renders impossible any attempts to measure within that region. This is mainly due to attenuation of the laser beam when it penetrates high-pressure dense sprays with a pronounced liquid core. The compromise that is often made is to move the measurement plane further away from the nozzle exit. In the present experiment, the measurements plane was set at 10 mm away from the nozzle exit, where higher data rates were achieved and a smaller number of injections was needed, as transparent nozzle tips are replaced after approximately 100 injection events. The latter is a necessity due to certain wear that appears in the acrylic tips caused by high-pressure fuel flow.

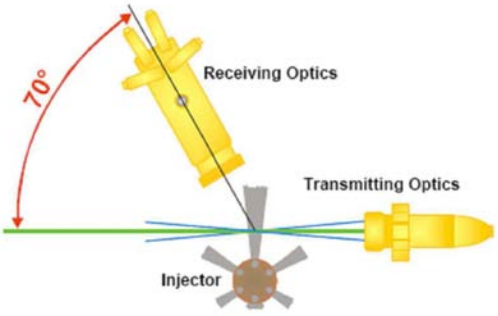

Figure 6: Optical configuration of the phase – Doppler anemometer (PDA) system.

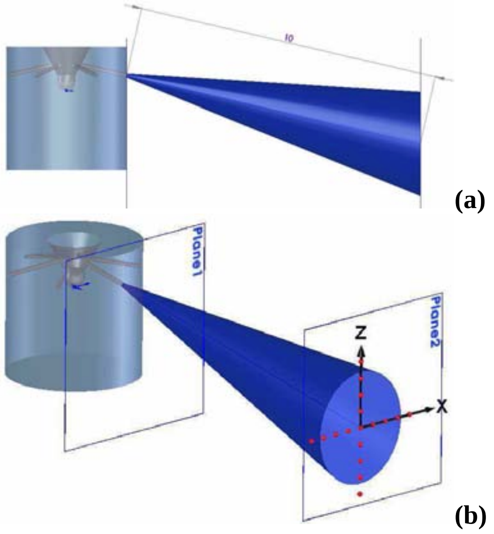

Figure 7: Schematic representation of the PDA measurements grid; (a) axial plane distance from nozzle exit and (b) grid points definition.

Figure 7 schematically illustrates the location, in space, of the measurement plane and grid relative to the injection hole exit. Points, where data were acquired, lie on two normal axes as shown by red dots in Figure 7(b). The spatial resolution of the above grid is 0.5mm.

RESULTS AND DISCUSSION

In this section the various results will be presented and discussed. Initially, the results obtained from the combined investigation of internal nozzle flow and emerging spray of a valve-covering orifice (VCO) nozzle are presented. Those include images of in-hole cavitation structures, focused particularly on string cavitation, as well as the emerging spray shape for several operating conditions including various needle lifts, Reynolds and cavitation numbers. Following the VCO large-scale study, results from a prototype nozzle design are presented. This design promises to eliminate string cavitation inside the injection holes, thus, it exhibits stable sprays under all tested operating conditions. Internal nozzle flow results accompanied by spray images are presented. Finally, spray characterisation results from a real-size transparent tip VCO nozzle are presented. These results include particle velocity and size measurements conducted at sprays produced by a transparent tip converted VCO nozzle.

Large-Scale VCO Nozzle Study

The study of the VCO nozzle geometry includes various operating conditions: low and full needle lift cases, low and high cavitation numbers, as well as a variety of flow rates through the nozzle are included. The manufactured large-scale VCO nozzle replica is ten times (×10) larger than the real-size nozzle and it features sharp hole inlet. The latter is important since a fair amount of geometric-induced cavitation is present inside the injection hole; consequently, nozzle discharge coefficient varies from 0.26, at lowest needle lift, to 0.47 at maximum needle lift. Additionally, cavitation and Reynolds numbers of all tested conditions vary from 3 to 6.5 and 12 000 to 27 500, respectively.

The first observation is done at 20×10^{-6} m needle lift, cavitation number of 3 and low Reynolds number, of the order of 12 000. At such low flow rate conditions geometric – induced cavitation is minimum inside the hole (Figure 8); therefore, emerging spray is not atomised. Moreover, it is clearly seen on the sequence of images presented in Figure 8 that string cavitation has been observed. Its presence is not continuous, it is rather switching on and off during the tests. Additionally, it is found to have a profound effect on the spray cone angle. The mechanism of string formation under these low flow rate conditions has confirmed and is in full agreement with observations presented in [17]. According to what has been recorded, vapour visualised as a ‘string’ is not actually ‘cavitation’ but air entering into the nozzle from the hole exit. Swirling flow patterns inside the injection hole possibly cause sufficient pressure drop allowing for air from outside the nozzle to enter the injection hole and travel upstream towards the sac volume. Once this stream of air reaches the hole inlet, it interacts instantly with geometric-induced cavitation at that location. Therefore, cavitation pockets are generated at the hole inlet due to strong interaction with the stream of air/bubbles. Following induction of geometric-induced cavitation, the flow field inside the injection hole is altered, thus, influencing spray stability. The resulting effect on spray angle has been quantified and the recorded data of string cavitation inside the nozzle hole and spray cone angle show a change of approximately 30°. Precisely, when no string is present, spray cone angle varies from 18°-20°; however, when string cavitation is observed inside the hole, spray cone angle is measured to be of the order of 50°.

Increasing Reynolds and cavitation numbers to 18000 and 6.3, respectively, flow field inside the injection hole changes marginally, at low needle lifts. Main difference is found to be on the size of the geometric – induced cavitation regime. The latter is now larger and occupies more of the cross-sectional area of the hole, as opposed to lower CN conditions, and also extends further inside the hole. As presented previously in [17, 38] the interaction between intense geometric-induced cavitation structures and string cavitation is responsible for the differentiation in spray angles of upper and lower spray boundary. In detail, when the geometric locus of the cavitation strings coincides with the area occupied by geometric-induced cavitation pockets, then the effect of the string on the spray shape is marginal. On the contrary, when string cavitation lies on the part of the hole that is not occupied by geometric cavitation then the effect on the spray shape is well pronounced; the latter is illustrated in Figure 9 by comparison of spray images against predictions of vapour in VCO nozzles.

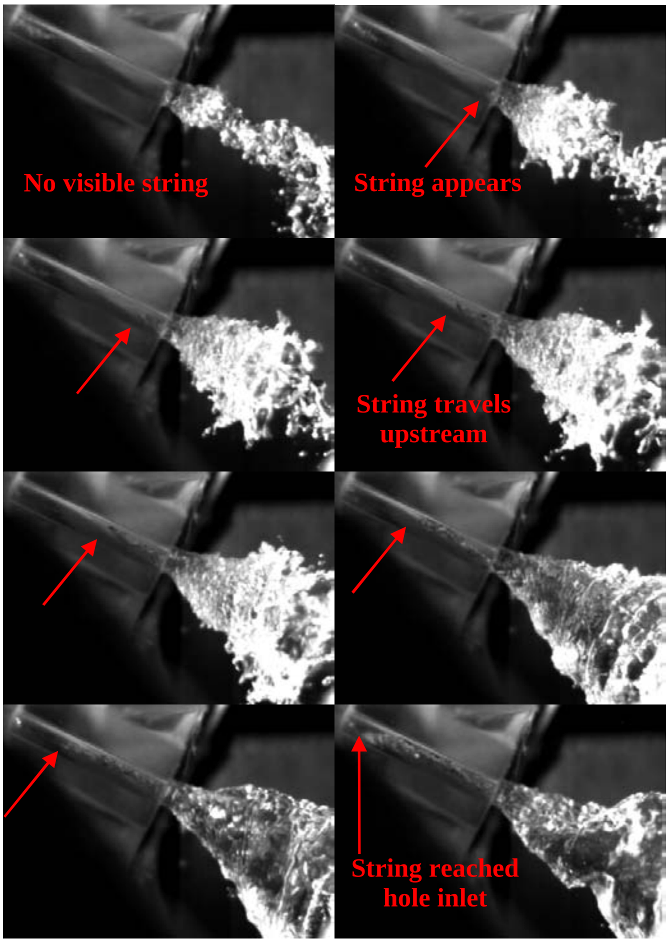

Figure 8: Developmnt of string cavitation and spray shape at 20µm needle lift, CN=3 and Re=12 000.

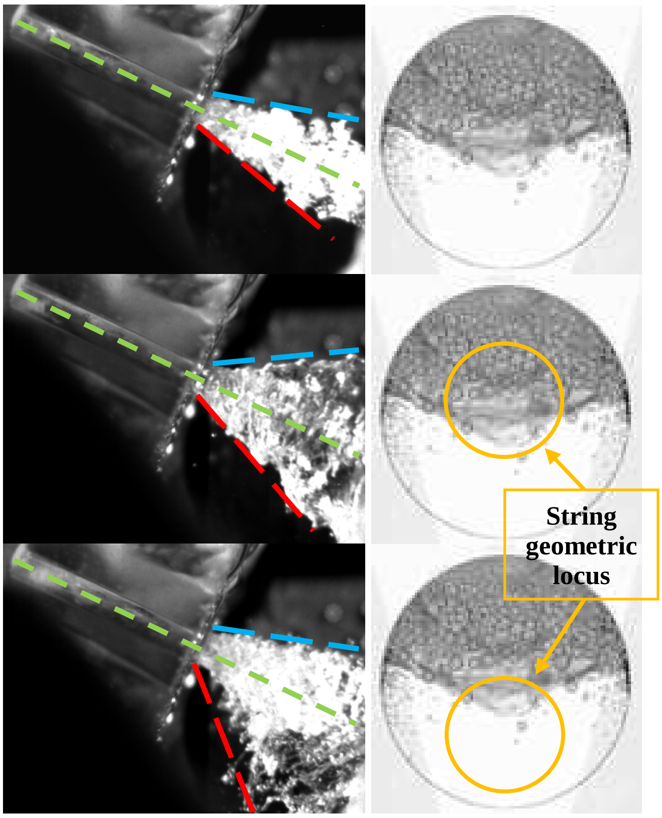

(a) (b)

Figure 9: (a) Spray shape variation images and (b) vapour distribution prediction [38]

Similar behaviour has been observed at high valve lift cases. Precisely, at full needle lift that is set to 250×10^{-6} m, geometric-induced cavitation is very intense and reaches the exit of the injection hole. Therefore, string cavitation seems to affect mainly the lower boundary of the spray as illustrated in Figure 10. Quantitatively the effect on the lower spray boundary presented in Figure 10 is reduced to 50%, as compared to the low needle lift cases (see Figure 9). The reason for this reduction lies on the fact that at high needle lift cases, the upper part of the hole is solidly occupied by geometric cavitation structures that, at high flow rates, extend to the hole exit thus, increasing atomisation. Additionally, at such high flow velocities (calculated to be larger than 15 m/s for the large-scale model), string cavitation structures rarely initiate at the hole exit and travel upstream inside the injection hole. Instead, strings are created at the core of recirculation zones forming inside the nozzle's sac volume [8]. In the case of VCO nozzles, where the sac volume is absent, a minor volume that forms between the needle face and hole inlet promotes swirling motion at the hole entry, due to injection holes flow field interactions. Therefore, this swirling motion gives rise to string structures and due to their origin location, their core consists of tiny cavitation bubbles that most probably are fed into the stream from the intense geometric cavitation structures at the hole entry and enhance its existence. Recent work by the authors in fully transparent real-size nozzles operating at pressures up to 600bar has verified that such structures can be present during real injection events.

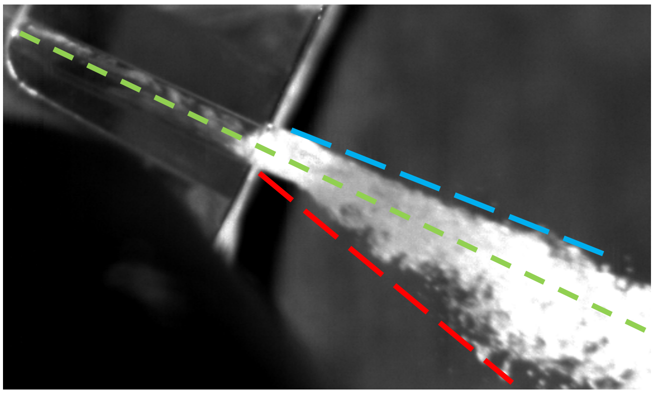

Figure 10: Observed variation in upper (blue) and lower (red) spray half angle at full needle lift and cavitation number of 6.3.

Large-Scale Prototype Nozzle Design

The authors' research group has conceived and tested a new nozzle design that eliminates the aforementioned vortex flow at the hole entry by isolating each hole's flow path. Elimination of vortex flow has been proved to affect considerably, and ultimately eliminate, vortex cavitation structures. As presented in the following Figure 11, geometric cavitation structures formed at the hole inlet are "controlled"; the latter effectively means that cavitation always takes place at the same location. The penetration of the formed vapour pocket inside the nozzle hole and resulting volume fraction are carefully 'designed' with the aid of CFD by modifying basic nozzle design characteristics. The presented nozzle design exhibits no hole inlet rounding thus, cavitation structures are intense. It is illustrated in Figure 11(a, b and c) that at various needle lifts, under constant cavitation number, formed vapour clouds extend to certain length, for each case, inside the injection hole and remain at the same location without exhibiting any transient movement in terms of their length. The swirling motion reported by various researchers [5, 29, 36] inside the injection hole is absent. Therefore, string cavitation is eliminated and emerging sprays exhibit stable shape patterns, as illustrated in Figure 12. As mentioned above, by altering certain design characteristics of this new concept nozzle design cavitation is well controlled and, consequently, different spray dispersion angles are achieved (Figure 12) and exhibited spray stability is paramount under all operating conditions. Moreover, levels of spray atomisation are well controlled by the extend of geometric cavitation structures inside the injection hole.

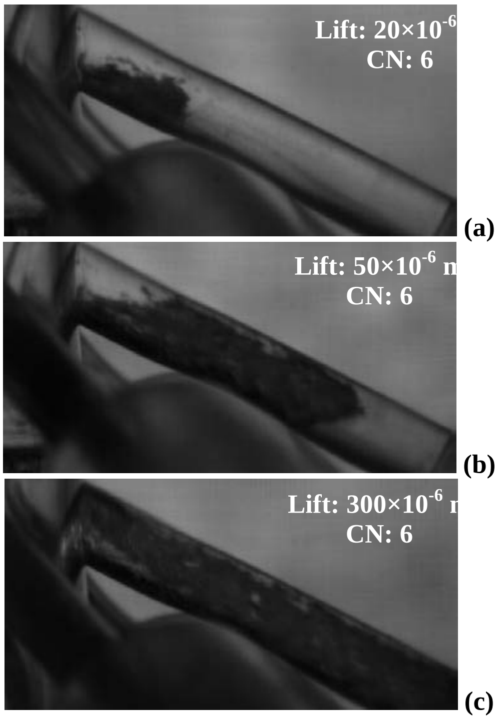

Figure 11: Cavitation imaging inside the injection hole of a new concept design nozzle at CN = 6 and (a) low needle lift of 20μm, (b) needle lift of 50μm and (c) full lift of 300μm.

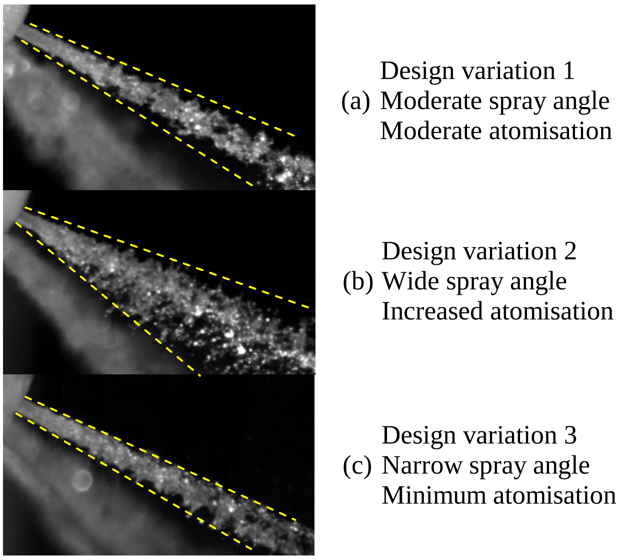

Figure 12: Spray images at steady state conditions from a new concept nozzle design for two different needle designs (a), (b) and (c).

Real-Size Transparent Nozzle Tip

Following the extensive investigations of internal flow and its effects on emerging spray shape stability in enlarged, transparent nozzle replicas, the need to confirm the existence of the observed structures in real-size nozzles has become a necessity. A selected, generic VCO nozzle has been converted to accommodate a transparent nozzle tip that allows for direct optical access inside the nozzle and injection holes. Simultaneous acquisition of images of the emerging spray enabled the establishment of the link between internal nozzle flow and emerging spray stability in real-size nozzles. However, due to the complexity of the real-size nozzle tip experiment, certain alterations to operating conditions had to be made; injection pressure is set to 30 MPa to prevent leakage and fast deterioration of the transparent nozzle cap and therefore, injection duration is set to 4ms to match the corresponding flow rates.

Detailed investigations on string cavitation have provided enough supporting evidence that structures observed in large-scale replicas also exist in real-size nozzles. Figure 13 illustrates sample acquired images and nozzle characteristics that are visible from this view angle. As illustrated below, the needle surface, the minor formed sac volume and side views of the injection holes are clearly visible. On the right-hand image of Figure 13, cavitation bubbles that started forming inside the injection hole are shown. Additionally, evidence of needle string cavitation is visible; needle string cavitation is effectively a string cavitation originates at the hole entrance, due to strong swirling flow, and extends on to the needle face.

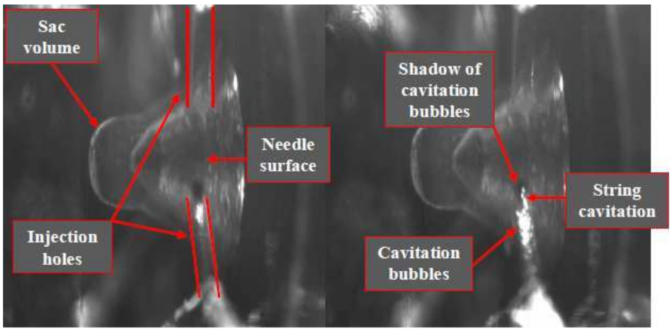

Figure 13: Sample side view images of VCO nozzle and explanation of illustrated features.

Figure 14 presents a series of images from 1.9ms – 2.5ms after triggering of injection from a 4ms injection event at 40 MPa injection pressure. It is noticed that from 2ms after triggering of injection and onwards, string cavitation appears at the hole entrance and it moves towards both directions, the needle surface and inside the hole. The latter contributes to acceleration in formation of geometric cavitation structures inside the hole. These string structures remain attached to the needle until its lift increases enough to no longer be in front of the injection holes entrance. Similar behaviour of string cavitation structures inside high-pressure injection nozzles has been verified through earlier work of the authors' research group. As injection develops, a strong swirling flow is present inside the injection hole and around its entrance. The latter enhances the formation of strings of bubbles and confirmed the previously presented behaviour of string cavitation and its formation mechanisms in the large-scale nozzle replicas.

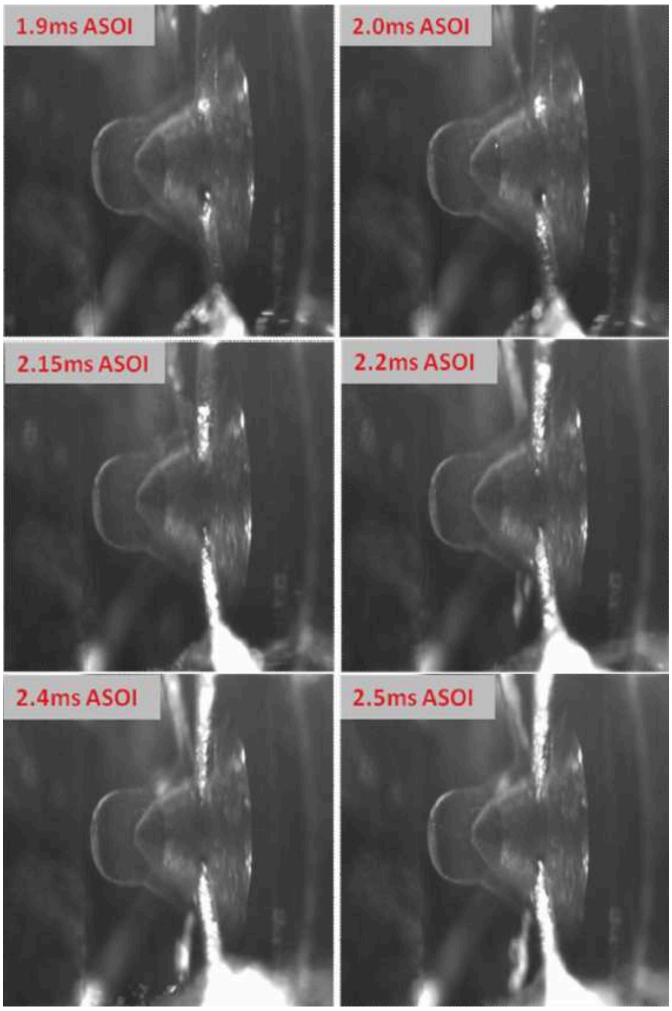

Figure 14: Time sequence of images at 300bar injection pressure and injection duration of 4ms.

Further investigations in real-size nozzles are focused to establishment of possible links between in-hole cavitation formation and development and the emerging spray structure and stability. The following dual imaging investigation includes bottom view, high-speed images of the internal hole flow and first stages of the emerging spray.

Acquired images for the standard VCO nozzle design at 40 MPa showed that at early injection stages, when cavitation has not built up inside the hole, this is immediately reflected on the emerging spray shape. Figure 15 illustrates a sequence of images for the aforementioned conditions and it can be argued that atomisation quality of the spray (right-hand side images) improves as cavitation builds up inside the hole (left-hand side images). Additionally, an extra feature that is clear from these images is that Start of Injection (SOI) happens at around 1ms after electronic triggering of the injector, which implies that the first liquid to exit the injection hole is visible at 1ms after triggering, as shown in the images below. At higher injection pressures of 40 MPa, as illustrated in Figure 16, cavitation develops faster than the lower pressure case inside the injection hole. This ensures that spray atomisation is less affected by any marginal changes of cavitation structures inside the hole. However, in Figure 16 a substantial change in spray cone angle is evident at 1.34ms after trigger. The optical set-up and lighting source used does not allow for clear interpretation of cavitation strings inside the hole, although geometric cavitation pattern does not seem to be affected from one step to the next.

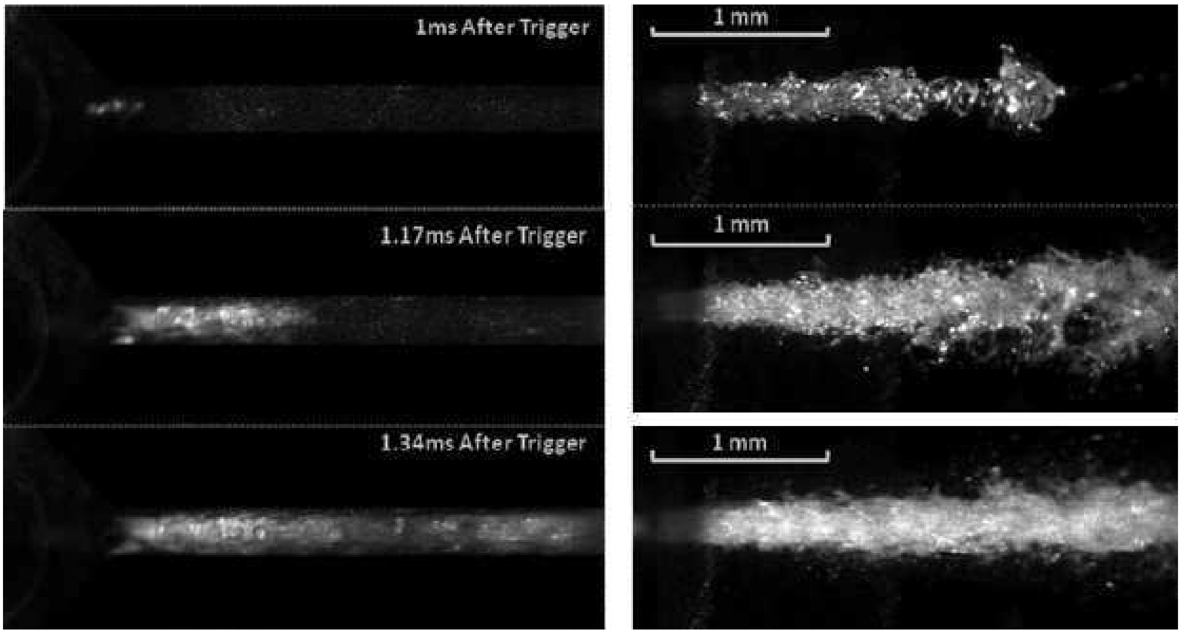

In-hole flow **Emerging spray**

Figure 15: Sequence of images at early stages of injection for the VCO nozzle design at 300bar injection pressure.

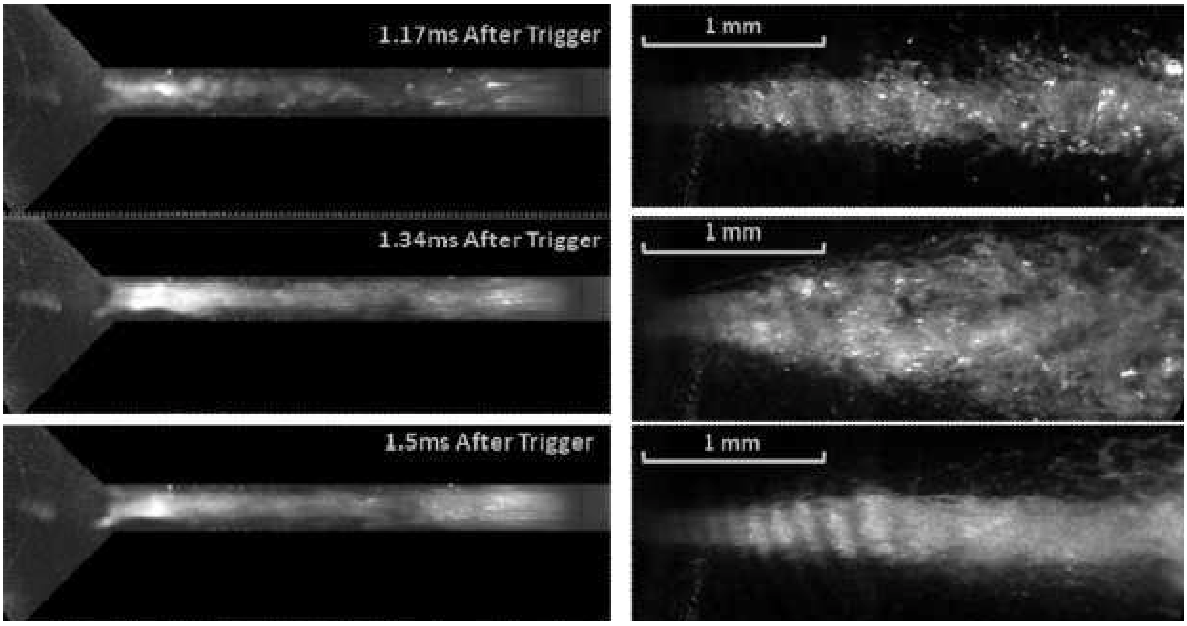

In-hole flow **Emerging spray**

Figure 16: Sequence of images from injection event at 400bar.

Finally, assessment of real-size transparent nozzle tips and complete characterisation of the spray is achieved through the use of PDA measurements. The latter aims to demonstrate that such real-size transparent nozzle tips reproduce adequately the internal flow and spray characteristics of real-size metal nozzles; additionally, it provides an extra means of quantitative measurements of spray velocities and sizes that is considered mandatory for a compete characterisation of the performance of an injector.

PDA results have been acquired for the VCO nozzle geometry, and are presented as temporal and spatial profiles. The former show the variation of the resultant velocity vector (absolute velocity and angle values are plotted) at one point for the entire injection duration. The latter show the spatial variation of the resultant velocity vectors at a certain time for more than one point at a cross section of the jet. Furthermore, droplet diameter profiles are presented in the same way. The main axis of the PDA measurement points is the vertical axis z, as shown in the top row of Figure 17(a). In the same figure, the temporal velocity profiles at three points along the vertical (z) axis are presented. The spatial resolution of the three points is 0.5mm on either sides of axis z. Droplet velocities at the centre of the jet appear to be as high as 190m/s, while from 1.5-5.5ms after triggering the velocity profile at the centre of the jet follows the behaviour of the needle lift profile. At a vertical location of 0.5mm above the centre point (z = -0.5mm), observations of unstable velocities towards the end of injection are evident. The latter is mainly attributed to intense geometric cavitation structures that transiently extend to the exit of the hole during one injection event. On the contrary, at a vertical location of 0.5mm below the centre point of the jet (Figure 17(e), z = +0.5mm), the velocity profile and the angle of the velocity vector exhibit a stable behaviour. Figure 18 also presents temporal velocity distributions for two points at z = -1mm and z = +1mm from the centre of the jet. Velocity variations for both points follow the same trend of instabilities as previously explained, since their location is at the two edges of the jet.

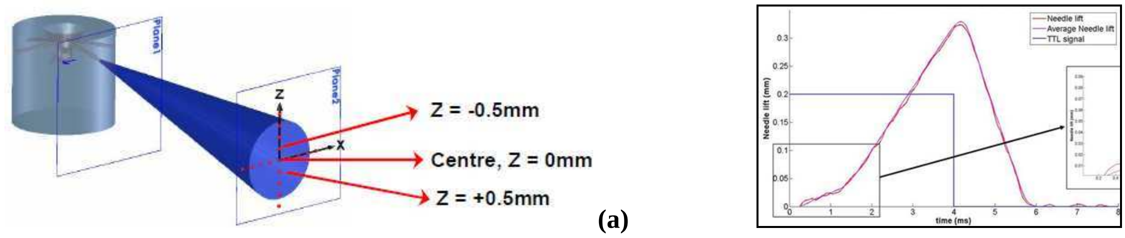

(a)

(b)

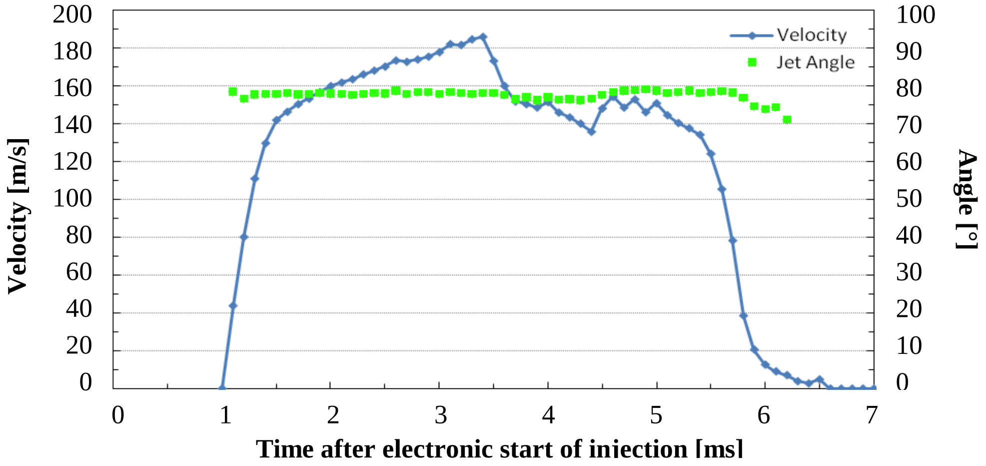

(c)
Point location: z = -0.5mm

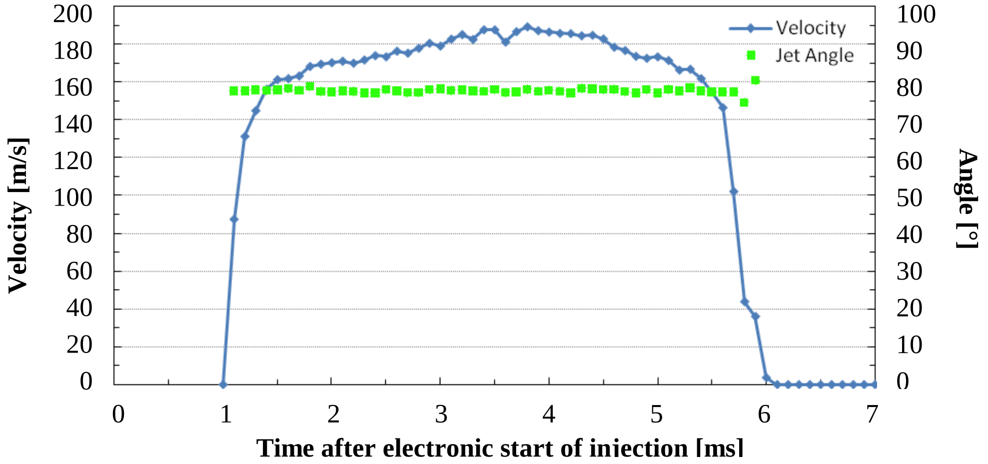

(d)
Centre point: z = 0mm

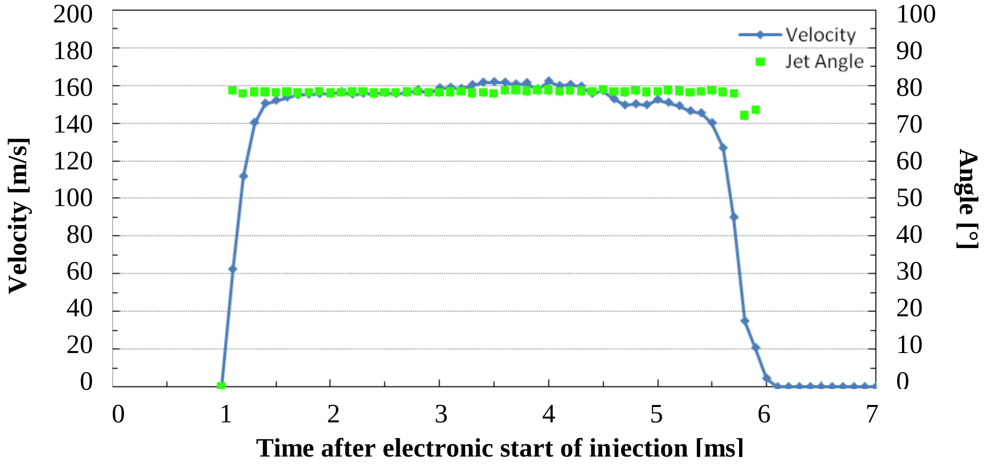

(e)
Point location: z = 0.5mm

Figure 17: (a) Legend of measurements grid. (b) Needle lift profile and temporal velocity profiles at (c) z = - 0.5 mm, (d) at the centre of the jet z = 0 mm and (e) z= 0.5 mm on the z axis.

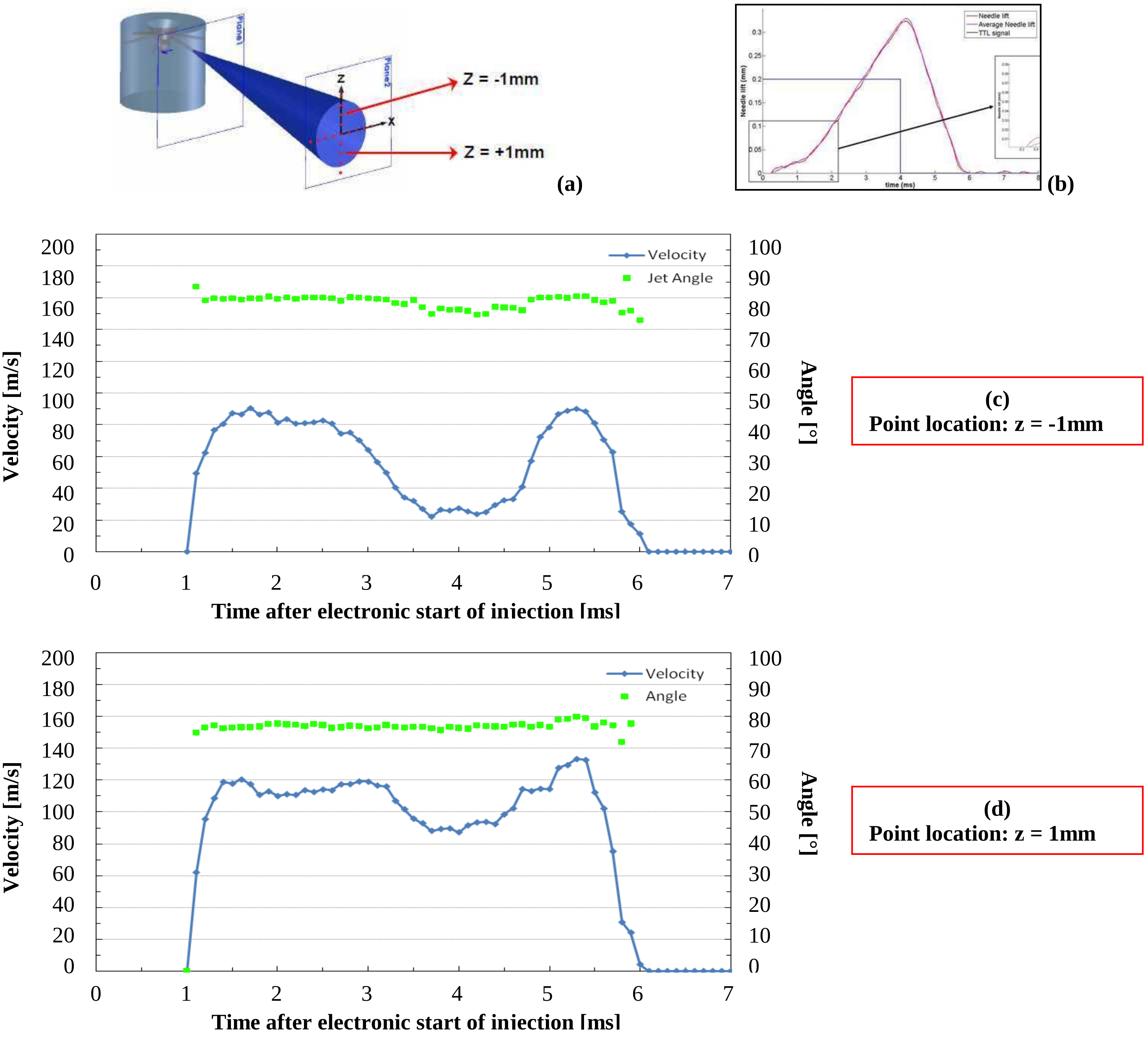

(c)
Point location: z = -1mm

(d)
Point location: z = 1mm

Figure 18: (a) Legend of measurements grid. (b) Needle lift profile and temporal velocity profiles at (c) z = - 1 mm and (d) z= 1 mm on the z axis.

Droplet size distribution at the centre of the VCO nozzle jet is illustrated in Figure 19, in the form of average mean (AMD) and Sauter mean diameter (SMD). Droplet sizing measurements always refer to the complete injection event and neither spatial representation at certain time steps, nor temporal variation graphs at a single point could secure a satisfactory description of the effect. Therefore, a better representation of the phenomenon is achieved, when the comparison is based on the number of droplets that crossed the measuring plane during one injection event, excluding only the tail of the spray. More specifically, judgement upon the normalised distribution graph leads to more accurate conclusions.

The graph presented in Figure 19 includes diameter values from all points measured on the vertical z axis. Although the AMD values vary slightly around the mean value of 10μm, the SMD values present a wider distribution that stabilises at values around 40μm. A rise in SMD values observed at times from 3.5 to 4 ms are directly connected to the needle closing event. The latter distribution is typical high pressure nozzle behaviour; however, it should be stressed that the tested nozzle is not a real nozzle. The transparent cap is not manufactured in a similar way to the real, all-metal, nozzle and the injection pressure is not the nominal operating pressure of production nozzles. As a result, large diameter droplets are expected to be found, contributing to the calculated high SMD values.

Droplet size data gathered from all measurement points, during the complete injection event are illustrated in Figure 20, in a normalised diameter distribution graph. The corresponding mean droplet size value is smaller than the one presented in Figure 19. The reason lies on the fact that, while the presented temporal profile corresponds to data collected during the time velocities have developed and injection has started (i.e. from 1.5 to 5 ms), the normalised diameter distribution graph takes into account the complete injection event after start of injection (i.e. from 1 to 6ms). The observed difference in mean droplet size is then directly connected to small, spherical droplets that are generated during the needle closing time and validated from the measuring system..

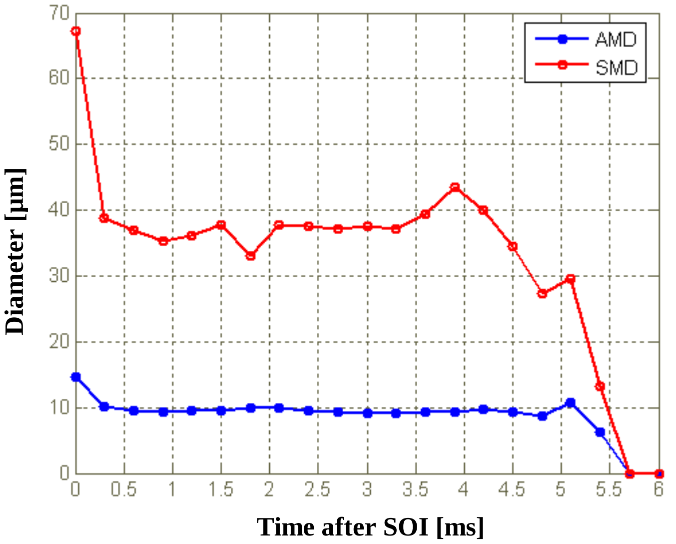

Figure 19: Temporal droplet diameter distribution at the centre of the jet (z = 0mm).

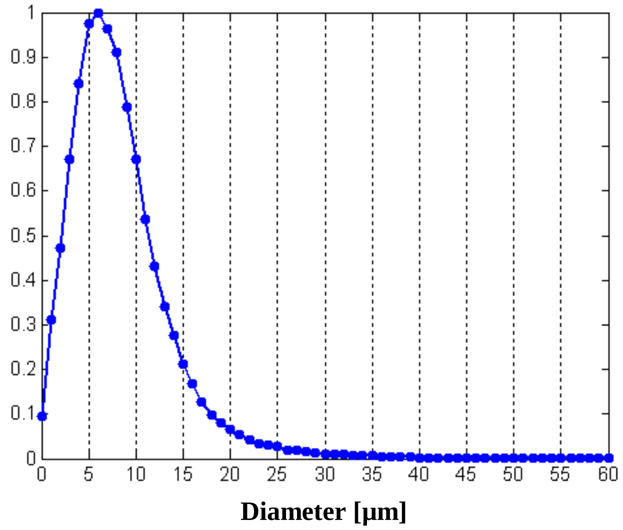

Figure 20: Normalised diameter distribution across all points of the measuring plane during the complete injection duration.

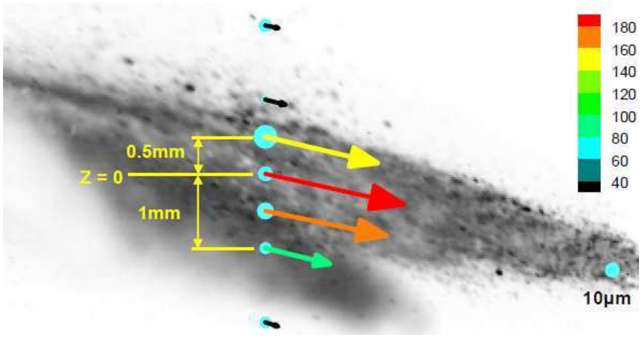

Figure 21: Spatial velocity and size profile for the VCO nozzle at 10mm along the jet axis and 4ms after triggering.

Finally, an overall representation of the measured velocities and droplet sizes across the vertical plane at 10mm along the jet axis, is given in Figure 21, where both the droplet spatial velocity and size distributions are presented; these values refer to 4ms after the triggering of injection, a time when the needle is at its maximum lift according to the previously acquired needle lift data. Moreover, in full accordance with previously presented data, the velocity profiles are those of a typical jet with the velocity values peaking around the centre axis of the jet and becoming smaller at the two edges of the jet. Additionally, the droplet sizing profiles follow the same trend as larger droplets are found at the centre of the jet, while smaller ones tend to move at its edges. Finally, the unstable behaviour of the upper half of the jet is now reflected clearly in the droplet sizing profiles; at 0.5mm above the centre point, the largest droplet diameter of the cross-section can be found.

CONCLUSIONS

Cavitation forming inside the nozzle of fuel injection equipment for Diesel engines represents the main flow feature affecting nozzle discharge coefficient, the momentum of the injected liquid and spray dispersion angle. As demonstrated in the present work, understanding of the flow mechanisms taking place inside high-pressure injection nozzles is a prerequisite for the design of advanced systems that minimise shot – to – shot variations. Moreover, the present study has provided a number of experimental data for string cavitation regarding their origin and their immediate effect on spray instabilities.

High-speed visualisation of cavitation structures forming inside enlarged and real-size VCO Diesel nozzles with cylindrical (parallel) holes has been reported. Dual imaging of cavitation structures inside the nozzle hole and the emerging spray revealed that cavitation enhances spray atomisation; increasing cavitation numbers result in the development of geometric-induced cavitation at the hole entry that, in turn, increases spray atomisation quality. Investigations also revealed and confirmed previous findings of the research group that during transient needle movement (opening and closing phases), when flow inside the hole is not fully developed, strings appear that initiate at the hole exit and travel upstream towards the entry of the hole. Presence of such string structures is found to alter the spray dispersion angle significantly and induce random instabilities. At later stages during the injection event and at times when flow is fully developed inside the hole, string cavitation is identified to initiate at the hole entry. The mechanism of creation is attributed to vortical flow structures present inside the sac volume that are generated due to hole-to-hole flow interaction. The core of these vortices interacts with the intense cavitation structures present at the hole entry, resulting to the creation of cavitation strings, whose core consists of cavitation micro-bubbles coming from already developed geometric-induced structures. Moreover, the location of cavitation strings relative to the geometric-induced cavitation inside the hole is strongly connected to the instability of upper or lower spray boundary.

Similar flow structures have been observed in real-size VCO nozzle replicas and realistic operating conditions. At injection pressures of 30 MPa, during the transient needle movement phase, string cavitation is generated at the hole entry that extends to either sides, on to the needle face, and inside the injection hole. Simultaneous imaging of the emerging spray revealed significant spray instabilities that are also attributed to unstable string cavitation structures. Geometric cavitation is found to enhance atomisation also in real-size VCO nozzles, confirming the agreement between large-scale and real-size nozzle experiments. Finally, PDA measurements on real-size transparent caps revealed that generated spray is directly comparable to that generated by real nozzles thus, such acrylic nozzle tips consist an innovative and extremely informative means of nozzle flow investigations. Spray instabilities observed by the high-speed imaging technique have also been confirmed by the PDA measurements; unstable velocities, and spray angles have been recorded for both, upper and lower, spray boundaries.

Finally, following the understanding of various nozzle flow phenomena and the establishment of links between various forms of cavitation and spray instabilities, a new concept nozzle design has been proposed. This novel design has demonstrated stable spray angles that are directly related to certain design characteristics. The proposed nozzle hole configuration and the elimination of sac volume have diminished hole-to-hole interactions thus, eliminated vertical flow structures. The absence of string cavitation has been confirmed and the “controlled” geometric-induced cavitation demonstrated stable effects on spray dispersion angle and subsequent atomisation quality.

ACKNOWLEDGMENT

The authors would like to thank all staff members and PhD students of the Energy and Transport Research Centre of City University London that have made contributions to the cavitation research programme on Diesel injectors. Finally, the authors would like to express their gratitude to Toyota Motor Co. Japan for financial support on the real-size nozzle tip experiments.

NOMENCLATURE

VCO	Valve covering orifice	
CFD	Computational fluid dynamics	
PDA	Phase – Doppler anemometer	
SOI	Start of injection	
AMD	Arithmetic mean diameter	
SMD	Sauter mean diameter	
CN	Cavitation number	dimensionless
Re	Reynolds number	dimensionless
P_{inj}	Injection pressure	Pa
P_{back}	Chamber pressure	Pa
P_{vapour}	Vapour pressure	Pa

REFERENCES

[1] Chaves, H., M. Knapp, A. Kubitzek, F. Obermeier and T. Schneider, *Experimental study of cavitation in the nozzle hole of diesel injectors using transparent nozzles.* SAE technical paper, 1995. **950290**.

[2] Badock, C., R. Wirth, A. Fath and A. Leipertz, *Investigation of cavitation in real size diesel injection nozzles.* International journal of heat and fluid flow, 1999. **20**(5): p. 538-544.

[3] Arcoumanis, C., M. Badami, H. Flora and M. Gavaises, *Cavitation in real size multi-hole diesel injector nozzles.* Transactions Journal of Engines, SAE paper 2000-01-1249, SAE Transactions, 2000. **109**(3): p. 1485-1500.

[4] Arcoumanis, C., M. Gavaises, J.M. Nouri, E. Abdul-Wahab and R. Horrocks, *Analysis of the flow in the nozzle of a vertical multi-hole diesel engine injector.* Transactions Journal of Engines, SAE paper 980811, SAE Transactions, 1998. **107**(3).

[5] Roth, H., M. Gavaises and C. Arcoumanis, *Cavitation Initiation, Its Development and Link with Flow Turbulence in Diesel Injector Nozzles.* Transactions Journal of Engines, SAE paper 2002-01-0214, SAE Transactions, 2002. **111**(3): p. 561-580.

[6] Afzal, H., C. Arcoumanis, M. Gavaises and N. Kampanis. *Internal flow in Diesel injector nozzles: modelling and experiments*. in *Proc. 3rd IMeCHE International Seminar on Fuel Injection Systems*. 1999. London, 1-2 Dec.

[7] Gavaises, M. and A. Andriotis. *Vortex Cavitation inside Multi-hole Injectors for large Diesel Engines and its Effect on the Near-nozzle Spray Structure*. in *SAE 2006-01-1114*. 2006.

[8] Andriotis, A., M. Gavaises and C. Arcoumanis, *Vortex flow and Cavitation in Diesel Injector Nozzles.* Journal of Fluid Mechanics, 2008. **10**: p. 195-215.

[9] Gavaises, M., A. Andriotis, D. Papoulias, N. Mitroglou and A. Theodorakakos, *Characterization of string cavitation in large-scale Diesel nozzles with tapered holes.* Physics of Fluids, 2009. **21**: p. 052107.

[10] Arndt, R.E.A., *Cavitation in fluid machinery and hydraulic structures.* Annual Review of Fluid Mechanics, 1981. **13**(1): p. 273-326.

[11] Hsiao, C.T. and L.L. Pauley, *Numerical study of the steady-state tip vortex flow over a finite-span hydrofoil.* Journal of fluids engineering, 1998. **120**: p. 345.

[12] Arndt, R.E.A., *Cavitation in vortical flows.* Annual Review of Fluid Mechanics, 2002. **34**(1): p. 143-175.

[13] Hsiao, C.T. and G.L. Chahine, *Numerical study of cavitation inception due to vortex/vortex interaction in a ducted propulsor.* Journal of Ship Research, 2008. **52**(2): p. 114-123.

[14] Nouri, J.M., N. Mitroglou, Y. Yan and C. Arcoumanis, *Internal Flow and Cavitation in a Multi-Hole Injector for Gasoline Direct-Injection Engines.* SAE SP, 2007-01-1405, 2007. **2084**: p. 23.

[15] Gavaises, M., *Flow in valve covered orifice nozzles with cylindrical and tapered holes and link to cavitation erosion and engine exhaust emissions.* International Journal of Engine Research, 2008. **9**(6): p. 435-447.

[16] Gavaises, M., D. Papoulias, E. Giannadakis, A. Andriotis, N. Mitroglou, and A. Theodorakakos, *Comparison of cavitation formation and development in Diesel VCO nozzles with cylindrical and converging tapered holes*, in *THIESEL 2008.* 2008: Valencia, Spain, 8-10 Sept, 2008.

[17] Andriotis, A., M. Spathopoulou and M. Gavaises. *Effect of nozzle flow and cavitation structures on spray development in low-speed two-stroke Diesel engines*. in *25th CIMAC World Congress on Combustion Engine Technology*. 2007. 21–24 May 2007, Vienna.

[18] Soteriou, C., R. Andrews, N. Torres, M. Smith and R. Kunkulagunta. *Through the diesel nozzle hole–a journey of discovery*. in *ILASS-Europe. 2001*. 2001. September 2-6. Zurich, Switzerland.

[19] Blessing, M., G. Konig, C. Kruger, U. Michels and V. Schwarz. *Analysis of flow and cavitation phenomena in diesel injection nozzles and its effects on spray and mixture formation*. 2003: Professional Engineering for the Institution of Mechanical Engineers.

[20] Soteriou, C., M. Lambert, S. Zuelch and D. Passerel. *The flow characteristics of high efficiency Diesel nozzles with enhanced geometry holes*. in *THIESEL International Conference on Thermo- and Fluid Dynamic Processes in Diesel Engines*. 2006. Valencia, Spain.

[21] Soteriou, C.C.E., M. Smith and R.J. Andrews. *Cavitation Hydraulic Flip and Atomization in Direct Injection Diesel Sprays, IMechE*. in *IMechE*. 1993. London.

[22] He, L. and F. Ruiz, *Effect of cavitation on flow and turbulence in plain orifices for high-speed atomization.* Atomization and Sprays, 1995. **5**(6): p. 569-584.

[23] Soteriou, C., R. Andrews and M. Smith, *Direct injection diesel sprays and the effect of cavitation and hydraulic flip on atomization.* SAE technical paper, 1995. **950080**.

[24] Kim, J.H., K. Nishida and H. Hiroyasu, *Characteristics of the internal flow in a diesel injection nozzle.* International Journal of Fluid Mechanics Research, 1997. **24**(1-3).

[25] Soteriou, C., M. Smith and R. Andrews. *Diesel injection: laser light sheet illumination of the development of cavitation in orifices*. in *IMechE Paper C529/018/98*. 1998.

[26] Giannadakis, E., D. Papoulias, M. Gavaises, C. Arcoumanis, C. Soteriou, and W. Tang, *Evaluation of the predictive capability of diesel nozzle cavitation models.* SAE Paper 2007-01-0245, 2007.

[27] Miranda, R., H. Chaves, U. Martin and F. Obermeier, *Cavitation in a Transparent Real Size VCO Injection Nozzle*. Proceedings of ICLASS, Sorrento Italy, 2003.

[28] Arcoumanis, C., M. Gavaises, H. Flora and H. Roth, *Visualisation of Cavitation in Diesel Engine Injectors.* Mec.Ind., 2001. **2**: p. 375-381.

[29] Roth, H., E. Giannadakis, M. Gavaises, C. Arcoumanis, K. Omae, I. Sakata, M. Nakamura, and H. Yanagihara, *Effect of Multi-Injection Strategy on Cavitation Development in Diesel Injector Nozzle Holes.* Transactions Journal of Engines, SAE paper 2005-01-1237, 2005. **114-3**: p. 1029-1045.

[30] Giannadakis, E., , *Modelling of Cavitation in Automotive Fuel Injector Nozzles* in *Mechanical Engineering, Thermofluids Section*. 2005, Imperial College, University of London: London.

[31] Schmidt, D., C.J. Rutland and M.L. Corradini, *A FULLY COMPRESSIBLE, TWO-DIMENSIONAL MODEL OF SMALL, HIGH-SPEED, CAVITATING NOZZLES.* Atomisation and Sprays, 1999. **9**(3): p. 255-276.

[32] Singhal, A.K., M.M. Athavale, H. Li and Y. Jiang, *Mathematical basis and validation of the full cavitation model.* Journal of fluids engineering, 2002. **124**: p. 617.

[33] Graham, M., N. Keeler and J. Kewley. *Ultra-high pressure common rail systems*. in *Injection Systems for IC Engines*. 2009. IMechE, London, UK.

[34] Giannadakis, E., M. Gavaises and A. Theodorakakos. *The Influence of Variable Fuel Properties in High-Pressure Diesel Injectors*. in *SAE 2009-01-0832*. 2009.

[35] Gavaises, M., D. Papoulias, A. Andriotis, E. Giannadakis and A. Theodorakakos. *Link Between Cavitation Development and Erosion Damage in Diesel Injector Nozzles*. in *SAE 2007-01-0246*. 2007.

[36] Liverani, L., C. Arcoumanis, H. Yanagihara, I. Sakata and K. Omae. *Imaging of the Flow and Cavitation Formation in a Transparent Real-Size Six-Hole Nozzle under Realistic Conditions*. in *COMODIA, Paper SC14*. 2008. Hokkaido University, Japan.

[37] Liverani, L., *Cavitation in Real-Size Diesel Injector Nozzles*, in *School of Engineering and Mathematical Sciences*. 2010, City University London: London.

[38] Gavaises, M., A. Andriotis and C. Arcoumanis, *Complex cavitation structures in Diesel fuel injector nozzles*, in *IMechE conference on "Injection Systems for IC Engines"* 2009: London, 13-14 May, 2009.

DROP IMPACT OF A CONCENTRATED COLLOIDAL SUSPENSION

M. Muratore[1], V. Bertola[1], M.D. Haw[2]

[1]University of Liverpool, School of Engineering, Harrison Hughes Building, Liverpool L69 3BX, UK
[2]University of Strathclyde, Department of Chemical and Process Engineering, James Weir Building, 75 Montrose Street, Glasgow G1 1XJ, UK

ABSTRACT

The impact of drops of a concentrated colloidal suspension of nearly hard-core particles in octadecene (volume fraction: 59.6%) onto solid surfaces is studied experimentally by high-speed imaging, for impact Weber numbers ranging between 26 and 262, and for different values of the target surface energy. Upon impact, these drops do not exhibit inertial spreading, which is observed for other Newtonian and non-Newtonian fluid drops. On wettable surfaces (glass), impact is followed by capillary-driven spreading at the same rate observed in Newtonian fluids (Tanner's law), while on less wettable surfaces (PTFE) colloidal suspension drops relax to achieve the shape of a spherical cap, but do not spread. This peculiar impact morphology, and in particular the absence of inertial spreading, is interpreted as a consequence of dilatancy and jamming occurring upon impact.

INTRODUCTION

The impact morphology of liquid droplets onto solid, dry surfaces, is well-known (see e.g. [1-4]). Upon impact, the liquid spreads on the surface taking the form of a disk; for low impact velocity, the disk thickness is approximately uniform, while for higher impact velocities the disk is composed of a thin central part (often called "lamella") surrounded by a circular rim. This initial spreading stage is typically very fast (≈5 ms). After the drop has reached maximum spreading, two qualitatively different outcomes are possible.

If the initial kinetic energy exceeds a threshold value capillary forces are insufficient to maintain the integrity of the drop, which disintegrates into smaller satellite droplets jetting out of its outermost perimeter (splashing). If splashing does not occur, the drop is allowed to retract under the action of capillary forces, which tend to minimize the contact with the surface; in some cases, retraction is so fast that the liquid rises in the middle forming a Worthington jet, which may subsequently result in the complete rebound of the drop from the surface.

Whilst there exists a significant volume of literature about single drop impacts of simple (Newtonian) fluids, the number of works about fluids with complex microstructure (polymer melts or solutions, gels, pastes, foams and emulsions, etc.) is comparatively very small. However, these fluids are frequently used in common applications, such as painting, food processing, and many others.

The microscopic structure of fluids is described from the macroscopic point of view of continuum mechanics by constitutive equations, which express the relationship between the stress tensor and the velocity gradient. Simple liquids, such as water, are generally characterized by a Newtonian constitutive equation, where the stress tensor is a linear function of the velocity gradient, whereas in complex (or non-Newtonian) fluids the stress tensor is a generic function of the velocity gradient and of its derivatives. [5,6].

Thus, the study of non-Newtonian drops requires a completely different modelling approach, as well as different sets of experimental data, depending on the form of the constitutive equation of the fluid. In particular, due to the large spatial and temporal gradients observed during drop impacts, small changes in the constitutive equation result into large macroscopic effects (for example, most drop impact models become inaccurate for large fluid viscosities [7]).

An important example of complex fluid is represented by pastes, which are widely used in many industrial processes such as cosmetics, pharmaceutical, and food industry. Pastes can be described as concentrated suspensions of colloidal particles (i.e., particles with size in the range between a few nm and a few μm) in a fluid medium.

Despite the practical importance of colloidal flows [8,9], they are still poorly understood in comparison with other complex fluids, and studies on model systems were carried out only recently [10]. A peculiar characteristic of colloidal flows is the appearance of strong non-linearities, such as yielding, shear-thickening, and shear localisation or apparent wall slip due to particle depletion near solid walls [11-14]. Moreover, specific applications (e.g., microfluidics) may involve geometric dimensions comparable with the particle size, leading to confinement effects [15].

When a highly concentrated suspension of particles is forced to flow, its volume must increase on shearing to enable motion. Dilation within a fixed volume of suspending liquid eventually causes particles to encounter the air-liquid interface. This generates large capillary forces at the free surface, which can then balance the normal inter-particle forces and resist further motion, jamming the sample [16].

This work presents the preliminary results of drop impact experiments of a suspension of near hard-core colloidal particles, with the purpose to investigate the impact morphology in the presence of shear thickening or jamming, which may be induced by the large velocity gradients arising upon drop impact.

MATERIALS AND METHODS

Fluid preparation and characterisation

A model colloidal suspension characterised by nearly hard-core (purely repulsive) interactions was prepared with poly-methyl-methacrylate (PMMA, density: 1180 kg/m^3) spheres (radius r ~ 604nm, 5% polydispersity) sterically stabilised by poly-12-hydroxy stearic acid (PHSA) chemically grafted onto their surface [17], and suspended in octadecene (density: 789 kg/m^3; surface tension: 0.03 N/m).

In order to ensure that particles interact as hard spheres, the fluid medium must be a poor solvent for PMMA, in order to limit particles swelling, but a good solvent for PHSA so that polymer chains stretch out. When two particles come into contact, the repulsive energy given by the superposition of the two polymer layers rapidly increases as the distance between particles reduces [18]. Among the various suitable solvents, octadecene was selected because of its very low volatility.

Suspensions were centrifuged at 2000 rpm for 12 hours to create a sediment, which was assumed to have a concentration of 64% (random close packing or maximum random packing) [19]. The sediment was then diluted with octadecene to a concentration of 59.6%, corresponding to a density of 1022 kg/m^3.

According to the equilibrium thermodynamics phase diagram of ideal hard-spheres [20], for volume fractions between 54.5% and 74% (maximum crystalline close packing fraction) the system is crystalline. However, experiments showed that model suspensions of sterically-stabilized colloidal hard-spheres failed to crystallize for volume fractions greater than 58%, remaining in a non-equilibrium phase known as the colloidal glass [21].

Figure 1 shows examples of flow curves for dense hard-sphere suspensions at different volume fractions [22]. For concentrations above 56%, fluids exhibit strong shear thickening at shear rates of the order of 50 s^{-1}.

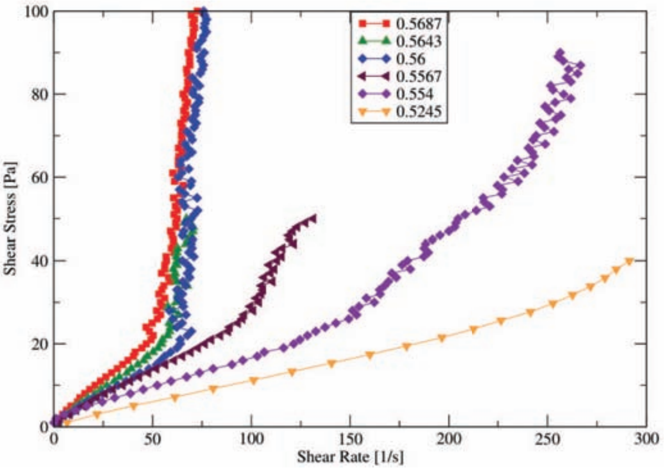

Figure 1. Flow curves of dense suspensions of PMMA particles (r = 613 nm), for different volume fractions [22].

Shear-thickening could be an indication of jamming inside the fluid sample. Indeed, dilatancy and jamming can be directly related to shear-thickening during extensional rheology experiments [23]. For shear rates below the shear-thickening point, fluids exhibit a Newtonian behaviour, with shear viscosities of the order of 0.5 Pa·s.

For the sake of comparison, a Newtonian fluid with a measured viscosity of 0.55 Pa·s was obtained by preparing a 96% solution of glycerol in water (density: 1250 kg/m^3).

Experimental setup and procedure

Drops were generated using a syringe with blunt hypodermic needle (gauge 21, 0.495 mm i.d.) driven by a micrometric screw, and detached under their own weight. The needle was suspended above two substrates of different surface energy (glass and PTFE). To change the impact velocity, the drop release height was adjusted between 2 and 18 cm using a Vernier height gauge, which corresponds to theoretical free-fall velocities between 0.6 and 1.9 m/s.

The competition between inertia and surface forces was characterised through the Weber number, $We = \rho v^2 D_0/\sigma$, where ρ is the suspension density, σ is the solvent surface tension, v is the drop velocity, and D_0 the characteristic diameter before impact.

A high-frame rate CMOS camera (Phantom v9000) equipped with a zoom lens (Navitar 7000) and horizontally aligned with the surface recorded the impacts of single drops. Back-to-front illumination was provided by a LED backlight (Philips AccentLed) which ensured a uniform illumination intensity, and images with a resolution of 576×576 pixels were captured at 4000 frames per second. Magnification was kept constant throughout all experiments and lengths on the image could be calculated by comparison with a reference length (spatial resolution: 16.26 µm/pixel). To ensure a fine optical alignment, the camera, the heated surface and the backlight were fixed to an optical breadboard.

Quantitative data were extracted from images using proprietary software developed in LabView environment, which after background subtraction and image optimization measured the base diameter of drops, as well as the left and right contact angles using the drop profile tangent method.

The characteristic drop diameter before impact, measured by comparison with a known reference length, was 2.208±0.075 mm, resulting into Weber numbers ranging from 26 to 262.

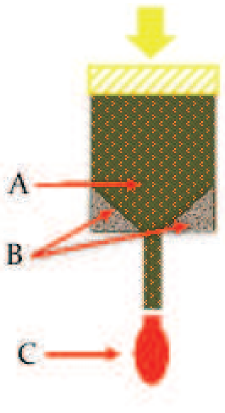

Figure 2. Schematic of the syringe-needle dispensing system (see text for description).

Although the syringe-needle dispensing system described above ensures a very good reproducibility of the drop diameter, the particle concentration may not remain constant as the two-phase (solid-liquid) mixture is pushed through the needle. In fact, the higher resistance encountered in the sudden contraction and in the needle is likely to induce self-filtration, favouring the flow of the suspending liquid with respect to particles. With reference to Figure 2, when the mixture approaches the contraction (a) the velocity of particles becomes smaller than that of the liquid (i.e., the liquid/solid slip ratio become greater than one); some of the particles accumulate in the corners of the contraction (b). Thus, the particle concentration in the drop (c) is probably smaller than in the syringe reservoir, and slowly varies as the syringe is emptied.

RESULTS

Figure 3 compares the drop impact morphologies of colloidal drops impacting with the same Weber number (We=145) on solid substrates characterised by different surface energy (glass and PTFE).

These images suggests that at the moment of impact colloidal suspension drops are not necessarily spherical, but may exhibit deformations created at the moment of drop generation, similar to what happens during the generation of viscoplastic drops from capillary nozzles [24]. Such deformations eventually disappear as the drop is deposited on the target surface and takes the shape of a spherical cap under the action of capillary forces. These images also show that the inertial spreading of drops, which usually occurs in the first 5 ms after impact, is not noticeable on either surface, although one can observe capillary-driven spreading on the glass substrate at longer times after the impact.

The base diameter (non-dimensionalised with respect to the characteristic drop diameter, D_0) of colloidal suspension drops impacting on a glass surface is plotted as a function of time in Figure 4, for different impact velocities hence different Weber numbers. Upon impact, the drop base diameter has a modest inertial deformation for less than 1 ms, then remains almost constant before the beginning of capillary-driven spreading. Surprisingly, increasing the Weber number, i.e. the impact kinetic energy, reduces the inertial deformation; moreover, in the range of Weber numbers considered, at the end of inertial expansion the base diameter remains smaller than the drop equilibrium diameter.

These observations suggest that upon impact the colloidal suspension jams, and therefore large inertial deformations are not possible; increasing the impact kinetic energy jamming is quicker, which further reduces the inertial deformation. For longer times (> 100 ms), irrespective of the Weber number, spreading continues at the rate $D \sim t^{1/10}$, as predicted by Tanner's law for Newtonian drops [25].

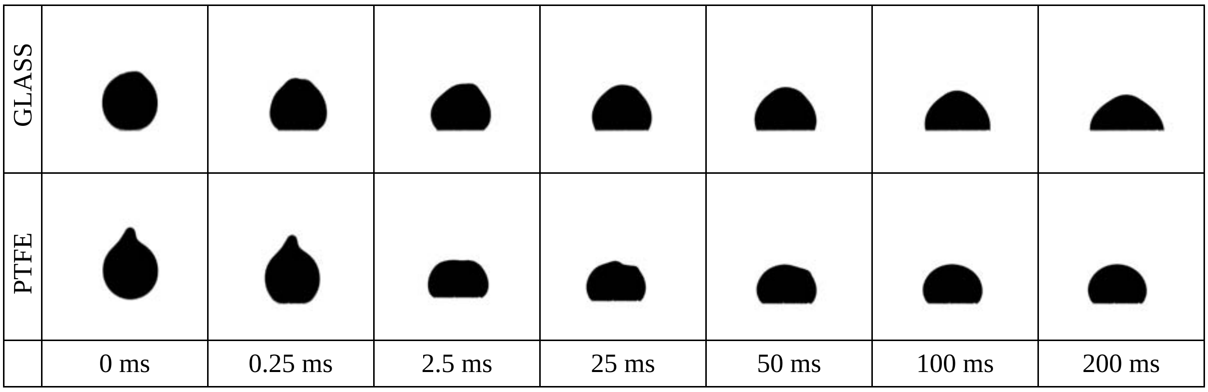

Figure 3. Drop impact morphology of colloidal suspension drops (volume fraction: 59.6%) impacting on glass and PTFE surfaces, for We = 145.

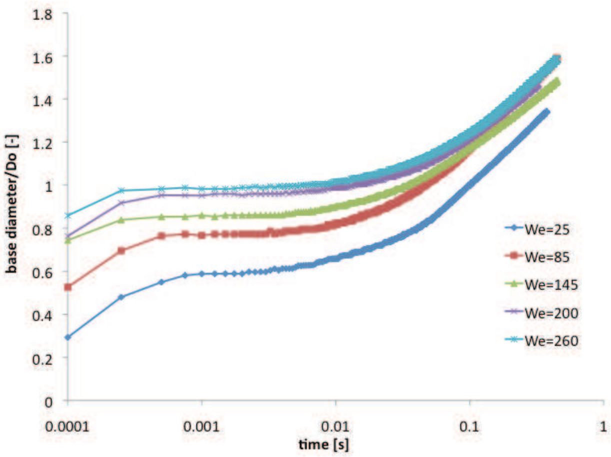

Figure 4. Dimensionless base diameter of colloidal suspension drops (Φ = 59.6%) impacting on a glass surface.

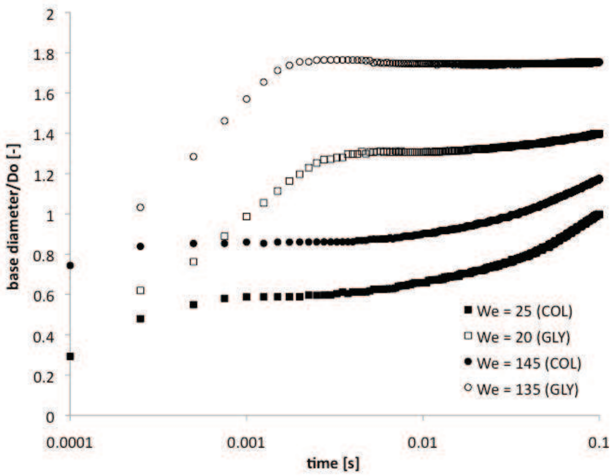

Figure 5. Comparison between the base diameters of colloidal suspension drops and Newtonian drops impacting on glass.

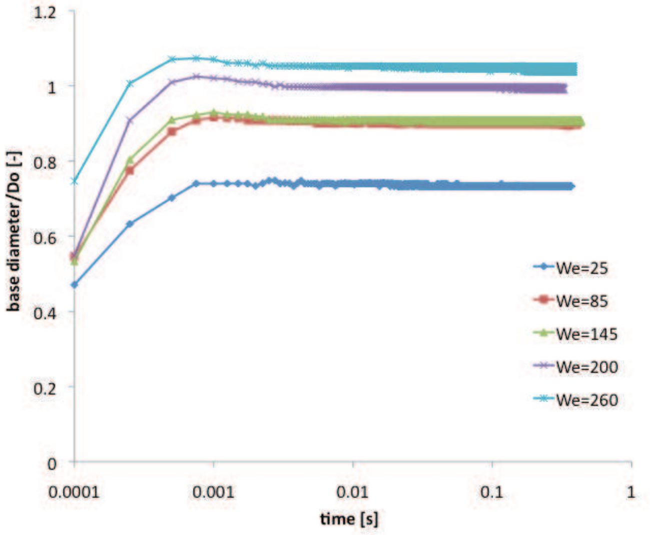

Figure 6. Dimensionless base diameter of colloidal suspension drops (Φ = 59.6%) impacting on a PTFE surface.

Figure 5 compares the base diameters of two colloidal suspension drops and two Newtonian drops with a viscosity of 0.55 Pa·s (i.e., a viscosity similar to that of the colloidal suspension before shear-thickening, see Figure 1). Despite the similar viscosity, the inertial spreading of the Newtonian drops is larger and has a longer duration (3-5 ms) than that of colloidal suspension drops; as expected, the drop deformation increases as the Weber number grows. This comparison provides further evidence that the impact on a solid substrate, even from a modest falling height, is able to cause jamming in colloidal suspension drops.

Figure 6 shows the base diameter of colloidal drops impacting on a PTFE surface. The inertial deformation upon impact is again of very small amplitude and short duration (about 1 ms). Unlike in the case of the glass surface, no capillary-driven spreading can be observed, and the base diameter remains constant for an indefinite time. It is interesting to observe that drops with different impact Weber numbers do not exhibit the tendency to attain a same equilibrium value of the base diameter, i.e. the value determined by the Young-Laplace equation, but seem to remain frozen (jammed) in the state they reach upon impact.

The comparison with Newtonian drops impacting on the same surface (Figure 7) shows that, in addition to significant inertial deformations, Newtonian drops are also able to partially retract, in order to attain the equilibrium base diameter value. Note that the equilibrium value of the glycerol solution drops base diameter is significantly different from any of the colloidal suspension drop base diameters because the fluids have different surface tensions. Moreover, in colloidal suspension drops the base diameter (hence the contact angle) depends strongly on the impact Weber number, meaning that the contact angle cannot be determined using the Young-Laplace equation, but rather depends on the initial small inertial deformation and on particles jamming.

CONCLUSIONS

The impact of concentrated colloidal suspension drops onto solid surfaces was studied by high-speed imaging, and compared with Newtonian drops of similar viscosity.

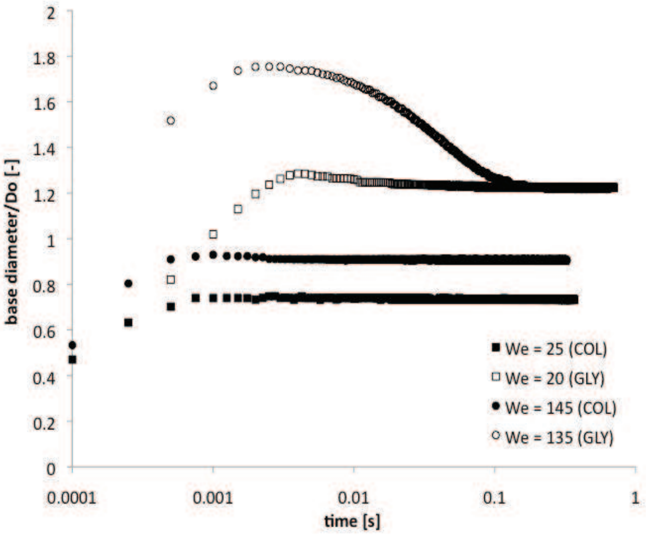

Figure 7. Comparison between the base diameters of colloidal suspension drops and Newtonian drops impacting on PTFE.

Experiments show that concentrated colloidal suspension drops do not exhibit large inertial deformations, which suggests that the impact induces dilatancy and jamming of colloidal particles, which prevent the drop deformation.

On glass substrates, at longer time scales one can observe capillary-driven spreading, where the spreading rate is about the same as that of Newtonian drops.

On PTFE substrates, capillary spreading cannot be observed, and the drop base diameter remains constant after impact. The base diameter value depends on the impact Weber number, which suggests that wetting plays a negligible role in comparison to the initial inertial deformation and the subsequent jamming of the colloidal suspension.

ACKNOWLEDGMENTS

The Authors thank A. Schofield for particle synthesis and L. Isa for permission to reproduce flow curves from his thesis.

REFERENCES

[1] M. Rein, Phenomena of liquid-drop impact on solid and liquid surfaces, Fluid Dynamics Research, vol. 12(2), pp. 61-93, 1993.
[2] R. Rioboo, C. Tropea and M. Marengo, Outcomes from a drop impact on solid surfaces, Atomization & Sprays, vol. 11, pp. 155-166, 2001.
[3] R. Rioboo, M. Marengo and C. Tropea, Time evolution of liquid drop impact onto solid, dry surfaces, Exp. Fluids, vol. 33, pp. 112-124, 2002.
[4] A. L. Yarin, Drop impact dynamics: Splashing, spreading, receding, bouncing, Annu. Rev. Fluid Mech., vol. 38, pp. 159–192, 2006.
[5] R. G. Larson, The Structure and Rheology of Complex Fluids, Oxford University Press, New York, 1999.
[6] G. Astarita, G. Marrucci, Principles of Non-Newtonian Fluid Mechanics, McGraw-Hill, New York, 1974.
[7] G. German, V. Bertola, Review of drop impact models and validation with high-viscosity Newtonian fluids, Atomization and Sprays, vol. 19, pp. 787-807, 2009.

[8] J. A. Lewis, Colloidal Processing of Ceramics, Journal of the American Ceramic Society, vol. 83, pp. 2341-2359, 2000.

[9] D. I. Wilson, S. L. Rough, Exploiting the curious characteristics of dense solid–liquid pastes, Chemical Engineering Science, vol. 61, pp. 4147-4154, 2006.

[10] M. D. Haw, Jamming, two-fluid behaviour and self-filtration in concentrated colloidal suspensions, Physical Review Letters, vol. 92, 185506, 2004.

[11] G. Petekidis, D. Vlassopoulos, P. N. Pusey, Yielding and flow of sheared colloidal glasses, J. Phys.: Condens. Matter, vol. 16, S3955, 2004.

[12] K. N. Pham, G. Petekidis, D. Vlassopoulos, S. U. Egelhaaf, P. N. Pusey, W. C. K. Poon, Yielding of colloidal glasses, Europhysics Letters, vol. 75, pp. 624-630, 2006.

[13] W. J. Frith, P. d'Haene, R. Buscall, J. MewisShear thickening in model suspensions of sterically stabilized particles, J. Rheol. 40, 531-548 (1996)

[14] P. Coussot, Rheophysics of pastes: a review of microscopic modeling approaches, Soft Matter, vol. 3, pp. 528-540, 2007.

[15] D. Psaltis, S.R. Quake, C. Yang, Developing optofluidic technology through the fusion of microfluidics and optics, Nature, vol. 442, pp. 381–386, 2006.

[16] M. E. Cates, M. D. Haw and C. B. Holmes, Dilatancy, jamming and the physics of granulation, J. Phys. Cond. Matt., vol. 17, S2517, 2005.

[17] L. Antl, J. W. Goodwin, R. D. Hill, R. H. Ottewill, S. M. Owens, S. Papworth, J. A. Waters, The preparation of poly(methyl-methacrylate) lattices in non-aqueous media, Colloids and Surfaces, vol. 17, pp. 67-78, 1986.

[18] B. A. de L. Costello, P. F. Luckham, Th. F. Tadros, Investigation of the interaction forces of polymer-coated surfaces using force balance, rheology, and osmotic pressure results, Langmuir, vol. 8, pp. 464-468, 1992.

[19] J. D. Bernal, The bakerian lecture, 1962: The structure of liquids, Proceedings of the Royal Society A, vol. 280, pp. 290-321, 1964.

[20] W. W. Wood, J. D. Jacobson, Preliminary results from a recalculation of the Monte Carlo equation of state of hard spheres, Journal of Chemical Physics, vol. 27, pp. 1207-1208, 1957.

[21] P. N. Pusey, W. van Megen, Phase behaviour of concentrated suspensions of nearly hard colloidal spheres, Nature, vol. 320, pp. 340-342, 1986.

[22] L. Isa, Capillary flow of dense colloidal suspensions, Ph.D. Thesis, University of Edinburgh, 2008.

[23] M. I. Smith, R. Besseling, M. E. Cates, V. Bertola, Dilatancy in the flow and fracture of stretched colloidal suspensions, Nature Communications, vol. 1, 114, 2010.

[24] G. German, V. Bertola, Formation of viscoplastic drops by capillary breakup, Physics of Fluids, vol. 22, 033101, 2010.

[25] L. H. Tanner, The spreading of silicone oil drops on horizontal surfaces, J. Phys. D: Appl. Phys. 12, pp. 1473, 1979.

DIPSI Workshop 2011 on Droplet Impact Phenomena & Spray Investigation
May 27, 2011, Bergamo, Italy

EXPERIMENTAL AND NUMERICAL INVESTIGATION OF THE DROPLET BEHAVIOR PASSING A COMPRESSOR CASCADE

B. Ober*, C. Storm*, H. Gomaa°, S. Seifert°, B. Weigand°, F. Joos*

*Laboratory of Turbo Machinery / Power Engineering
Helmut Schmidt University / University of the Federal Armed Forces; 22043 Hamburg, Germany
°Institute of Aerospace Thermodynamics
University of Stuttgart; 70569 Stuttgart, Germany

ABSTRACT

High fogging systems are often used in gas turbine power stations for power augmentation. Water droplets injected into the compressor inlet will partly follow the air flow, will partly be splashed at the compressor blades and partly touch the surface of the blades. The water film of the surface will be atomized at the trailing edge of the blade.

The work presented concerns with the numerical calculation of the spray behavior passing a transonic compressor cascade investigating droplet atomization. The physical models used are discussed in detail. The comparison with measurements of the droplet velocity as well as of the droplet size distribution of the transonic two phase flow inside a planar compressor cascade explains the accuracy of the physical models used in the numerical investigation.

INTRODUCTION

The ongoing change towards the use of renewable sources of energy imposes new challenges to the grid with regard to grid stability. Presently available storage capacity is not sufficient to stabilise the fluctuating power output of electric energy sources such as wind or solar. In order to cope with these fluctuations an energy supply system is needed that is able to adapt quickly to the demand. Gas turbines have, due to their short start up times, proven a reliable support in ensuring a stable grid. But yet a more efficient and more capable gas turbine system remains desirable. One way to augment the power output and increase the efficiency of a gas turbine is the injection of water droplets into the inlet structure (1).

The mechanisms that determine the behaviour of the water spray in the compressor of a gas turbine are not yet fully understood. Moreover remains the testing in this field of research demanding because of the efforts that have to be taken with regard to energy consumption and equipment (2). Therefore the implementation and validation of numerical test methods is a key milestone on the road to employ the entire potential of this technology.

In order to take the development one step further the authors have conducted numerical and experimental investigations on the droplet behaviour passing a compressor cascade.

APPROACH

The Laboratory of Turbo Machinery at the Helmut Schmidt University in Hamburg, Germany possesses a high speed wind tunnel. The results obtained during the experimental investigations conducted at this test facility serve as the data basis for the numerical investigations for which two different approaches were chosen. One study dealt with two existing particle breakup models implemented in AVL Fire which aimed at the assessment of the general behaviour and flexibility of the respective model. Within the second study a standalone model that communicates directly with ANSYS CFX was tested to clarify its suitability to predict the prevalent phenomena in a cascade flow. The calculations conducted in Stuttgart used Fire by AVL. In Hamburg a self developed code for the dispersed phase (DPF) which communicates with ANSYS CFX was used. Both packages utilize the Navier-Stokes-Equations which will not be discussed in detail in this work. Further information can be found in various publications (3).

EXPERIMENTAL INVESTIGATION

Test Rig

The wind tunnel which is capable of delivering supersonic flow regimes consists of the major components:

- centrifugal compressor
- settling chamber
- intake duct with film layer injection
- cascade
- water separator

The basic setup is depicted in Figure 1.

The compressed air supplied by the centrifugal compressors (not depicted) is fed into the settling chamber where the flow is equalised. The compressors are capable of delivering a supercritical pressure ratio. The maximum Mach number in the test section is Ma=1.2. A high pressure pump atomizes desalinated water into the settling chamber.

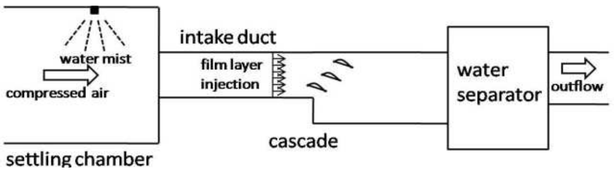

Figure 1:BASIC SETUP OF TEST RIG (4)

Constructional boundary conditions demand an intake duct of *l*= 2m. The imposed boundary layer has to be accounted for during two dimensional testing. This is achieved by a film layer injection which accelerates the flow close to the side walls.

The test section is depicted schematically in Figure 2. It contains a compressor blade cascade of nine controlled diffusion airfoils. The blade contour is derived from a cross section of an actual axial compressor profile which has been extruded. Glass windows allow optical accessibility.

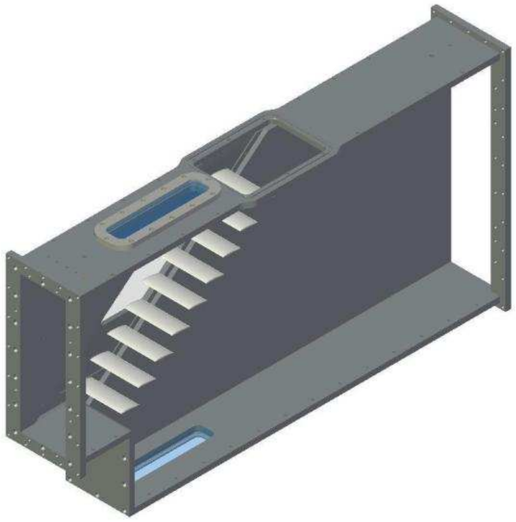

Figure 2: TEST SECTION (4)

Measurement technique

Test results comprise of velocity and diameter information of the droplets passing the cascade. A two dimensional Laser Doppler Anemometry and Phase Doppler Anemometry setup (2D LDA/PDA) delivers the necessary information. The light source is an argon ion laser with a power output of 4W.

The field of interest is captured in a point to point measurement with 1200 nodes. The dry flow is examined with 2000 samples and 5000 for the droplet laden flow respectively. The velocity information of a dry flow is recorded with the use of Di-Ethyl-Hexyl-Sebacat (DEHS) droplets which can be easily atomized to sizes which are known to follow the air flow with negligible deviation $(d < 0.3\ \mu\mathrm{m})$ (1).

Droplet classification

The diameter distribution can be evaluated by the use of the Sauter-Mean-Diameter (SMD) D_{32}. It is given by:

$$D_{32} = \frac{\sum_{i=1}^{N} n_i d_d^3}{\sum_{i=1}^{N} n_i d_d^2} \tag{1}$$

Herein N is the number of droplet size classes, n_i is the number of particles in the respective size class and d_d is the corresponding diameter. The SMD is a useful measure to analyse droplet behaviour with regard to evaporation as it is the ratio of the dispersed phase's volume and surface.

A characteristic flow induced by a Controlled Diffusion Airfoil (CDA) incorporates a regime of high velocity on the suction side of the profile. Therefore the description of droplet behaviour has to consider three phenomena in the compressor application.

Experimental data

The measurements were carried out by (4) using the parameters:

Table 1: CASCADE FLOW CONDITIONS

Parameter	Value
Mach number	0.85
Reynolds number	673000
Temperature	293 K
Total pressure	1260 mbar
AVDR	≈ 1.08
Flow angle β_1	35.6 deg
incidence	0 deg

Results of the dry reference air flow show a typical velocity distribution of a compressor profile of this type as depicted in Figure 3. The incident flow is accelerated on the suction side of the profile and forms a transonic flow regime. Further downstream the flow is decelerated to subsonic velocities. Most characteristic for this type of blade is the rapid acceleration which imposes high relative velocities to any inert particle passing the area.

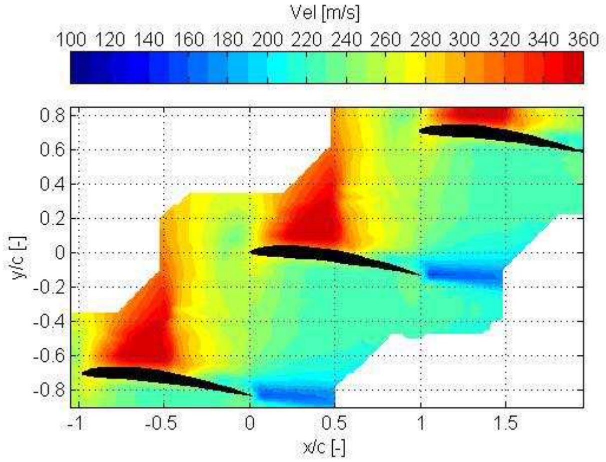

Figure 3: EXPERIMENT: DRY AIR (4)

The effects can be seen in Figure 4. Depicted is the SMD of a droplet laden flow. The results show a quasi uniform diameter distribution at the cascade entrance of 50-55 µm. In the area which is characterized by transonic velocities in Figure 3 a decrease in SMD is observed.

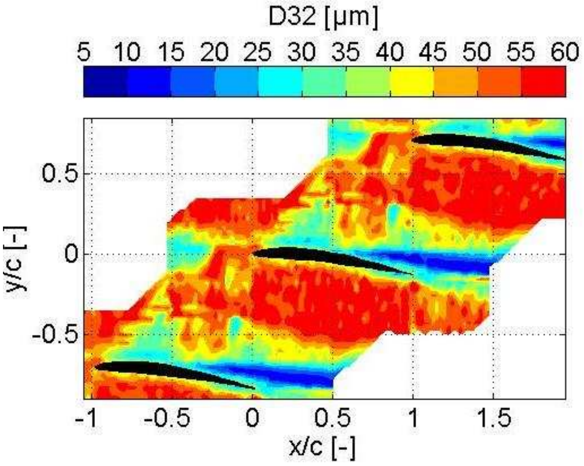

Figure 4: EXPERIMENT: SMD (4)

Calculations of the Weber number based on the relative velocity and a mean droplet diameter $d = 20...40\ \mu m$ (Figure 5) however show a maximum value of $We_{max} = 3$ which is well below the critical value of $We_{crit} = 12$ for droplet breakup (5). Based on this information it can be assumed that breakup does not occur for $d_d \leq 40\ \mu m$. The discrepancy between measurement and phenomenological investigation can be justified with the inability of PDA to account for deformed droplets and the sensitivity of SMD calculation to large diameters as (4) reported. The influence on much larger droplets are not yet quantified. Future investigations will have to clarify the critical droplet diameter for s to occur. Downstream of the transonic flow regime a reduced SMD of $D_{32} = 5...15\ \mu m$ is recorded. This is partly due to small droplets as a result of the splashing phenomenon on the leading edge of the blade and partly due to the water film disintegration on the suction side.

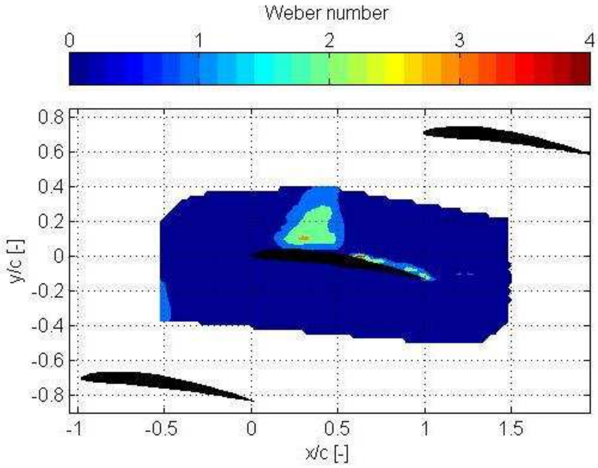

Figure 5: EXPERIMENT: WEBER NUMBER 20-40µm (4)

MODEL TEST: NUMERICAL INVESTIGATION OF A SINGLE AIRFOIL

AVL Fire

Desired applications of a numerical model for droplet breakup in axial compressors include a wide range of possible flow parameters. Especially droplet disintegration will be studied, because this might be important in industrial applications where Ma and Re numbers are higher and the injected droplets are larger than in current tests. The computations utilizing AVL Fire focus on model studies. Hence, a simplified geometry, namely a single compressor profile shaped airfoil, depicted in Figure 6, has been selected. This is suitable for investigating various models for disintegration and atomization.

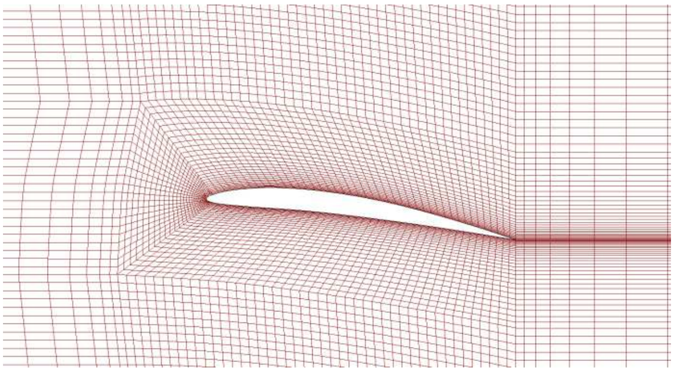

Figure 6: SIMULATION: AREA OF INTEREST

Restrictions in computing capacity for calculations with AVL Fire demanded to restrict the computed area to a flow passage around the blade instead of the entire cascade. The boundary conditions are derived from experimental data.

A full run of a two phase flow simulation consists of three steps:

- calculation of dry flow
- calculation of droplet laden flow without breakup
- calculation of droplet laden flow with breakup

Calculation of the dry flow is necessary to find the proper boundary conditions for the two phase flow. From a calculation of a droplet laden flow with disabled breakup model the distribution of relative velocity between phases is derived. This information is then fed into the simulation including breakup modelling as it is a necessary set of information for the calculation.

For the simulation of the dry flow total pressure at the inlet is adjusted until the velocity distribution matches the experimental data. The resulting Ma number distribution is depicted in Figure 7.

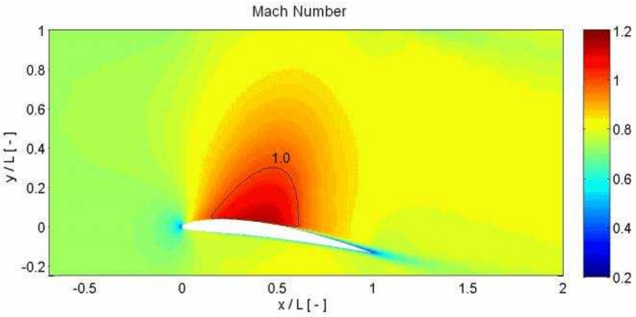

Figure 7: SIMULATION: MACH NUMBER DRY AIR

The incident velocity is uniformly distributed at $237\ m/s$. Flow is accelerated on the suction side of the profile up to transonic velocities. Further downstream a deceleration to $v > 250\ m/s$ can be observed. In contrast to experimental data the velocity at the trailing edge is greater than at the leading edge of the blade, which is abnormal for a compressor application. This difference is the result of an absent staggering angle which is due to the computational boundary conditions as mentioned above. The similarity with regard to the transonic flow regime remains.

AVL Fire delivers the functionality to conduct a simulation of the described kind. An Euler-Lagrangian approach is used. Breakup models like WAVE and TAB are already implemented. The investigation of the breakup models aimed at the clarification whether an adaption to the application at hand is possible.

Droplet Breakup: WAVE Standard Model

The Wave model (6) is based on the stability analysis of a cylindrical slab of water as depicted in Figure 8. It was developed for the modeling of primary jet disintegration and also considers secondary breakup. Only the latter is relevant within this study.

An infinitesimal axially symmetric disturbance is exerted upon the surface. The initial displacement of the magnitude η_0 will grow with a rate of ω. The corresponding wavelength is λ.

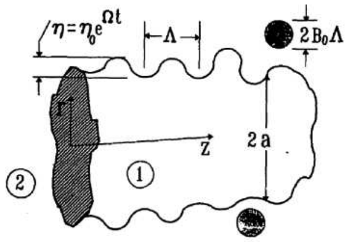

Figure 8: CONCEPT OF WAVE (6)

Let the maximum growth rate $\omega_{\max}=\Omega$ occur with the corresponding wavelength Λ. Wavelength Λ and growth rate Ω then characterize the fastest growing wave on the surface. Calculations are conducted with local fluid properties.

$$\frac{\Lambda}{r}=9.02\frac{(1+0.45\,Oh_{\mathrm{d}}^{\;0.5})(1+0.4\,T^{0.7})}{(1+0.87\,\mathrm{We}_{\mathrm{g}}^{\;1.67})^{0.6}} \tag{2}$$

$$\Omega\left(\frac{\rho_{\mathrm{g}}r^{3}}{\sigma}\right)^{0.5}=\frac{0.34+0.38\,We_{\mathrm{g}}^{\;1.5}}{(1+\,Oh_{\mathrm{d}})(1+1.4\,T^{0.6})} \tag{3}$$

where

$$We_{\mathrm{g}}=\frac{u_{\mathrm{rel}}^{2}r\rho_{\mathrm{g}}}{\sigma}, \tag{4}$$

$$Oh_{\mathrm{d}}=\frac{\eta_{\mathrm{d}}}{\sqrt{\rho_{\mathrm{d}}r\sigma}} \tag{5}$$

and

$$T=Oh_{\mathrm{d}}We_{\mathrm{g}}^{0.5}. \tag{6}$$

Disintegration is then accounted for by the formation of new stable droplets which are sheared off the surface. The radius of the new droplet is r_{stable} and the rate of change in radius of the original droplet is denoted by

$$\frac{dr}{dt}=\frac{-(r-r_{\mathrm{stable}})}{\tau_{\mathrm{a}}} \tag{7}$$

wherein

$$\tau_{\mathrm{a}}=\frac{3.726C_2 r}{\Lambda\Omega} \tag{8}$$

is the duration of the disintegration process. For the investigations conducted here only the secondary breakup is relevant. The size of the secondary droplet is assumed to be proportional to Λ. The radius is then:

$$r_{\mathrm{stable}}=C_1\Lambda \tag{9}$$

The breakup only occurs if $C_1\Lambda\le r$. Duration of breakup process is computed using:

$$t_2=C_2\frac{r}{u_{\mathrm{rel}}}\left(\frac{\rho_{\mathrm{d}}}{\rho_{\mathrm{g}}}\right)^{0.5} \tag{10}$$

Constant C_1 influences the model's behaviour with regard to the predicted size of the secondary droplet (eqn. (9)). By adjusting the value of constant C_2 the duration of disintegration is altered (eqn. (10)). A parameter study has been conducted to indentify the most suitable combination for the problem at hand. The results of the two phase flow simulation using the pressure boundary conditions found in the simulation of the dry flow are depicted in Figure 9.

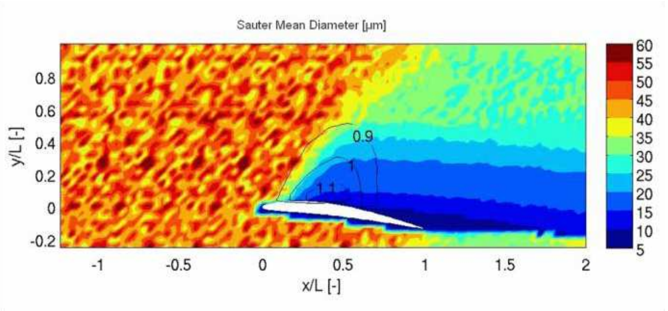

Figure 9: SIMULATION: WAVE RESULTS

The incident flow is characterized by a non uniform SMD-distribution of $D_{32,\mathrm{inc}}=35...60\ \mu\mathrm{m}$ and a regular pattern of high and low values. The boundary conditions are chosen according to the experimental data ($D_{32,\mathrm{inc}}=45\ \mu\mathrm{m}$) and the injection of droplets is done randomly. Other than expected, the SMD is not homogeneous, indicating a not completely random inflow of droplets.

Particle breakup is predicted in the area of transonic flow regime. The relative velocity in this area exceeds stability threshold of $v_{\mathrm{rel}}\le 40\ \mathrm{m/s}$ as derived from the parameter studies. In comparison to experimental data it can be stated that SMD in subsequent flow is generally underestimated. The resulting SMD increases with increasing distance from the blade surface in vertical direction corresponding to the decreasing relative velocity in the same direction as depicted in Figure 10. The number of constants that influence the model's behavior proved to be insufficient to adjust droplet breakup with regard to point in time, duration and secondary droplet size independently.

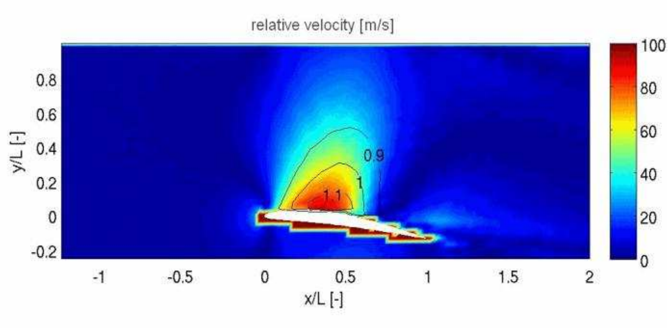

Figure 10: SIMULATION: RELATIVE VELOCITY

Droplet Breakup: Taylor Analogy Breakup Model

An oscillating droplet's movement is analyzed in analogy to the standard spring-damper model as formulated by (7) (Figure 11). The underlying law of movement is formulated:

$$m\ddot{x} = F - kx - d\dot{x}\,. \tag{11}$$

In this application *x* is the excitation of the droplet's equator, as depicted in Figure 12.

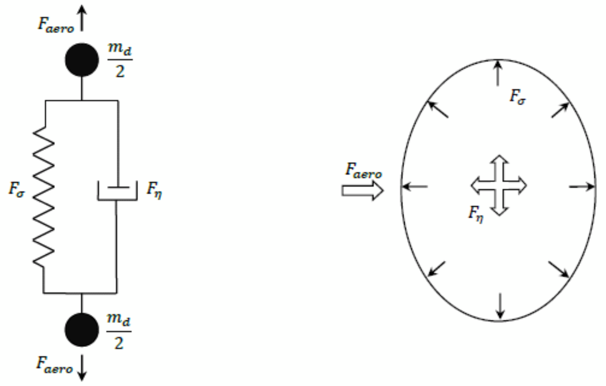

Figure 11: TAB: SPRING MASS ANALOGY (7)

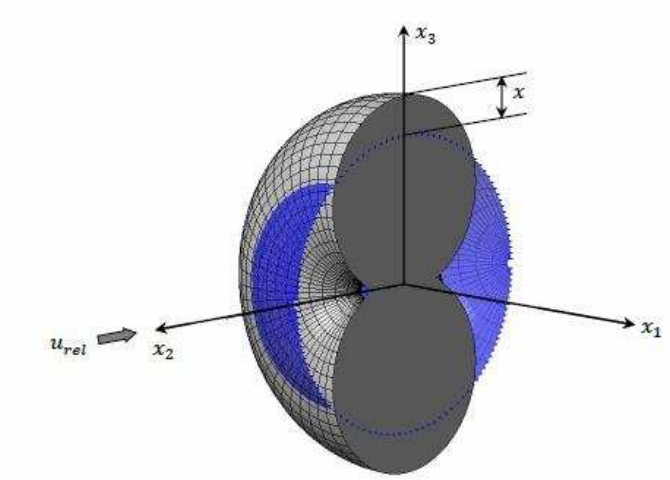

Figure 12: TAB: DROPLET DEFROMATION (7)

It is assumed that breakup occurs if $x > C_b r$. Herein C_b is a dimensionless constant. The dimensionless displacement of the droplet's equator is:

$$y = \frac{x}{C_b r}\,. \tag{12}$$

It is further assumed that the external force is equal to the force exerted by the continuous phase, that the force exerted by the spring is equal to the surface tension and that the damping force is equal to the viscosity of the fluid. Equations and the assumptions above yield:

$$\ddot{y} = \frac{C_F \rho_g u^2}{C_b \rho_d r^2} - \frac{C_k \sigma}{\rho_d r^3} y - \frac{C_d \eta_d}{\rho_d r^2} \dot{y}\,. \tag{13}$$

Constants C_i are determined via mathematical analysis and experimental data. The original droplet oscillates normal to the direction of movement. If $y > 1$ the droplet disintegrates and new droplets are formed. The size of the secondary droplet is determined via the law of energy conservation. The sum of the droplet's energy comprises surface-, oscillation- and deformation energy.

$$E_{\text{original}} = 4\pi r^2 \sigma + \frac{\pi}{5} \rho_d r^5 (\dot{y} + \omega^2 y^2) \tag{14}$$

Herein is *K* the ratio of deformation and oscillation energy to energy in fundamental mode. Secondary droplets are assumed to be spherical and stable. Therefore the total energy of secondary droplets consists of surface and kinetic energies:

$$E_{\text{product}} = 4\pi r^2 \sigma \frac{r}{r_{32}} + \frac{\pi}{6} r^5 \rho_d \dot{y}^2 \tag{15}$$

Equalization yields:

$$\frac{r}{r_{32}} = 1 + \frac{8K}{20} + \frac{\rho_d r^3}{\sigma} \dot{y}^2 \left(\frac{6K - 5}{120} \right) \tag{16}$$

Constant *K* can be adjusted to deliver the desired secondary droplet size.

The model's sensitivity to different values for each factor C_i has been investigated in a parameter study. The results of a simulation utilizing the most suitable combination of constants is depicted in Figure 13

The incident flow shows the same properties as seen in the previous investigation using the WAVE model. Again a non uniform SMD distribution is visible as well as a regular pattern in the incident flow. Values for SMD are again underestimated in comparison to experimental data in the region downstream of the transonic flow regime. Even though the TAB model has a more versatile set of adjustment parameters a strong cross influence between the parameters remains. The influence of the parameters on the different aspects of droplet breakup (point in time, duration and secondary droplet size) proved to be too widespread to achieve a suitable combination. To be able to arbitrarily adapt the breakup properties enhanced modeling is necessary. Therefore a set of parameters that have an isolated influence on each aspect of droplet breakup is desirable.

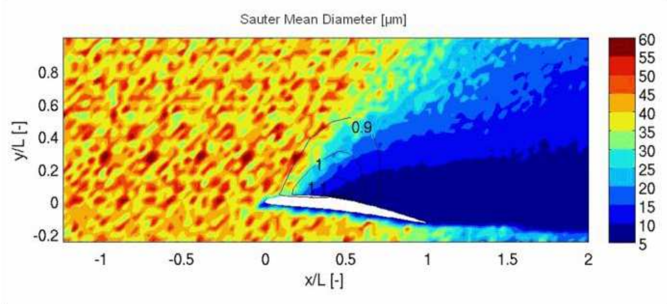

Figure 13: SIMULATION: TAB RESULTS

NUMERICAL INVESTIGATION OF A COMPRESSOR CASCADE

Disperse Phase Flow Code (DPF)

The Disperse Phase Flow (DPF) Code first introduced by (8) is a FORTRAN written source code designed for communication with the ANSYS CFX 13.0 flow solver for numerical simulation of water droplet-laden compressor flows. Utilising an Euler-Lagrange approach the two phases are considered separately. Source terms, as resultant forces of momentum, are determined from droplet motion within the DPF code and considered in the ANSYS flow solver calculations for the continuous phase to obtain a two-way coupling. The successive computation facilitates stability and efficiency, while flexibility is maintained by the independent and expandable routine structure of the FORTRAN Code.

The turbulent continuous phase is calculated by ANSYS CFX 13.0 utilizing a finite volume discretization scheme to solve Reynolds averaged Navier Stokes equations associated with the k-ε turbulence model for closure. Via the ANSYS User Fortran interface the DPF Code initiates the read-out of fluid flow data followed by the successive calculation of droplets' trajectories within the computational mesh. The forces of the carrier flow acting on a particle i.e. drag force F_{CW}, force of gravity F_G, pressure gradient force F_P, virtual mass force F_{VM}, basset force F_B and forces due to domain rotation F_R, deliver the equation of motion:

$$m_d \frac{du_{d,i}}{dt} = F_{CW,i} + F_{G,i} + F_{P,i} + F_{VM,i} + F_{B,i} + \ldots \qquad (17)$$

(i: index for Cartesian coordinate)

For consideration of droplet specific phenomena, disperse phase models for turbulent dispersion, secondary breakup and splashing are implemented within discrete routines as (8) presented.

To model the turbulent dispersion due to turbulent fluctuations of the carrier flow a stochastic method, i.e. the eddy interaction model concept mainly described by (9) is applied by that particle interaction with a succession of fluid phase turbulent eddies is simulated. Turbulent kinetic energy k and the energy dissipation rate ε of the continuous phase are taken for estimation of the current eddy's life time T_e and length scale L_e. Not until the droplet leaves the eddy or the eddy collapses a new eddy is considered. For the duration of particle eddy interaction the fluctuating part of the particle velocity is determined on the basis of a Gaussian distribution with zero mean. Under assumption of isotropic turbulence the variance is directly derived from the definition of turbulent kinetic energy.

A rather droplet specific behaviour is the deformation due to aerodynamic load acting. Depending on flow velocities, fluid properties and particle diameter, the extent of deformation affects its resistance coefficient and hence particle motion but further leads to secondary breakup as a result of exceedingly high deformation. The DPF code accounts for this behaviour by means of the Taylor Analogy Breakup (TAB) model introduced by (7) as described above. To define the critical value of deformation at which secondary breakup occurs an empirical model by (10) is introduced. In dependence of the Weber number and taking nonlinearities of acting forces and deformations at larger deformations into account, following equation with upper boundary of deformation $y_{c,max}$ =2.1 and lower boundary of deformation $y_{c,min}$=1.771 is implemented:

$$\begin{aligned} We \le 13 \quad & y_c = y_{c,min} \\ We > 13 \quad & y_c = y_{c,min} + (y_{c,max} - y_{c,min}) \\ & \cdot \left[1 - \exp\left(-\frac{We - We_c}{2} \right)^{1.2} \right] \end{aligned} \qquad (18)$$

In consequence of droplet breakup secondary droplets are generated by dynamic allocation of memory within the DPF code. The same principle is applied on splashing occurrence.

The simulation model for droplets impinging on dry or wetted surfaces need to imply splashing and deposition mechanisms. The implemented model by (11) applies a criterion for splashing with account to wet surfaces, by use of the film thickness h, and based on the *K* value, which was first introduced by (12).

$$K^2 = \frac{\rho u_{pri}^2 d_{pri}}{\sigma} \frac{1}{\min\left(\dfrac{h}{d_{pri}}, 1\right) + \dfrac{1}{Re_n^{0.5}}} > K_c^2 \qquad (19)$$

For dry surfaces as regarded in the validation calculations the criterion for splashing agrees with the formulation by (12) and the critical *K* value of K_{crit} = 57.7. Further (10) introduced empirically derived correlations for the mass fraction of secondary to primary droplets as well as for secondary droplet diameter and velocities. For estimation of the secondary droplets' diameter, fluctuation velocities and circumferential angle a Nukiyama-Tanasawa distribution function is utilised in addition.

For validation purposes a droplet laden compressor flow according to the experimental investigations has been simulated. The computational quasi-two-dimensional domain contains the three centre blades of the transonic compressor cascade which are embedded within an ANSYS ICEM mesh grid of 114,000 hexahedral cells utilising C-grid structures. Experimental flow conditions are applied by defining the total pressure and total temperature condition at the inlet and a static pressure at the outlet. Regarding the restricted dimensions of the computational domain symmetry conditions are set at the side planes and periodic conditions at the lower and upper boundary as shown in figure 14.

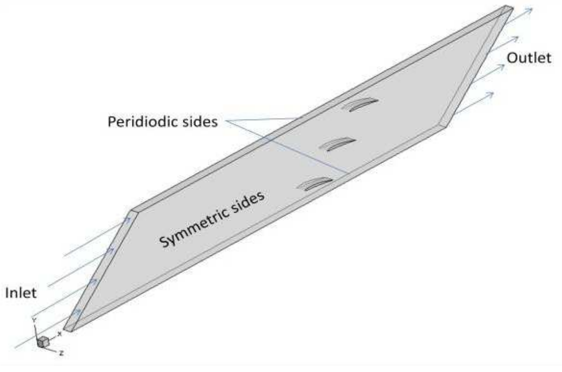

Figure 14: BLADE PASSAGE DOMAIN (13)

First simulations of the dry air compressor flow for evaluation of the continuous phase are opposed to corresponding experimental measurements. Both cases revealed good agreement concerning the transonic regime, with a supersonic flow region on the suction side terminated by a shock inducing flow separation, except a thinner wake region and less boundary layer thickening remained noticeable. More accurate results may be obtained by higher grid resolution or another turbulence model for better boundary layer treatment, but both options are not applicable in connection with the FORTRAN source code, so that minor variations are considered negligible.

For the droplet-laden compressor flow additional boundary conditions concerning the disperse phase are set within the DPF code environment. The experimental measured diameter spectrum is applied for the inlet flow of the droplets with a given water load of 2% of the air mass flow and an approximated number of 50,000 trajectories. The numerical results of both phases are joined using the visualisation software TECPLOT 360 2010.

Corresponding to the experimental results the distribution of the SMD is plotted as depicted in Figure 15.

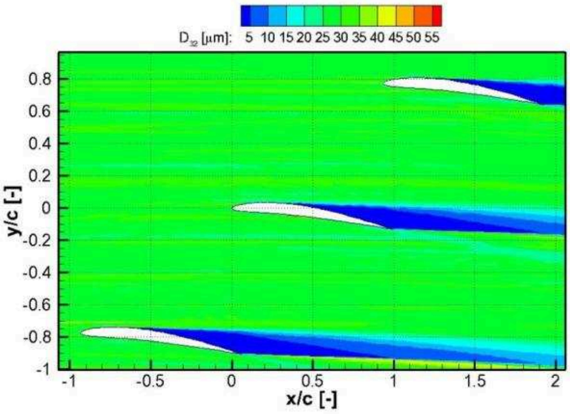

Figure 15: SIMULATION: SMD UTILISING DPF

The numerical computations reveal a homogeneous distribution of the D_{32} diameter on the pressure side as well as on the suction side, but an accumulation of particles with lowest mean diameters in the separation area and wake. Since no evaporation model is implemented droplet size remains constant along the trajectories, except if splashing or secondary breakup occurs. However for the given droplet diameter spectrum secondary breakup is not observed during numerical computations. Hence the droplets of lower diameter accumulated in the separation area and wake result of splashing only.

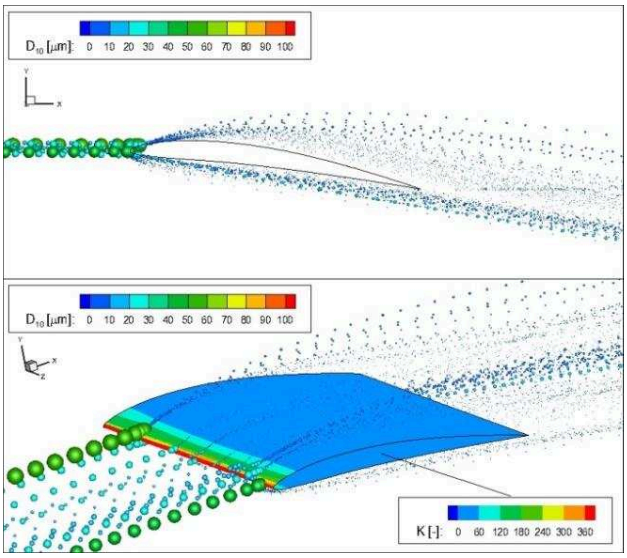

Figure 16: SIMULATION: SPLASHING DROPLETS (13)

Figure 16 depicts the process of several droplets splashing on the leading edge of the blade depending on the present K value. Splashing criterion is met above $K_c = 57.7$ resulting in multiple secondary droplet trajectories. Rebounding secondary droplets follow the airflow according to their inertia and lower particle relaxation time with quick adaptation to the near surface flow of the continuous phase towards the trailing edge.

In consequence the secondary droplets of reduced diameter accumulate in the wake of the blade while the larger primary droplets dominate in the flow to the opposed blade.

In qualitative comparison to the experimental measurements shown in Figure 4, similar results are obtained numerically with a homogeneous pattern of the diameter distribution along the blade's pressure side and accumulation of the lowest droplet diameter in the separation area and wake. The discrepancy within the transonic flow regime at the suction side, revealing measurements of reduced droplet diameter, were declared to be underestimated as described above.

CONCLUSIONS

The investigations conducted dealt with the behaviour of liquid droplets passing a transonic compressor cascade experimentally and numerically. Experiments carried out at the test facility at the Helmut-Schmidt-University in Hamburg, Germany served as the data basis for numerical investigations. The goal of the numerical investigations had two aspects. On the one hand the adjustability of the WAVE and TAB model was tested to assess the flexibility with regard to different aspects of droplet breakup. On the other hand a standalone code (DPF) was tested with regard to its ability to predict the droplet's behaviour in a compressor cascade.

Results show that the main properties of droplet breakup in a simulation, that are breakup location, breakup time as well as the resulting droplet diameters, are adjustable. This is done via the adjustment of the model's parameters. However, it is not possible to adjust them independently from each other, leading to a coupling of the properties.

The combination of ANSYS CFX and the in house developed code DPF was used to simulate a cascade flow in analogy to the experiments conducted. Due to the integration of a splashing model DPF was able to produce results that show a close correlation with the experimental results, as splashing appeared to be the prevalent driver of droplet diameter change in the flow.

Further prospects include the improvement of DPF to reduce the deviations seen and to include phenomena which are not yet accounted for as droplet collision and deformation.

The determination of a critical droplet diameter for secondary breakup needs further determination as well.

ACKNOWLEDGEMENTS

The authors would like to thank the DFG for supporting this project.

NOMENCLATURE

Latin Symbols

C	constant	[-]
d	diameter	[µm]
D	diameter	[µm]
E	energy	[J]
F	force	[N]
K	constant	[-]
l	length	[m]
r	radius	[m]
t	time	[s]
u	velocity	[m/s]
x	displacement	[m]
y	dimensionless displacement	[-]

Dimensionless Numbers

Ma	Mach number	[-]
Oh	Ohnesorge number	[-]
We	Weber number	[-]

Greek Symbols

β	flow angle	[°]
η	dynamic viscosity	[kg/m s]
ρ	density	[kg/cm^3]
σ	surface tension	[N/m]
τ	disintegration time	[s]
ω	growth rate	[1/s]
Λ	wave length	[m]
Ω	growth rate	[1/s]

Indices

0	initial condition
1...n	counter
32	Sauter Mean Diameter
B	Basset force
CW	drag force
d	dispersed (Phase)
e	eddy
g	gaseous (Phase)
G	gravity
inc	incidence
max	maximum
original	original
P	product
pri	primary
product	product
rel	relative
R	rotation
sec	secondary
stable	stable
VM	virtual mass

Abbreviations

CDA	Controlled Diffusion Airfoil
DEHS	Di-Ethyl-Hexyl-Sebacat
DPF	Dispersed Phase Fortran Code
LDA	Laser Doppler Anemometry
PDA	Phase Doppler Anemometry
SMD	Sauter Mean Diameter
TAB	Taylor Analogy Breakup

LITERATURE

1. **Kleinschmidt, R. V.** Value of wet compression in gas-turbine cycles. *Mechanical Engineering.* 1947, Vol. 69, p. 115-116.
2. **Ober, B., Eisfeld, T. and Joos, F.** *Aerodynamische Untersuchungen an Axialverdichtergittern an der Helmut-Schmidt-Universität Hamburg.* Hamburg : DGLR Jahrestagung 2010 Hamburg, 2010. 1302.
3. **Ferziger, J.H. and Peric, M.** *Computational Methods for Fluid Dynamics.* Berlin, Heidelberg, New York : Springer, 2002. ISBN 978-3-540-67586-0.
4. **Eisfeld, T. and Joos, F.** *Experimental Investigation of Two-Phase Flow Phenomena in Transonic Compressor Cascades.* Orlando, USA : ASME Turbo Expo 2009, 2009. GT2009-59365.
5. **Schmelz, F.** *Tropfenzerfall in beschleunigten Gasströmungen.* Aachen, Germany : Shaker, 2002. ISBN 978-3-540-71865-9.
6. **Reitz, R. D.** Modeling Atomization Processes in High-Pressure Vaporizing Sprays. *Atomisation and Spray Technology.* 1987, Vol. 3, p. 309-337.
7. **O'Rourke, P. J. and Amsden, A. A.** *The Tab Method for Numerical Calculation of Spray Droplet Breakup.* Toronto : Society of Automotive Engineers, 1987. SAE 872089.
8. **Matysiak, A.** *Euler-Lagrange Verfahren zur Simulation tropfenbeladener Strömung in einem Verdichtergitter* . s.l. : Universität der Bundeswehr Hamburg, 2007. Dissertation.
9. **Gosman, A.D. and Ioannides, E.** *Aspects of Computer Simulation of Liquid-Fueled Combustors.* Vol. 7, No. 6 : J.Energy, 1983. 4852-490.
10. **Schmehl, R.** *Tropfendeformation und Nachzerfall bei der technischen Gemischaufbereitung.* Berlin : Logos, 2004. ISBN 978-3-8325-0707-7.
11. **O'Rourke, P.J. and Amsden, A.A.** *A Spray/Wall Interaction Submodel for the KIVA-3 Wall Film Model.* Detroit, USA : Society of Automotive Engineers, 2000. SAE2000-01-0271.
12. **Mundo, C.** *Zur Sekundärzerstäubung newtonscher Fluide an Oberflächen, Ph.D. Thesis.* Erlangen-Nürnberg : University Erlangen-Nürnberg, 1996.
13. **Storm, D. and Joos, F.** *Euler-Lagrange Method for Numerical Simulation of Water Droplet-Laden Compressor Flows.* Stockholm : ISABE, 2011. 2011-1254 - Accepted Paper.
14. **Eisfeld, T. and Joos, F.** *New boundary layer treatment methods for compressor cascades.* Graz, Austria : s.n., 2009. ETC8 - B250.

DIPSI Workshop 2011 on Droplet Impact Phenomena & Spray Investigation
May 27, 2011, Bergamo, Italy

NEW APPROACHES TO MODELLING DROPLET HEATING AND EVAPORATION

S.S. Sazhin*, I.G. Gusev*, J.-F. Xie*, A.E. Elwardany*, A.Yu. Snegirev°, M.R. Heikal*[1]

*Sir Harry Ricardo Laboratories, School of Computing, Engineering and Mathematics,
University of Brighton, Brighton BN2 4GJ, U.K.
°Saint-Petersburg State Polytechnic University, Polytechnicheskaya, 29, Saint-Petersburg 195251, Russia.
[1]Current address: Department of Mechanical Engineering, Universiti of Teknologies PETRONAS, Bandar Sri Iskandar 31750 Tronoh, Perak Darul Ridzuan, Malaysia

ABSTRACT

New solutions to the droplet heat conduction equation, assuming that the droplet radius is a linear function of time, are described alongside new solutions to the same equation, assuming that the time evolution of droplet radius $R_d(t)$ is known. For sufficiently small time steps the time evolutions of droplet surface temperatures and radii, predicted by both approaches for typical Diesel engine-like conditions, coincide. Both solutions predict lower droplet temperatures and slower evaporation when the effects of the reduction of $R_d(t)$ due to evaporation are taken into account. A simplified model for multi-component droplet heating and evaporation, based on an analytical solution to the species diffusion equation, is discussed. This model has been generalised to take into account the effect of coupling between the droplets and the surrounding gas. A new approach to modelling multi-component droplets, including large numbers of components, heating and evaporation is discussed. This new approach is based on the replacement of a large number of actual components with a small number of quasi-components. The evaporation and condensation of n-dodecane ($C_{12}H_{26}$) are investigated using the molecular dynamics (MD) simulation technique. The values of the evaporation/condensation coefficient are estimated.

INTRODUCTION

In most commercial and research computational fluid dynamics (CFD) codes the modelling of droplet heating and evaporation is based on the assumptions that: there is no temperature gradient inside droplets; the droplet radius is fixed during each time step, although it changes from one time step to another; kinetic effects can be ignored; and in the case of multi-component droplets, the species diffusivity within the droplet is infinitely large or small [1].

The aim of this paper is to summarise some of the most recent developments in the modelling of droplet heating and evaporation processes, in which the above mentioned commonly used assumptions are relaxed. For mono-component droplets, these models take into account the effect of finite thermal conductivity and recirculation in the moving droplets, alongside the change in droplet radius during individual time steps [2,3]. For multi-component droplets, including relatively small numbers of components, the new models are based on the analytical solution of the species diffusion equation inside the droplet [4,5]. The model designed to take into account large numbers of components is based on the introduction of the concept of quasi-components [6]. A new approach to calculating the evaporation coefficient of n-dodecane, the closest approximation to Diesel fuel, is described based on [7]. This coefficient is essential for the accurate kinetic modelling of droplet evaporation.

The paper will start with an overview of results referring to hydrodynamic models of mono-component droplets, after which the modelling of multi-component droplets with small and large numbers of components is discussed. Then the focus moves to kinetic modelling with particular emphasis on calculation of the evaporation/condensation coefficient. Finally the conclusions of the paper are drawn.

MONO-COMPONENT DROPLETS: HYDRODYNAMIC MODELS

Assuming that droplet heating is spherically symmetric, the transient heat conduction equation inside droplets can be written as [1]:

$$\frac{\partial T}{\partial t} = \frac{\kappa}{R^2}\frac{\partial}{\partial R}\left(R^2\frac{\partial T}{\partial R}\right) + P(t,R), \qquad (1)$$

where $\kappa = k_l/(c_l\ \rho_l)$ is the liquid thermal diffusivity, k_l, c_l, and ρ_l are the liquid thermal conductivity, specific heat capacity, and density, respectively, R is the distance from the centre of the spherical droplet, t is time. The boundary and initial conditions for this equation, ignoring the effect of evaporation, can be presented as:

$$h(T_g - T_s) = k_l\frac{\partial T}{\partial R}\Big|_{R=R_d}, \qquad (2)$$

$$T(t=0) = T_{d0}(R), \qquad (3)$$

where $T_s = T_s(t)$ is the droplet's surface temperature, $T_g = T_g(t)$ is the ambient gas temperature, $h = h\ (t)$ is the convective heat transfer coefficient, linked with the Nusselt number Nu via the equation $\mathrm{Nu} = 2R_d h/k_g$, k_g is the gas thermal conductivity. To take into account the effect of evaporation the gas temperature T_g is replaced by the so-called effective temperature T_{eff} [1]:

$$T_{eff} = T_g + \rho_l L\frac{dR_d}{dt}/h, \qquad (4)$$

where L is the latent heat of evaporation and $\frac{dR_d}{dt}$ is the rate of change of droplet radius due to evaporation.

In the case when the convection heat transfer coefficient h (t) = h = const, the solution to the transient heat conduction equation (1), with R_d = const and the corresponding boundary (2) and initial (3) conditions, can be presented as [1]:

$$T = T_{eff} + \frac{R_d}{R} \sum_{n=1}^{\infty} \left\{ \left[q_n - \frac{\sin\lambda_n \ \mu_0(0)}{\lambda_n^2 \| V_n \|^2} \right] \exp(-\kappa_0 \lambda_n^2 \ t) \right.$$

$$\left. - \frac{\sin\lambda_n}{\lambda_n^2 \| V_n \|^2} \int_0^1 \frac{d\mu_0(\tau)}{d\tau} \exp\left[-\kappa_0 \lambda_n^2 (t-\tau) \right] d\tau \right\} \sin\left(\frac{\lambda_n R}{R_d} \right)$$

$$+ \frac{R_d}{R} \sum_{n=1}^{\infty} \frac{p_n}{\kappa_0 \lambda_n^2} [\ 1 - \exp(-\kappa_0 \lambda_n^2 t)] \sin\left(\frac{\lambda_n R}{R_d} \right) . \qquad (5)$$

A set of positive eigenvalues λ_n, numbered in ascending order (n=1, 2, . . .) (the trivial solution $\lambda = 0$ is not considered), is found from the solution of the following equation:

$$\lambda_n \cos\lambda_n + h_0 \sin\lambda_n = 0 \, , \qquad (6)$$

$$h_0 = \frac{h r_d}{k_l} - 1, \ \| V_n \|^2 = 0.5(1 - \sin 2\lambda_n / 2\lambda_n) \, ,$$

$$V_n = \sin(\lambda_n R / R_d) \, ,$$

$$\kappa_0 = k_l / (c_l \rho_l R_d^2) \, ,$$

$$p_n = \frac{1}{\| V_n \|^2} \int_0^1 \left[\frac{R P(t,R)}{R_d} \right] V_n(R) d(R/R_d) \, .$$

The generalisation of the above model to the case of moving droplets (Effective Thermal Conductivity (ETC) model) can be achieved by replacing the thermal conductivity of liquid k_l with the effective thermal conductivity $k_{\mathrm{eff}} = \chi \ k_l$, where the coefficient χ varies from about 1 (at droplet Peclet numbers <10) to 2.72 (at droplet Peclet numbers >500). The variations of all parameters with temperature and time were accounted for when analytical solution (4) was incorporated into a numerical code.

This model was applied to the modelling of droplet heating and evaporation, assuming that droplet radius remains constant during the time step. Assuming that the Lewes number is equal to 1, the change of the droplet radius from one time step to another was described by the following equation [2]:

$$\frac{dR_d}{dt} = -\frac{k_g \ \mathrm{Sh}}{2 \rho_l c_{pg} R_d} \, , \qquad (7)$$

where k_g is the gas thermal conductivity, c_{pg} is the gas specific heat capacity at constant pressure, Sh is the Sherwood number. When solving Equation (7) it was assumed that the temperature remained the same during the time step.

Solution (5) has been generalised to the case when droplet radius was assumed to be a linear function during the time step [2] or an arbitrary function $R_d(t)$ [3]. In the latter case, the solution turned out to be the simplest when the initial droplet temperature is assumed to be constant. Since $R_d(t)$ depends on the time evolution of the droplet temperature, an iterative process is required. Firstly, the time evolution of $R_d(t)$ is obtained using the conventional approach, when it remains constant during the time step, but changes from one time step to another. Then these values of $R_d(t)$ are used in the new solutions to obtain updated values of the time evolution of the distribution of temperatures inside the droplet and on its surface. These new values of droplet temperature are used to update the function $R_d(t)$. This process continues until convergence is achieved, which typically takes place after about 15 iterations. The results of these calculations were compared with the results obtained using the approach when the droplet radius was assumed to be a linear function of time during individual time steps for typical Diesel engine-like conditions. For sufficiently small time steps the time evolutions of droplet temperatures and radii predicted by both approaches coincided. This suggests that both approaches are correct and valid. Similarly to the case when droplet radius is assumed to be a linear function of time during the time step, the solutions for arbitrary $R_d(t)$ predict lower droplet temperature and slower evaporation when the effects of the reduction of $R_d(t)$ are taken into account. It is shown that in the case of constant droplet initial temperature, models both taking and not taking into account the changes in the initial droplet temperature with the distance from the droplet centre predict the same results. This indicates that both models are correct. The correctness of this approach is further supported by agreement between the results obtained in [2] and those reported in [8]. In the latter paper the analysis is based on the direct numerical solution to Equation (1), taking into account the effect of the moving boundary.

MULTI-COMPONENT DROPLETS: HYDRODYNAMIC MODELS

For modelling multi-component droplet heating and evaporation, the same equations as used for mono-component droplets are applied, but these are complemented by the equations for species mass fractions $\left(Y_{li} \equiv Y_{li}(t,R)\right)$ inside the droplets [1]:

$$\frac{\partial Y_{li}}{\partial t} = D_l \left(\frac{\partial^2 Y_{li}}{\partial R^2} + \frac{2}{R} \frac{\partial Y_{li}}{\partial R} \right), \qquad (8)$$

where $i > 1$, D_l is the liquid mass diffusivity. Equation (8) is solved subject to the boundary condition [1]:

$$\alpha(\epsilon_i - Y_{lis}) = -D_l \frac{\partial Y_{li}}{\partial R}\bigg|_{R=R_d-0}, \qquad (9)$$

and the initial condition $Y_{li}(t=0) = Y_{li0}(R)$, where $Y_{lis} = Y_{lis}(t)$ are liquid components' mass fractions at the droplet's surface,

$$\alpha = \frac{|\dot{m}_d|}{4\pi\rho_l R_d^2}, \qquad (10)$$

$\epsilon_i = Y_{vis}/\sum_i Y_{vis}$ are species evaporation rates. The effect of recirculation in the moving droplets is taken into account by replacing D_l with $D_{eff} = \chi_Y D_l$, where χ_Y is determined by Equation (18) of [4]. This model is known as the Effective Diffusivity (ED) model.

In contrast to the previously used models, our approach is based on the analytical solution of Equation (8) subject to the above mentioned boundary and initial conditions [4,5]:

$$Y_{li} = \epsilon_i + \frac{1}{R}\left\{\left[\exp\left[D_l\left(\frac{\lambda_0}{R_d}\right)^2 t\right][q_{i0} - \epsilon_i(0)Q_0] - Q_0\int_0^t \frac{d\epsilon_i(\tau)}{d\tau}\exp\left[D_l\left(\frac{\lambda_0}{R_d}\right)^2 (t-\tau)\right]d\tau\right]\sinh\left(\lambda_0\frac{R}{R_d}\right) + \sum_{n=1}^{\infty}\left[\exp\left[-D_l\left(\frac{\lambda_n}{R_d}\right)^2 t\right][q_{in} - \epsilon_i(0)Q_n] - Q_n\int_0^t \frac{\mathrm{d}\epsilon_i(\tau)}{\mathrm{d}\tau}\exp\left[-D_l\left(\frac{\lambda_n}{R_d}\right)^2 (t-\tau)\right]d\tau\right]\sin\left(\lambda_n\frac{R}{R_d}\right)\right\}, \qquad (11)$$

where λ_0 is the non-zero solution of equation $\tanh\lambda = -\lambda/h_{0Y}$, λ_n are the solutions of Equation (6), with h_0 being replaced with h_{0Y},

$$Q_n = \begin{cases} -\frac{1}{\|v_0\|^2}\left(\frac{R_d}{\lambda_0}\right)^2 (1+h_{0Y})\sinh\lambda_0 & \text{when } n=0 \\ \frac{1}{\|v_n\|^2}\left(\frac{R_d}{\lambda_n}\right)^2 (1+h_{0Y})\sin\lambda_n & \text{when } n\geq 1 \end{cases}$$

$$\|v_n\|^2 = \begin{cases} \frac{R_d}{2}\left[1+\frac{\mathrm{h}_{0\mathrm{Y}}}{h_{0Y}^2-\lambda_0^2}\right] & \text{when } n=0 \\ \frac{R_d}{2}\left[1+\frac{\mathrm{h}_{0\mathrm{Y}}}{h_{0Y}^2-\lambda_n^2}\right] & \text{when } n\geq 1 \end{cases},$$

$$q_{in} = \begin{cases} \frac{1}{\|v_0\|^2}\int_0^{R_d} RY_{li0}(R)\sinh\left(\lambda_0\frac{R}{R_d}\right)\mathrm{d}R & \text{when } n=0 \\ \frac{1}{\|v_n\|^2}\int_0^{R_d} RY_{li0}(R)\sin\left(\lambda_n\frac{R}{R_d}\right)\mathrm{d}R & \text{when } n\geq 1 \end{cases}$$

$$h_{0Y} = -\left(1+\frac{\alpha R_d}{\mathrm{D}_l}\right).$$

The molar fractions of species i in the vapour phase at the droplet surface are determined as:

$$X_{vi} = X_{li}\gamma_i \exp\left[\frac{L_i M_i}{R_u}\left(\frac{1}{T_{bi}} - \frac{1}{T_s}\right)\right], \qquad (12)$$

where X_{li} are the liquid molar fractions at the surface of the droplet, γ_i are the activity coefficients. L_i, M_i and T_{bi} are the latent heat of evaporation, molar masses and boiling temperatures of species i, R_u is the universal gas constant, T_s is the droplet surface temperature. The activity coefficient for the ethanol/acetone mixture has been estimated following [9]. In the limit, when $\gamma_i = 1$ the Raoult law is valid.

The above model has been generalised to take into account the effects of the moving boundaries on the solution to Equation (8) and tested against available experimental data (see [4,5] for details). Two new solutions to the equation, describing the diffusion of species during multi-component droplet evaporation, are described. The first solution is the explicit analytical solution to this equation, while the second one reduces the solution of the differential transient species equation to the solution of the Volterra integral equation of the second kind. Both solutions take into account the effect of the reduction of the droplet radius due to evaporation, assuming that this radius is a linear function of time. These solutions can be considered as the generalisations of the solutions reported earlier. The analytical solution is presented in the case when parameter h_{Y0} can be assumed to be a constant, the value of which is less than -1 during the time step. These solutions are complementary to the ones suggested earlier, which took into account the effect of the moving boundary due to droplet evaporation on the distribution of temperature inside the droplet. The analytical solution has been incorporated into a zero dimensional CFD code and applied to the analysis of bi-component droplet heating and evaporation. The case of an initial 50% ethanol - 50% acetone mixture and droplets with initial diameter equal to 142.7 µm, as in our earlier paper [4], has been considered. Effects of droplets on gas have been ignored at this stage and droplet velocity has been assumed to be constant and equal to 12.71 m/s. To separate the effect of the moving boundary on the species diffusion equation from similar effects on the heat conduction equation inside droplets, described in [4,5], a rather artificial assumption that the droplet temperature is homogeneous and fixed has been made. The moving boundary slows down the increase in the mass fraction of ethanol (the less volatile substance in the mixture) during the evaporation process and accelerates droplet evaporation.

The original simplified model (not taking into account the effects of the moving boundary) has been generalised to take into account the effect of coupling between the droplets and the surrounding gas [5]. The new model has been validated against the observed average droplet temperatures in a monodisperse spray for various n-decane/3-pentanone droplet mixtures. It is concluded that the effect of coupling leads to noticeably better agreement with the experimental results than the results of the one-way solution. The simplified bi-component model has also been implemented into the FLUENT CFD code. Both the stand-alone zero-dimensional code and FLUENT CFD code predict identical results in identical cases, when the effects of droplets on gas are ignored and gas in the enclosure is assumed to be homogeneous. This opens the way for using the customised version of the FLUENT code, incorporating the new model of bi-component droplet heating and evaporation, for the analysis of realistic cases referring to inhomogeneous enclosures, taking into account the effects of droplets on gas.

The main limitation of this model is that it is able to take into account a rather limited number of components, while realistic fuels usually include a very large number of these components. An alternative model, suggested in [6] is based on replacing the large number of actual components with a small number of quasi-components. These quasi-components are then treated as actual components in the model described earlier, taking into account the diffusion of quasi-components in droplets. The model has been applied to Diesel fuel droplets which have been approximated as a mixture of 21 actual components C_nH_{2n+2}, where $n \geq 5$. These 21 actual components have been replaced by up to 20 quasi-components (the maximal number of quasi-components in this model).

The initial mole fraction of each quasi-component is calculated as:

$$X_j = \int_{n_{j-1}}^{n_j} f_m(n)\mathrm{d}n, \tag{13}$$

where j is an integer in the range $1 \leq j \leq N_f$, N_f is the number of quasi-components, $n_0 \leq n \leq n_f$ and $f_m(n)$ is the distribution function approximated as:

$$f_m(n) = C_m\left(n_0, n_f\right) \frac{(M(n)-\gamma)^{\alpha-1}}{\beta^{\alpha}\Gamma(\alpha)} \exp\left[-\left(\frac{M(n)-\gamma}{\beta}\right)\right], \tag{14}$$

where $M(n) = 14n + 2$ are the molecular weights, $n_0 = 5$, $n_f = 25$, $\Gamma(\alpha)$ is the Gamma function, α and β are parameters that determine the shape of the distribution and γ determines the original shift. We assume that $\alpha = 18.5$, $\beta = 10$ and $\gamma = 0$. The constant $C_m\left(n_0, n_f\right)$ is defined as [6]:

$$C_m\left(n_0, n_f\right) = \left\{\int_{n_0}^{n_f} \frac{(M(n)-\gamma)^{\alpha-1}}{\beta^{\alpha}\Gamma(\alpha)} \exp\left[-\left(\frac{M(n)-\gamma}{\beta}\right)\right] \mathrm{d}n\right\}^{-1}. \tag{15}$$

Each quasi-component has a number of carbon atoms estimated as [6]:

$$\bar{n}_j = \frac{\int_{n_{j-1}}^{n_j} n f_m(n)\mathrm{d}n}{\int_{n_{j-1}}^{n_j} f_m(n)\mathrm{d}n}. \tag{16}$$

The latent heat and saturation pressure for each quasi-component have been calculated by replacing n with $\bar{n}_j$. Other thermo-physical properties have been assumed to be the same as those for n-dodecane. The latent heat and saturation pressure for each quasi-component have been assumed to be relatively weak functions of n.

This model has been applied to the analysis of heating and evaporation of droplets with initial radius 25 µm, initial temperature 300 K and constant velocity 1 m/s. The gas temperature and pressure have been assumed to be constant and equal to 880 K and 3 MPa respectively. The evaporation time predicted by the ETC/ED models using 20 quasi-components has been shown to be longer than in the case of 1 quasi-component. This can be attributed to the fact that at the final stages of droplet evaporation the heaviest species (large number of carbon atoms) become the dominant. They evaporate more slowly than more volatile species (small number of carbon atoms). Also they have higher wet bulb temperatures. There are also noticeable differences between the surface temperatures and radii predicted by the ETC/ED and ITC/ID models. Higher droplet surface temperatures, predicted by the ETC/ED model, compared with the ITC/ID model, are expected to affect the physical ignition delay of the autoignition of the fuel vapour [1].

MONO-COMPONENT DROPLETS: KINETIC MODELS

The limitation of the hydrodynamic models described above, even in the case of evaporation at high pressures, has been discussed in a number of papers, including [9-13]. In these papers the evaporation of n-dodecane (the nearest approximation to Diesel fuel) has been considered and a new model for the analysis of droplet heating and evaporation has been developed based on the combination of the kinetic and hydrodynamic approaches. In the immediate vicinity of droplet surfaces (up to about one hundred molecular mean free paths), the vapour and ambient gas dynamics have been studied based on the Boltzmann equation (kinetic region), while at larger distances the analysis has been based on the hydrodynamic equations (hydrodynamic region). Mass, momentum and energy fluxes have been conserved at the interface between these regions.

The predictions of this model have been shown to be as accurate as those of the model based on the kinetic equations in the whole domain, but both differed considerably (up to 10%) from the predictions of the hydrodynamic models for Diesel engine-like conditions. The practical application of this combined or kinetic modelling, however, requires the specification of some special boundary conditions at the droplet surface and at the interface between the kinetic and hydrodynamic regions. The kinetic boundary condition at the interface between vapour and its condensed phase has been presented as [10]:

$$f^{out} = \sigma f^e + (1-\sigma) f^r \quad (v_x > 0), (17)$$

where $f^{out}$is the overall distribution function of molecules leaving the interface from the liquid phase, σ is the evaporation coefficient, f^e is the distribution function of molecules in the saturated vapour at the liquid surface temperature, f^r is the distribution function of reflected molecules and v_x is the velocity component normal to the interface. In the equilibrium state the evaporation and condensation coefficients are equal. They will be referred to as the evaporation/condensation coefficient. In the above mentioned papers [9-13], it has been implicitly or explicitly assumed that the distribution function f^e is isotropic Maxwellian. The values of the evaporation/condensation coefficients have been assumed equal to 0.04 and 0.5 (the minimal and average value of this parameter of water) [9] or 1 [10-13]. None of these assumptions have been rigorously justified. The only practical way to perform this justification would be to base it on the molecular dynamic simulation at the interface region.

Most of the previous studies have applied the molecular dynamic approach to the analysis of the evaporation and condensation processing of monatomic or relatively simple polyatomic molecules, such as argon, water or methanol [14-18]. In our previous study [7], molecular dynamics simulations have been performed to study the evaporation and condensation of n-dodecane ($C_{12}H_{26}$) at liquid-vapour phase equilibria using the modified OPLS (Optimized Potential for Liquid Simulation) model. The interface thickness in equilibrium state has been predicted to be 1.2-2.0 nm. It has been shown that the molecular chains lie preferentially parallel to the interface in the liquid-vapour transition region. The predicted evaporation/condensation coefficient decreased from about 0.9 to about 0.3 when temperature increased from 400 K to 600 K. Typical molecular behaviours in the evaporation and condensation processes have also been presented and discussed.

Although this result still needs to be confirmed based on simulations including much larger numbers of molecules, it opens the way for a much more rigorous approach to the kinetic modelling of droplet heating and evaporation compared with the approaches used so far.

CONCLUSIONS

New solutions to the heat conduction equation, describing transient heating of an evaporating droplet, are described following [2]. These solutions take into account the effect of the reduction of the droplet radius due to evaporation, assuming that this radius is a linear function of time. The latter assumption does not allow us to apply these solutions to describe the whole process, from the start of evaporation, until the moment in time when the droplet completely evaporates. However, these solutions are expected to be used to describe droplet heating and evaporation over a small time step when other parameters, except droplet radius and temperature, can be assumed constant. In this case they can be considered as generalisations of the approach currently used in all research and commercial computational fluid dynamics (CFD) codes known to us, in which it is assumed that droplet radius is constant during the time step.

New solutions to the heat conduction equation described in [3] are summarised, involving transient heating of an evaporating droplet and assuming that the time evolution of it's radius $R_d(t)$ is known. Since $R_d(t)$ depends on the time evolution of the droplet temperature, an iterative process is required. The results of the calculations of droplet surface temperature, using this approach, are compared with the results obtained using the approach when the droplet radius is assumed to be a linear function of time during individual time steps for typical Diesel engine-like conditions. For sufficiently small time steps the time evolutions of droplet surface temperatures and radii predicted by both approaches coincide. Similarly to the case when droplet radius is assumed to be a linear function of time during the time step, the new solution predicts lower droplet temperatures and slower evaporation when the effects of the reduction of $R_d(t)$ are taken into account.

A simplified model for multi-component droplet heating and evaporation is discussed. Apart from the finite thermal conductivity of droplets and recirculation inside them, this model takes into account species diffusion inside droplets, based on the analytical solution to the species diffusion equation. The model has been implemented into a stand-alone zero-dimensional code and validated against the observed droplet temperatures in a monodisperse spray for various ethanol/acetone droplet mixtures. This simplified model has been generalised to take into account the effect of coupling between the droplets and the surrounding gas. A new approach to modelling multi-component droplets, including large numbers of components, heating and evaporation is discussed. This new approach is based on the replacement of a large number of actual components with a small number of quasi-components. It takes into account the effect of finite thermal and mass diffusion inside the droplet using the ETC/ED and ITC/ID models.

Two new solutions to the equation, describing the diffusion of species during multi-component droplet evaporation, are described. The first solution is the explicit analytical solution to this equation, while the second one reduces the solution of the differential transient species equation to the solution of the Volterra integral equation of the second kind. Both solutions take into account the effect of the reduction of the droplet radius due to evaporation, assuming that this radius is a linear function of time. These solutions can be considered as the generalisations of the solutions reported earlier.

The evaporation and condensation of n-dodecane ($C_{12}H_{26}$), the closest approximation to Diesel fuel, have been investigated using the molecular dynamics (MD) simulation technique. Some preliminary results of this investigation are presented. The thickness of the transition layer between liquid and vapour phases at equilibrium is estimated to be 1.2-2.0 nm. It has been pointed out that the molecules at the liquid surface need to gain relatively large translational energy to evaporate. Vapour molecules with high translational energy can easily penetrate deep into the transition layer and condense in the liquid phase. The values of the evaporation/condensation coefficient at various liquid phase temperatures have been estimated.

ACKNOWLEDGMENT

The authors are grateful to the European Regional Development Fund Franco-British INTERREG IVA (Project C5, Reference 4005), EPSRC (grant EP/H001603/1), the Royal Society (UK) (Project JP090548) and RFBR Russia (grant 10-08-92602-KO_a) for the financial support of this project.

NOMENCLATURE

Symbol	Quantity	SI Unit
c	specific heat capacity	$J\cdot kg^{-1}\cdot K^{-1}$
C_m	constant introduced by Equation (15)	
D	diffusion coefficient	$m^2\cdot s^{-1}$
f_m	distribution function	
h	heat transfer coefficient	$W\cdot m^{-2}\cdot K^{-1}$
h_0	parameter introduced in Equation (6)	
h_{0Y}	parameter introduced in Equation (11)	
k	thermal conductivity	$W\cdot m^{-1}\cdot K^{-1}$
L	latent heat of evaporation	$J\cdot kg^{-1}$
m	mass	kg
M	molar mass	$kg\cdot kmole^{-1}$
n	number of carbon atoms	
N_f	number of quasi-components	
Nu	Nusselt number	
Pe	Peclet number	
p_n	parameter introduced in Equation (5)	
q_{in}	parameter introduced in Equation (11)	
q_n	parameter introduced in Equation (5)	
Q_n	parameter introduced in Equation (11)	
R	distance from the droplet centre	m
R_d	droplet radius	m
Sh	Sherwood number	
t	time	s
T	temperature	K
V_n	eigen function	
X	molar fraction	
Y	mass fraction	
α	parameter introduced by Equation (10) or constant introduced in Equation (14)	
β	constant introduced in Equation (14)	
γ	activity coefficient or constant introduced in Equation (14)	
ε_i	species evaporation rate	
κ	diffusivity	$m^2\cdot s^{-1}$
κ_0	parameter introduced in Equation (5)	
λ	eigenvalues	
μ	dynamic viscosity	Pa.s
$\mu_0(t)$	parameter introduced in Equation (5)	
ρ	density	$kg\cdot m^{-3}$

Subscripts

b	boiling
d	droplet
eff	effective
f	final
g	gas
i	species
l	liquid
p	constant pressure
s	surface
v	vapour
0	initial

REFERENCES

[1] S.S. Sazhin, Advanced models of fuel droplet heating and evaporation, *Progress in Energy and Combustion Science*, vol. 32, pp. 162-214, 2006.

[2] S.S. Sazhin, P.A. Krutitskii, I.G. Gusev, M.R. Heikal, Transient heating of an evaporating droplet, *Int J Heat and Mass Transfer*, vol. 53, pp. 2826-2836, 2010.

[3] S.S. Sazhin, P.A. Krutitskii, I.G. Gusev, M.R. Heikal, Transient heating of an evaporating droplet with presumed time evolution of its

radius, *Int. J of Heat and Mass Transfer*, vol. 54(5-6), pp. 1278-1288, 2011.

[4] S.S. Sazhin, A. Elwardany, P.A. Krutitskii, G. Castanet, F. Lemoine, E.M. Sazhina M.R. Heikal, A simplified model for bi-component droplet heating and evaporation, *Int. J of Heat and Mass Transfer*, vol. 53(21-22), pp. 4495-4505, 2010.

[5] S.S. Sazhin, A. Elwardany, P.A. Krutitskii, V. Depredurand, G. Castanet, F. Lemoine, E.M. Sazhina, M.R. Heikal, Multi-component droplet heating and evaporation: numerical simulation versus experimental data, *Int. J of Thermal Science*, vol. 50, pp. 1164-1180, 2011.

[6] S.S. Sazhin, A. Elwardany, E.M. Sazhina, M.R. Heikal, A quasi-discrete model for heating and evaporation of complex multicomponent hydrocarbon fuel droplets, *Int. J of Heat and Mass Transfer*, vol. 54, pp. 4325-4332, 2011 .

[7] B.Y. Cao, J.-F. Xie, S.S. Sazhin, Molecular dynamics study on evaporation and condensation of n-dodecane at liquid-vapour phase equilibria, *J Chemical Physics*, vol. 134, 164309 2011.

[8] S.L. Mitchell, M. Vynnycky, I.G. Gusev, S.S. Sazhin, An accurate numerical solution for the transient heating of an evaporating spherical droplet, *Applied Mathematics and Computation*, vol. 217, pp. 9219-9233, 2011.

[9] A.P. Kryukov, V.Y. Levashov, S.S. Sazhin, Evaporation of diesel fuel droplets: kinetic versus hydrodynamic models, *Int. J. Heat Mass Transfer*, vol. 47, pp. 2541-2549, 2004.

[10] I.N. Shishkova, S.S. Sazhin, A numerical algorithm of kinetic modelling of evaporation processes, *J. Comput. Phys.*, vol. 218, pp. 635-653, 2006.

[11] S.S. Sazhin, I.N. Shishkova, A.P. Kryukov, V.Yu. Levashov, M.R. Heikal, Evaporation of droplets into a background gas: kinetic modelling, *Int. J. Heat Mass Transfer*, vol. 50, pp. 2675-2691, 2007

[12] S.S. Sazhin, I.N. Shishkova, A kinetic algorithm for modelling the droplet evaporation process in the presence of heat flux and background gas, *Atomization Sprays*, vol. 19, pp. 473-489, 2009.

[13] S.S. Sazhin, I.N. Shishkova, M. Heikal, Kinetic modelling of fuel droplet heating and evaporation: calculations and approximations, *International J. of Engineering System Modelling and Simulation*, vol. 2, pp. 169-176, 2010.

[14] T. Tsuruta, H. Tanaka, T. Masuoka, Condensation/evaporation coefficient and velocity distributions at liquid-vapour interface, *Int. J. Mass Heat Transfer*, vol. 42, pp. 4107-4116, 1999.

[15] G. Nagayama, T. Tsuruta, A general expression for the condensation coefficient based on transition state theory and molecular dynamics simulation, *J. Chem. Phys.*, vol. 118, pp. 1392-1399, 2003.

[16] T. Tsuruta, G. Nagayama, Molecular dynamics studies on the condensation coefficient of water, *J. Phys. Chem. B*, vol. 108, pp. 1736-1743, 2004.

[17] T. Ishiyama, T. Yano, S. Fujikawa, Molecular dynamics study of kinetic boundary conditions at an interface between argon and its condensed phase, *Phys. Fluids*, vol. 16, pp. 2899-2906, 2004.

[18] T. Ishiyama, T. Yano, S. Fujikawa, Molecular dynamics study of kinetic boundary conditions at an interface between a polyatomic vapor and its condensed phase, *Phys. Fluids*, vol. 16, pp. 4713-4726, 2004.

DIPSI Workshop 2011 on Droplet Impact Phenomena & Spray Investigation
May 27, 2011, Bergamo, Italy

COMBUSTION OF DIESEL SPRAY: LOW- AND HIGH-TEMPERATURE OXIDATION PROCESSES FOR FREE DIESEL INJECTION AND IN POROUS REACTORS

M. Weclas and J. Cypris

Georg-Simon-Ohm- University of Applied Sciences Nuremberg
Faculty of Mechanical Engineering, Institute of Vehicle Technology
Keßlerplatz 12, 90489 Nürnberg, Germany

ABSTRACT

Heat release process in a free volume combustion chamber and in porous reactors has been analyzed in a wide range of initial pressures and temperatures under Diesel engine-like conditions. For investigating of this kind of reactions a special combustion chamber characterized by a constant volume and adiabatic conditions has been used as an engine simulator.

Diesel spray combustion is a very complex multi-step process. The physics of spray formation, penetration and mixture formation must be considered together with chemistry of low- and high-temperature oxidation.

The resulting pressure history in both porous reactors and in free volume significantly depends on the initial pressure and temperature. At lower initial temperatures the process in porous reactors is accelerated. There are five characteristic regions of the process characterized by different delay time, reaction rate and number of recognizable oxidation reactions. Combustion in porous reactor is characterized by heat accumulation in solid phase of porous structure and results in reduced pressure peaks and lowered combustion temperature. This depends on reactor heat capacity, pore density, specific surface area, pore structure and heat transport. Low- and high-temperature oxidation processes of Diesel sprays as performed in porous reactors are similar in nature to those in free volume combustion chamber.

INTRODUCTION

Future internal combustion engine requires a clean homogenous combustion process. Such a process would result in simultaneous heat release characterized by a homogeneous temperature field in the combustion chamber. There are number of challenges in realizing of homogeneous combustion process in engine operating under variable load and speed conditions. Especially critical are: control of ignition timing, combustion duration, heat release rate and corresponding pressure gradient and pressure peak, control of combustion temperature for nearly zero-NO_x-emissions, completeness of the process for low CO and HC emissions. There is no system known to the authors that can satisfy all conditions selected above, at least if variable load conditions are considered. Two of them are of special attention: control of ignition timing and lowering of combustion temperature below thermal NOx-level. A novel kind of engine with combustion process in highly porous three-dimensional reactors that could satisfy above selected conditions has been proposed by Durst and Weclas [1,2].This engine concept has great potential for high cycle efficiency and for a nearly-zero emissions level allowing combustion temperature control due to heat accumulation in reactor. During the time between fuel injection begins and the rapid pressure increase corresponding to the high-temperature heat release process (ignition delay) a number of complex chemical and physical processes must be performed. Physics of the process must consider fuel supply process (injection), spray distribution in space, spray atomization, fuel vaporization and mixing with air. These processes are of high complexity in the case of Diesel engine-like conditions where the resulting mixture is highly non-homogeneous and time-space dependent. For future engines requiring clean combustion process (overall called as homogeneous combustion processes) the chemistry of the pre-ignition processes as well as controlled auto ignition are the key factors for process control under variable engine loads and rates. The low-temperature oxidation is usually treated as a two-stage process: cool- and blue flames are followed by a high temperature oxidation (depending on the initial temperature and pressure as well as on mixture composition). Additionally, development of high-temperature open cell and highly porous structures for application to internal combustion engines is necessary for development of this kind of combustion systems [3]. These processes can be divided into two groups: direct fuel injection into porous reactor (Diesel jet interaction with porous structure) and low- and high-temperature oxidation in the reactor. Thermal ignition and high-temperature oxidation (heat release) complete the investigated process [4-11]. There are almost no experimental data available in the literature on these processes. The paper describes selected aspects of these complex phenomena as performed in a free volume combustion chamber and in porous reactors under engine-like conditions. Heat release process in porous reactors having different structures and heat capacities is discussed in comparison to Diesel-like process (free volume combustion). In both cases a direct fuel injection using a common-rail diesel injection system into combustion chamber (free volume as well as porous reactor) is used.

DIESEL SPRAY INTERACTION WITH POROUS STRUCTURE

Diesel jet may be considered as a free jet propagating in space outwards of the nozzle exit characterized by narrow angle, high penetration velocity, large penetration length and to some extend by atomization. For jet interaction with porous structure there is almost no information available in the literature describing this complex phenomenon. Mostly for modelling, the spray interaction with porous structure is substituted by mono-disperse droplets homogeneously distributed in the porous structure, e.g. see [12]. For combustion of a liquid fuels, the interaction between the fuel spray and a porous medium (PM) is very complex [13]. These authors say that this process could not be observed and measured with conventional experimental methods because the complexity of porous structure does not allow optical access into it. They suggested that numerical simulation offers the only way to perform the analysis. Contrary to that, the present authors [4-9] presented experimental data allowing first insight into the process of Diesel spray interaction with a three-dimensional porous structure. If free jet interacts with porous structure there are some characteristic phases of the process to be described in [5]. In a free space between nozzle outlet and porous structure the jet develops having diesel spray properties. The injection pressure defines the jet properties, especially propagation and then impingement velocity. Jet impingement process onto inner surface of the porous structure depends on a number of parameters, especially on spray properties and degree of its development. Jet penetrating into porous structure interacts with wall junctions and a wide radial spreading of the impinging jet with reduced penetration velocity occurs in PM volume according to a multi-jet splitting [4-8] - fig.1. If the porous structure is hot a superposition of fuel distribution (multi-jet splitting) and fuel vaporization is observed – fig.2.

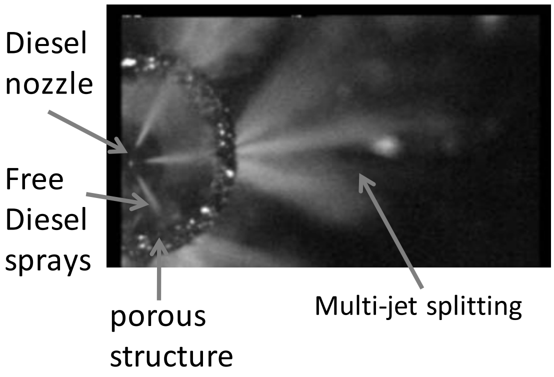

Figure 1: Multi-jet splitting by diesel jet interaction with porous structure

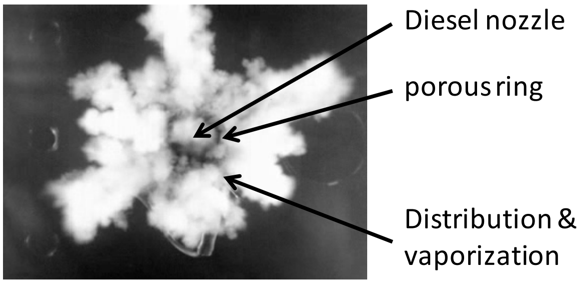

Figure 2: Diesel jet interaction with hot porous ring (T_{PM}=300°C)

SIMULATION OF ENGINE CONDITIONS FOR DIESEL SPRAY COMBUSTION IN FREE VOLUME AND IN POROUS REACTOR

Durst and Weclas [1,2] have proposed engine concept with mixture formation and combustion in a porous reactor. Application of a porous combustion reactor allows realization of homogeneous and flameless combustion process characterized by a near-zero emissions level. Heat recuperation in porous reactor may increase the engine-cycle efficiency resulting in reduction of CO_2 emissions. Heat accumulation in porous reactor results in significantly lowered combustion temperature permitting near-zero NO_x level. This is the essential difference between the combustion process in conventional Diesel engine and in engine with combustion in PM (see fig.3 and 4). One of possible realization of real engine with combustion in porous reactor requires that the fuel must directly be injected into combustion reactor. This in consequence requires that the fuel must be distributed throughout the reactor volume together with vaporization and mixing with air. The hot reactor is used as a three-dimensional igniter and the heat release process must be performed in the reactor volume. The fuel should be injected in a short period of time close to the TDC of compression stroke. The reactor temperature (temperature of solid phase of the reactor and temperature of the gas trapped inside reactor volume) and homogeneity of mixture inside the reactor define the conditions for thermal ignition and following heat release process. This is because the reactor heat capacity and large specific surface area for inter-phase heat transfer inside the reactor volume change the thermodynamic conditions of the process [14].

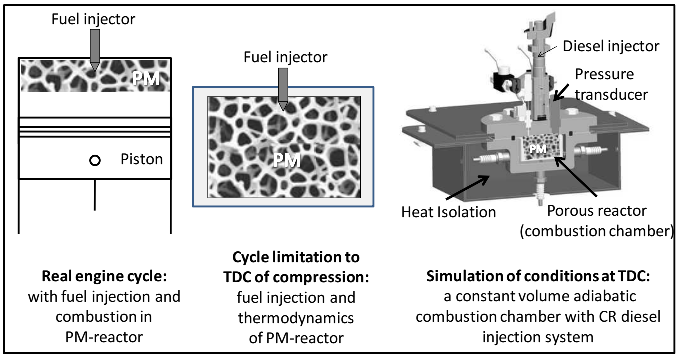

Figure 3: Simulation of real engine conditions in a special combustion chamber

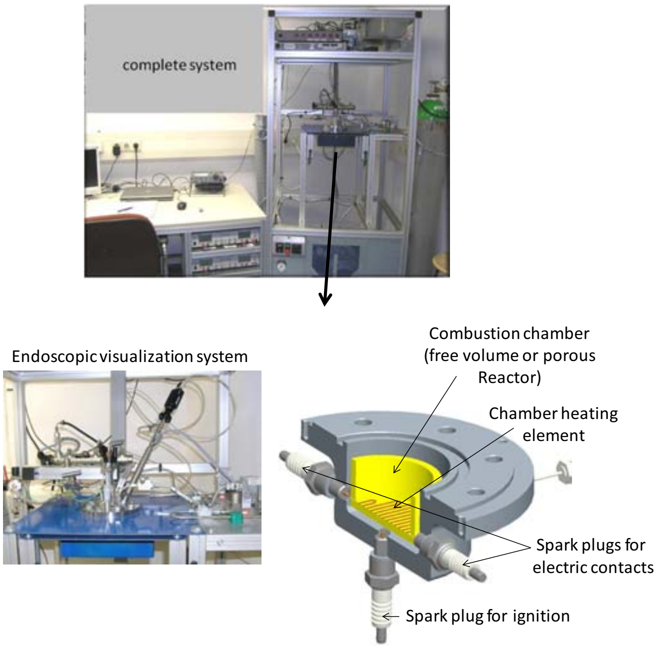

Figure 4: View of the combustion chamber

The whole process is analysed from time instance "zero" defined by the start of injection ("IB"). The procedure for setting of initial temperature T_{IB}=T_{PM} and initial pressure p_{IB} in the combustion chamber is shown in fig.5.

In a first step a given mass of synthetic dry air at certain pressure p_1 is supplied to the chamber. After closing the system the air is trapped in chamber (or porous reactor) which is electrically heated up to required temperature T_{IB} corresponding to the porous reactor temperature T_{PM}. This also results in increasing chamber pressure achieving p_{IB}.

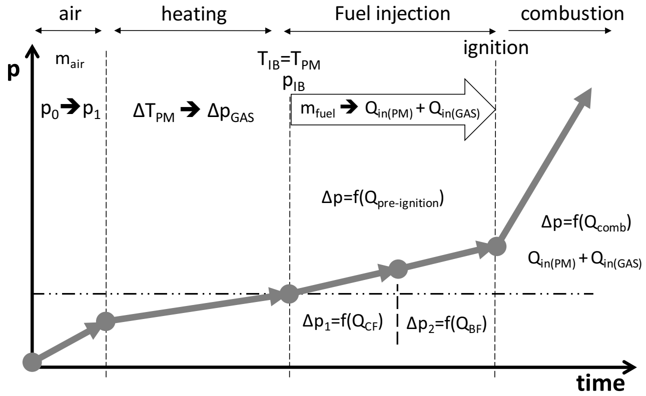

Figure 5: Measurement routing

Characteristic time *t* (delay time) of a particular process is analysed and measured starting at zero-time point (point IB)- see Fig.6. For analysis of the reaction rate a slope *sl* of the reaction curve corresponding to the particular oxidation process is described by average pressure changes in time [bar/ms].

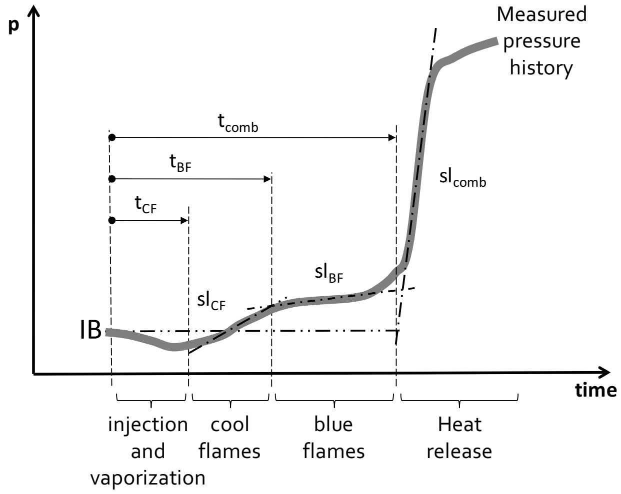

Figure 6: Definition of measured parameters on the pressure history

OVERALL CHARACTERISTICS OF SPRAY COMBUSTION IN A FREE VOLUME UNDER DIESEL ENGINE-LIKE CONDITIONS

On the basis of performed investigations in a wide range of initial pressures and temperatures it is possible to construct fields representing characteristic combustion modes. These fields consider three kinds of parameters characterizing low- and high-temperature oxidation processes: characteristic reaction behavior represented by a single- or a multi-step oxidation, reaction rate and characteristic delay time. The data plotted have quantitative form, and only the shape of border lines among different combustion modes should be interpreted more qualitatively – see fig.7. On the left hand side of this figure characteristic modes are presented in p_{IB}-T_{IB} diagram. On the right hand side examples of pressure history in an initial part of the heat release process are plotted. There are five characteristic modes of the process that have been selected:

Mode 1: Process at low initial pressures p_{IB} in a wide range of initial temperatures T_{IB} characterized by very long delay time (~20ms), very low reaction rate (<1bar/ms), and three slopes are recognizable.

Mode 2: Process at low initial temperatures T_{IB} in a wide range of initial pressures p_{IB} characterized by very long delay time (>20ms), very low reaction rate (<1bar/ms), and a single slope is recognizable.

Mode 3: Process at middle initial pressures p_{IB} and higher initial temperatures T_{IB} characterized by shorter delay time (<10ms), middle reaction rate (~5bar/ms), and three slopes are recognizable.

Mode 4: Process at middle initial temperatures T_{IB} and at higher initial pressures p_{IB} characterized by shorter delay time (<10ms), middle reaction rate (<10bar/ms), and two slopes are recognizable.

Mode 5: Process at high initial pressures p_{IB} and high initial temperatures T_{IB} characterized by short delay time (<2ms), high reaction rate (>20bar/ms), and two slopes are recognizable.

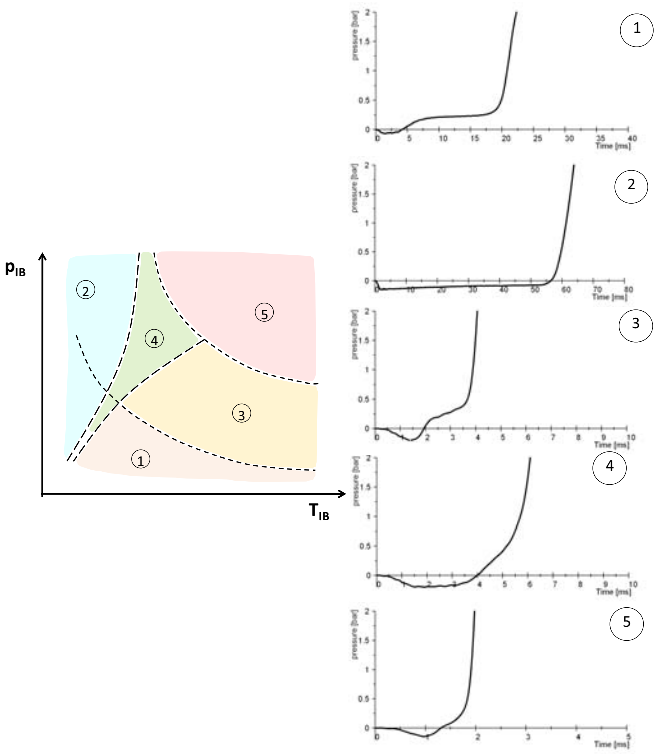

Figure 7: Characteristic modes of heat release process

In the range of low initial temperatures, mostly corresponding to cool flame reactions, a characteristic dependence of the delay time on the chamber pressure has been observed, as shown in fig.8. In a given range of pressures the delay time is the shortest and the corresponding reaction rates are the highest. This effect, in analogy to NTC (negative temperature coefficient), the authors have defined as a positive pressure coefficient PPC [11].

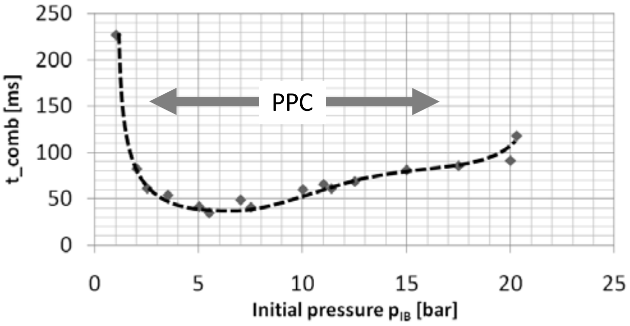

Figure 8: Range of positive pressure coefficient

An example of delay time distribution of characteristic reactions (top) as well as of reactions rate (bottom) is presented in fig.9. The data are plotted at constant air excess ratio (λ=1.5).

SPRAY COMBUSTION IN POROUS REACTORS UNDER DIESEL ENGINE-LIKE CONDITIONS

Application of highly porous three dimensional open cell structures to engines as well as to a combustion chamber significantly changes the conditions of mixture formation and combustion as compared to free volume combustion chamber:

- Large heat capacity of PM reactor (energy accumulation)
- Quite different conditions for spray development and its distribution in reactor volume
- Very effective and quick heat transport inside reactor
- Large specific surface area of PM reactor
- PM temperature dominates in the thermodynamics of the process (not gas temperature).

There are two types of reactor that have been considered: “ideal” porous reactor (IR) in which at any instant of time the gas temperature is equal to porous reactor temperature; “real” porous reactor (RR) in which at any instant of time after fuel injection starts the gas temperature is not equal to porous reactor temperature.

The thermodynamic analysis of the process in a free volume combustion chamber (FV) and in both considered porous reactors (IR and RR) allow formulating the following relations:

- Pressure change after fuel injection starts:

$$\Delta p_{G(FV)} > \Delta p_{G(RR)} >> \Delta p_{G(IR)}$$

- Temperature change of gas after fuel injection starts:

$$\Delta T_{G(FV)} > \Delta T_{G(RR)} >> \Delta T_{G(IR)}$$

The gas temperature change in a real reactor is a function of reactor temperature and can be expressed as [14]:

$$\Delta T_{G(RR)} = \Delta T_{G(FV)} - \left(K \cdot \Delta T_{PM}\right)$$

where K is the factor characterizing reactor heat capacity and heat transfer conditions between gas and reactor solid phase.

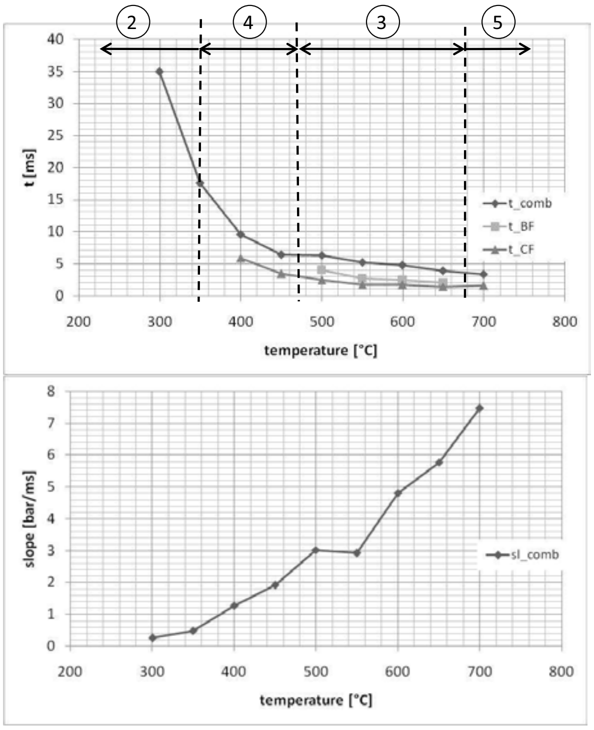

Figure 9: Distribution of delay times (top) and reaction rates (bottom) as a function of initial chamber temperature for a constant λ=1.5

An example of heat release process in a porous reactor made of SiC foam structure (8ppi pore density) as compared to free volume combustion is shown in figure 10. Top diagram shows a pressure history as measured after start of fuel injection and the bottom picture shows the pressure gradients representing the heat release rate. The process in porous reactor is faster (delay time is shorter and the reaction rate is higher) and the resulting maximum pressure is lowered owing to the large heat capacity of the reactor. Pressure history corresponding to the heat release process as performed in a porous reactor has a similar character as observed for combustion in a free volume chamber.

The energy accumulated in the porous reactor lowers the combustion temperature keeping the reaction rate high. This temperature depends significantly on heat capacity of the combustion reactor. In figure 11 the heat release process in two SiC foam reactors having significantly different pore density (8ppi and 30ppi) is shown for different initial reactor temperatures.

Generally, the heat release process is more delayed with increasing pore density, i.e. with decreasing pore size (foam structures). This effect is more visible at lower reactor temperatures. Also distribution of reaction rate indicates similar behaviour. The pressure peak level is pore density dependent and decreases with increasing pore density. This is mainly due to the heat capacity of reactor and heat transfer inside porous structure. The initial reactor temperature does not change this behaviour.

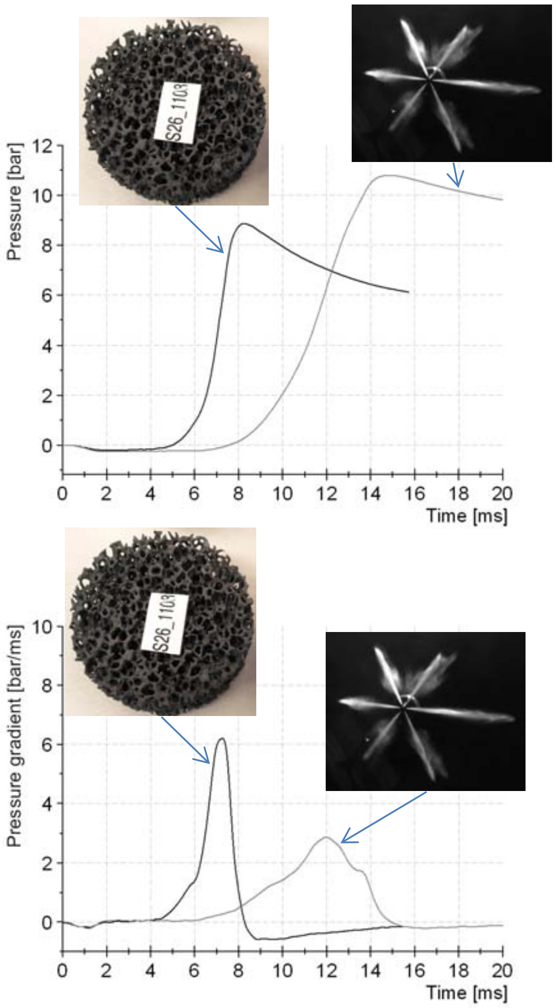

Figure 10: Heat release process in porous reactor (SiC foam structure, 8ppi) as compared to free volume process at p_{IB}=18bar and T_{IB}=400°C

The amount of heat accumulated in the porous reactor influences the maximum combustion temperature (real reactor conditions are considered). As shown in figure 12 the maximum combustion temperature for free volume combustion and for two different SiC foam reactors (8ppi and 30ppi) gradually increases with increasing initial temperature, and is significantly reduced in value for combustion reactors. This reduced temperature is a result of heat accumulation in a porous reactor and the maximum temperature reduces with increasing reactor heat capacity, pore density and specific surface area.

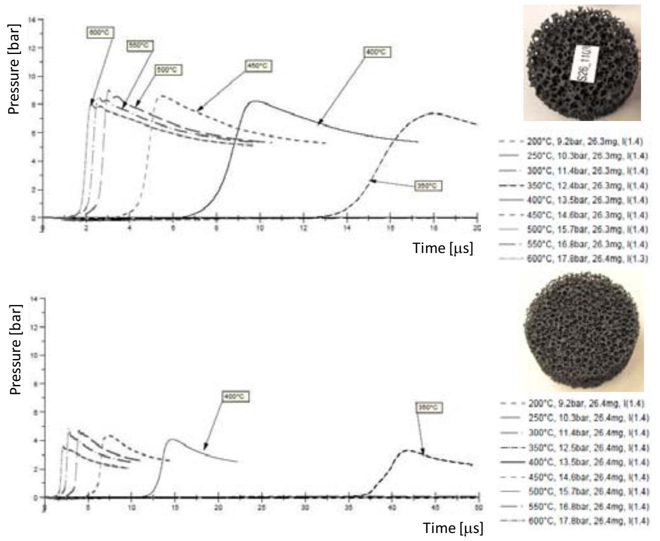

Figure 11: Comparison of pressure histories for heat release in different porous reactors after fuel injection starts at constant air access ratio λ (initial pressure, initial temperatures and mass of injected fuel are not constant)

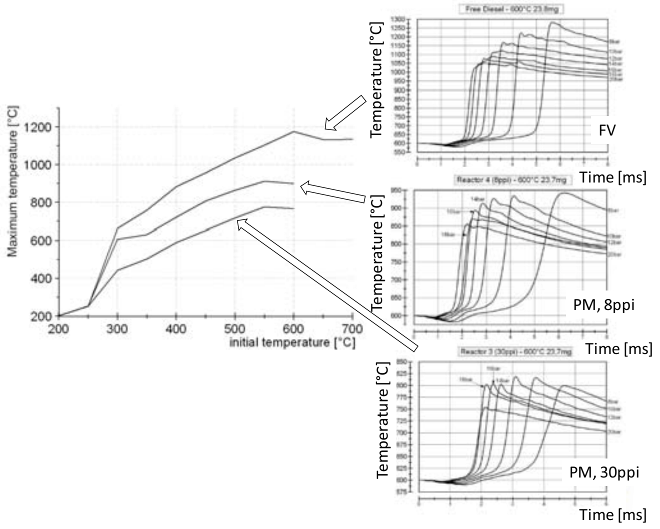

Figure 12: Distribution of maximum combustion temperature (left) versus initial temperature in free volume system and in two porous reactors (8ppi and 30ppi) for mass of injected fuel 23.8mg and a constant air excess ratio.

Characteristic features of heat release process can be constructed in two-dimensional fields representing characteristic combustion modes in porous reactors as compared to free Diesel injection conditions. There are two kinds of parameters to be considered: characteristic reaction behavior represented by a single- or a multi-step oxidation (fig.13) and distribution of characteristic delay time (fig.14). All these data are plotted in a two-dimensional field of initial chamber pressure and temperature. The data have been grouped according to pre-selected criteria, such as number of slopes in reaction curve and duration of delay time. The data plotted have quantitative character, and only the shape of border lines among different combustion modes should be interpreted more qualitatively. The shape of border lines depends on the reactor heat capacity, pore density and pore structure.

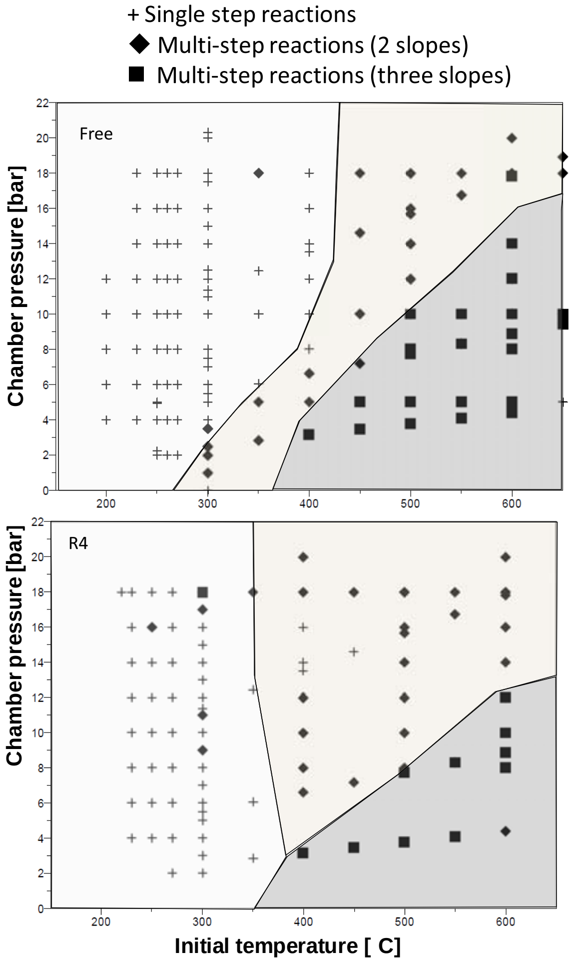

Figure 13: Fields representing characteristic combustion modes in SiC foam (8ppi) porous reactor as compared to free Diesel injection conditions

There are three characteristic regions selected in fig.13 representing three different characteristic modes of the oxidation process:

Region 1 is characterized by single-step reactions and is located at lower initial temperatures for all initial pressures.

Region 2 is characterized by multi-step reactions with two slopes recognizable in the reaction curve and is located in the range of middle-high initial temperatures at middle-high initial pressures.

Region 3 is characterized by multi-step reactions with three slopes recognizable in the reaction curve and is located in the range of higher initial temperatures at low-middle initial pressures.

In the case of reaction delay time the following regions are selected in fig.14:

Region A is characterized by delay times t > 20ms and is located at lower initial temperatures at all investigated initial pressures.

Region B is characterized by delay times 10ms < t ≤ 20ms and is located at higher initial temperatures and lower initial pressures as well as in a small region of high initial pressures.

Region C is characterized by delay times 5ms < t ≤ 10ms and is located at higher initial temperatures and lower-middle initial pressures as well as in a small region of high initial pressures.

Region D is characterized by delay times 2ms < t ≤ 5ms and is located at higher initial temperatures and middle to high initial pressures.

Region E is characterized by delay times t ≤ 2ms and is located at high initial temperatures and high initial pressures.

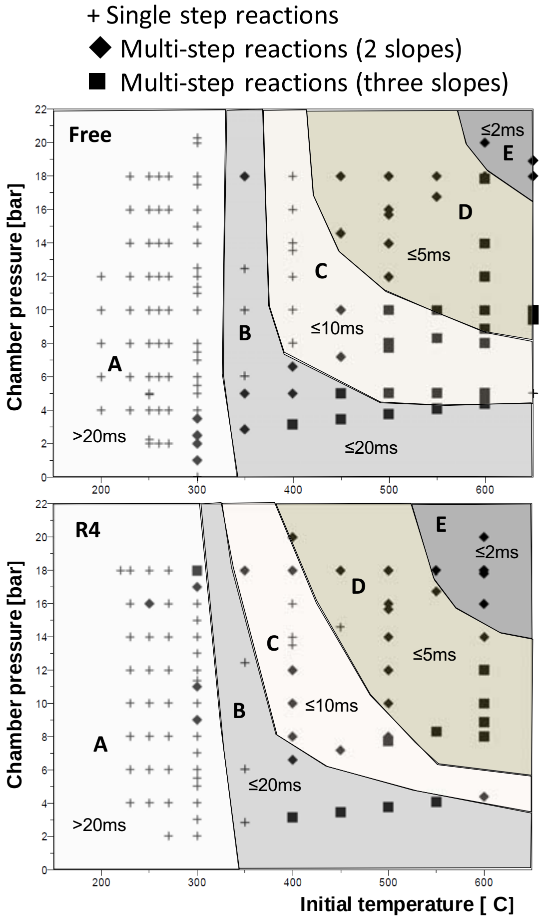

Figure 14: Fields representing characteristic combustion modes and delay times in SiC foam (8ppi) porous reactor as compared to free Diesel injection conditions

Analysis of characteristic regions selected in figures 13 and 14 indicates qualitative similarity of heat release process as performed under Diesel-like conditions and in porous reactor. A quantitative influence of porous reactor features (reactor heat capacity, pore density, pore structure, specific surface area and fuel distribution in reactor volume) is clearly visible. This qualitative similarity of processes as performed in a free volume and in porous reactors indicates high probability for applicability of the concept with clean combustion in porous reactor to internal engine conditions. Quantitative influence of reactor conditions described by reactor heat capacity, pore density, pore structure, specific surface area, fuel distribution in reactor volume and heat transport indicates a large potential for system optimization for application to internal combustion engines.

CONCLUDING REMARKS

1. Diesel spray combustion is a very complex multi-step process. The physics of spray formation, penetration and mixture formation must be considered together with chemistry of low- and high-temperature oxidation.
2. For investigating of this kind of reactions a special combustion chamber characterized by a constant volume and adiabatic conditions has been used as an engine simulator.
3. Positive Pressure Coefficient (PPC) indicates range of pressures p_{IB} where delay time of pre-ignition reactions is the shortest and the rate of these reactions is the highest (mostly corresponding to cool-flame reactions and transition to blue-flames).
4. Ignition delay time reduces with increasing chamber temperature and pressure: slow reactions are characterized by delay time of many tens to hundreds of milliseconds; fast reactions are characterized by delay time being less than one millisecond at high temperatures and high pressures.
5. Low- and high-temperature oxidation of Diesel sprays are significantly temperature and pressure dependent. There are five characteristic regions of the process characterized by different delay time, reaction rate and number of recognizable oxidation reactions.
6. Low- and high-temperature oxidation processes of Diesel sprays as performed in porous reactors are in nature similar to those in a free volume combustion chamber.
7. There are three main differences in the process conditions at similar thermodynamic conditions:
   - large heat capacity of the reactor influencing pressure peak level (heat supplied to the reactor)
   - large specific surface area of the reactor influencing heat transfer inside reactor volume
   - porous structure (pore size, density and structure) influencing the process of Diesel injection and fuel distribution in space as well as fuel vaporization and mixing with air.

REFERENCES

[1] Durst, F., Weclas, M., A new type of internal combustion engine based on the porous-medium combustion technique, J. Automobile Engineering, I.Mech.E., part D, Vol. 215, 2001, 63-81.

[2] Durst, F., Weclas, M., A New Concept of I.C. Engine with Homogeneous Combustion in Porous Medium (PM), 5th International Symposium on Diagnostics and Modeling of Combustion in Internal Combustion Engines, COMODIA, 2001, Nagoya, Japan.

[3] Schlier, L., Zhang, W., Travitzky, N., Cypris, J., Weclas, M., and Greil, P., Macro-cellular silicon carbide reactors for a non-stationary combustion under piston engine-like conditions, Int. Journal of Applied Ceramic Technology, (2010) DOI:10.1111/j.1744-7402.2010.02591

[4] Weclas, M., High velocity CR Diesel jet impingement onto porous structure and its utilization for mixture homogenization in I.C. engines, DITICE Workshop: Drop/wall interaction: Industrial applications, Experiments and Modeling, May 2006, Bergamo, Italy.

[5] Weclas, M., Some fundamental observations on the Diesel jet “destruction” and spatial distribution in highly porous structures, Journal of Porous Media, vol. 11, iss.2, 2008, 125-145.

[6] Weclas, M., Homogenization of liquid distribution in space by Diesel jet interaction with porous structures and small obstacles, 22nd European Conference on Liquid Atomization and Spray Systems, Como (Italy), September 2008, Paper no. ID ILASS08-A003,

[7] Weclas, M., Cypris, J., “Distribution-nozzle” concept: a method for Diesel spray distribution in space for charge homogenization by late injection strategy, ILASS – Europe 2010, 23rd Annual Conference on Liquid Atomization and Spray Systems, Brno, Czech Republic, September 2010, Paper no.ID ILASS10-39

[8] Weclas, M., Faltermeier, R. Diesel jet impingement on small cylindrical obstacles formixture homogenization by late injection strategy, Int. Journal of Engine Research, vol.8, Nr.5 2007, pp.399-413.

[9] Weclas, M. Potential of porous media combustion technology as applied to internal combustion engines, Journal of Thermodynamics, Volume 2010, Article ID 789262, 39 pages, doi:10.1155/2010/789262

[10] Weclas, M., 2005, Porous media in internal combustion engines, [in:] Cellular Ceramics-Structure, Manufacturing, Properties and Applications, Scheffler, M. , Colombo, P. (eds), Wiley-VCH-Publ. (May, 2005)

[11] Weclas, M., Cypris, J., Maksoud, T.M.A., Combustion of Diesel sprays under real-engine like conditions: analysis of low- and high-temperature oxidation processes, ILASS – Europe 2010, 23rd Annual Conference on Liquid Atomization and Spray Systems, Brno, Czech Republic, September 2010, Paper no.ID ILASS10-40

[12] Liu, H., Xie, M., Wu, D., Simulation of a porous medium (PM) engine using a two-zone combustion model, Applied Thermal Engineering 29 (2009) 3189–3197

[13] M. Abdul Mujeebu, M. Zulkifly Abdullah, A.A. Mohamadb, M.Z. Abu Bakar, Trends in modeling of porous media combustion, Progress in Energy and Combustion Science 36 (2010) 627-650

[14] Weclas, M., Cypris, J., Maksoud, T.M.A., Thermodynamic properties of real porous combustion reactor under Diesel engine-like conditions, subm. for publication in Journal of Thermodynamics (in review)

SPLASHING OF WATER DROPLETS ON A TILTED FLOWING LIQUID FILM

He Zhao*, Romain Ecault°, Carlos Alberto Dorao*, Svend Tollak Munkejord°

*Department of Energy and Process Engineering, Norwegian University of Science and Technology (NTNU),
Kolbjørn Hejes vei 1B, 7491 Trondheim, Norway
°SINTEF Energy Research, Sem Sælands vei 11, 7465 Trondheim, Norway

ABSTRACT

An experimental investigation of water droplets impinging with a liquid film of water flowing on a 20°-tilted aluminium board was carried out. The effects of impinging droplet size, velocity and liquid film parameters on splashing were both qualitatively and quantitatively studied and discussed. The evolution of a non-symmetric crown was characterized by investigating the normalized crown height and a non-symmetry factor versus the normalized time, and the breakup of secondary droplets was found influential to the crown evolution. An increase of film velocity and depth reduced the crown height, but it does not affect the non-symmetry factor until the crown started to collapse. Threshold of splashing was investigated, and it was found that the threshold can be well described by the model reported in Ref. [4].

INTRODUCTION

Droplet impacting on a surface was studied since the end of 19th century [1], and there has been a substantial progress in understanding the droplet impact phenomena in the last two decades [2] owing to the development in the technology of high speed camera. Distinguishing different flow regimes was one of the most important purposes due to its contribution to the control of different processes such as fuel injection, inkjet printing, phase separation etc. Such works were related with both high energy impingement corresponding to splashing and jetting and low energy impingement corresponding to bouncing on either a dry surface [3][10] or a liquid-covered surfaces [4][5][8][9]. Another highlighted purpose was to study the evolution process of the droplet impact for establishing models, and such work can also be found for droplets impinging on a dry surface [11] and a liquid-covered surface impact [6].

One aspect in common for most of the droplet impact studies was that the targets on which droplets impacted were immobile, but in some industrial processes this is less likely to be true. One example is annular flow, in which droplets are torn off from and deposit to a flowing liquid film dynamically such as shown in Figure 1. Annular flow models without considering the dynamics of the dispersed phase fail in describing the parameters such as pressure drop, film thickness and heat transfer. This is also the case for other processes where a flowing liquid film and droplets interact with each other. In order to make robust models, one shall understand further the interactions between droplets and a flowing liquid film.

Studies of droplets impacting with a flowing liquid film are, however, found to be inadequate. Initial attempts are made in Ref. [12][13][14], of all which the impact conditions are nearly normal (tilted angle less than 10°, with a horizontal surface defined as 0°). Ref. [12][13] focused on studying the relationship between the size of the crater formed by the impact of the droplet and the dependence of the total volume of secondary drops on the thickness and velocity of the liquid layer, and the slope of the tray. Ref. [14] focused on the transitions of flow regimes, and the critical Weber numbers for characterizing the regime-transitions seem to be independent on both the film thickness and velocity reported in the article. It is thus desired to investigate the impact of droplets on a flowing liquid film with more tilted angles and velocities as to investigate the effects of non-symmetrical impact and liquid film parameters on splashing evolution and transition.

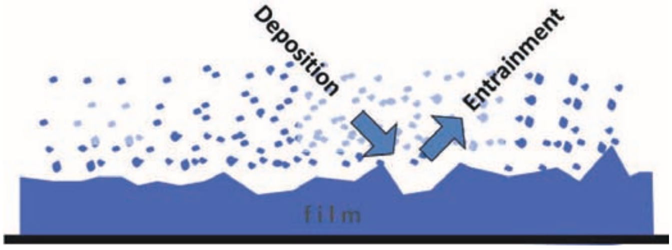

Figure 1 Sketch of annular-mist flow.

EXPERIMENTAL METHODS AND PARAMETERS

Experimental apparatus

Experimental apparatus and methods are to be described in this section. A sketch of the experimental apparatus is shown in Figure 2. A collimated LED was served as a light source. A Phantom V9 digital camera operated at 1255 fps (in most of the acquisitions) with a resolution of 1440×1080 pixels was employed for capturing the droplet-film interactions. A 20°-tilted aluminum board was placed inside a test cell, and a shallow channel, in which a liquid film flowed, was made of one pair of aluminum foil bands. The channel width was 15.5 mm, and depth was decided by the thickness of the aluminum foil, which was about 0.1 mm. A liquid pump circulated water for generating a flowing liquid film. Droplet was generated from a dropper, a needle of gauge 33 (Hamilton). Droplet releasing height was varied in order to have different impinging velocities.

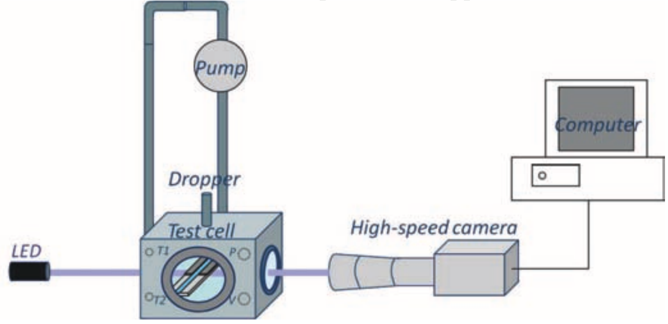

Figure 2 Sketch of experimental apparatus.

Measurement methods and parameters

Droplet diameter and velocity were measured from the captured videos. Diameter was evaluated by using the cross-sectional area of the droplet, and velocity was calculated by using the displacement and time interval. The relative uncertainties for both the diameter and velocity measurements were approximately 3%.

Four flow rates, 1.82×10^{-6}, 3.08×10^{-6}, 4.32×10^{-6}, 6.82×10^{-6} m^3/s were used. Liquid film thickness was evaluated by comparing the image difference with and without a liquid film. The relative uncertainty of the thickness was dependent on the flow rate, and the lowest and highest flow rates (1.82×10^{-6} and 6.82×10^{-6} m^3/s) corresponds to an uncertainty about 10%, while the other two flow rates (3.08×10^{-6}, 4.32×10^{-6} m^3/s) corresponds to an relative uncertainty about 5%.

Surface velocity of the liquid film was measured by tracking polybutylene beads (0.25-0.35 mm), which were set in the upstream of the flow. The relaxation time of the beads (τ_r) was less than 5 ms, which was about 10 times shorter than the time taken for the beads travelling from the released point to the camera focus, and thus, the beads can follow the flow well. The relative uncertainty of the surface velocity for the two lower flow rates (1.82×10^{-6}, 3.08×10^{-6} m^3/s) was about 5%, and was approximately 12% for the other two flow rates (4.32×10^{-6}, 6.82×10^{-6} m^3/s).

Table 1 shows the film parameters, in which the measured quantities are flow rate (Q), thickness (Δ), surface velocity (V_s), and the calculated quantities are mean velocity (V_m) and the film Reynolds number (Re_f) shown by Eq. (1) and Eq. (2).

$$V_m = \frac{Q}{\Delta \cdot W} \tag{1}$$

$$\mathrm{Re}_f = \frac{4\rho Q}{\mu W} \tag{2}$$

Table 1 Liquid film flow rate (Q, m^3/s) and corresponding liquid film thickness (Δ, mm), surface velocity (V_s, m/s), mean velocity (V_m, m/s) and Reynolds number (Re_f).

NO.	Q	Δ	V_s	V_m	Re_f
1	1.82×10^{-6}	0.55	0.37	0.21	528
2	3.08×10^{-6}	0.73	0.47	0.28	893
3	4.32×10^{-6}	0.89	0.55	0.32	1253
4	6.82×10^{-6}	1.20	0.62	0.38	1978

where Q, Δ and W are flow rate, thickness and channel width shown by, where $\rho = 1000$ kg/m^3 and $\mu = 0.89$ mPa·s are density and viscosity of water at 25°C.

EXPERIMENTAL OBSERVATIONS

In this section, we first show typical observations for the non-splashing regime, which is next to the regime of splashing. Secondly, splashing regime is shown, and the effects of droplet parameters, i.e. diameter and velocity, as well as the effects from the liquid film on splashing are described.

Non-splashing

For droplet-pool interactions, the non-splashing regimes can be jetting, coalescence, bouncing and partial coalescence. Jetting, which is adjacent to splashing and characterized by the central jet formation (sometimes breakup) [5][14], is of interest here. Figure 3 shows the typical non-splashing.

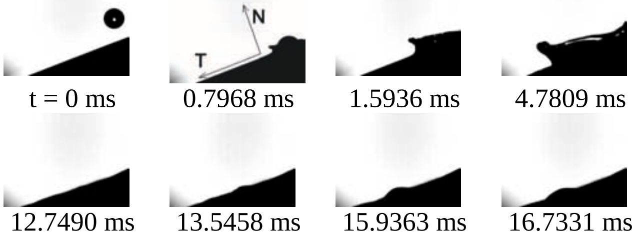

Figure 3 The non-splashing regime adjacent to splashing. Droplet parameters: diameter 2.0 mm, impinging velocity 2.8 m/s. Film parameters: angle 20°, thickness 0.55 mm, surface velocity 0.37 m/s (other parameters see Table 1).

Figure 3 shows that a non-symmetric wave is formed at t = 0.7968 ms. Due to the fact that the tangential (T) velocity of the droplet (≈ 1 m/s) is higher than the film velocity (0.37 m/s), the droplet has a relative motion towards downstream, along the tangential direction, of the liquid film, and thus a higher wave (in the normal direction and relative to the undisturbed film surface thereinafter) can be expected and seen at the downstream side of the impact point. At t = 4.7809 ms, the leading edge of the wave develops to about the maximum height. A primary central jet is initially seen at t = 12.7490 ms, and it reaches its maximum height at approximately t = 15.9363 ms.

Different from the central jet formation with a normal impact, where the central jet appears at the impact point, the central jet formed here moves away from the impact point, and it appears at downstream of the impinging point. This owes to the oblique impact condition and the liquid film motion.

Another remarkable difference between the central jet formation here and that from droplet-pool interactions is that the primary jet does not disintegrate into secondary droplets. Ref. [16][17] reported no central jet formation for splashing on thin films (dimensionless film thickness $\Delta^* = \Delta / D$ less than 0.125, where D is diameter of droplet), and Ref. [17] proposed the reasons 1. Crown breaking led to energy loss. 2. No cavity collapse. With thicker films (Δ^* approx. 0.3~0.6) presented in this investigation, the primary jet is observed without breaking up. We suggest that ability of focusing the receding wave as to form and break up the central jet here is weaker than in the case of droplet-pool interaction due to two reasons: 1. Shallow film - unlike the impact on a pool, where an undisturbed crater is formed and collapses naturally, the crater formation is interrupted by an unyielding surface, and the wave expands radially, which reduces the mass focusing during receding. 2. Non-symmetric wave - the tilted surface and film movement form a non-symmetric wave, with which the ability of focusing the receding mass is weaker than with a more symmetric wave.

Splashing with different impinging velocities

In this part, the effect of the impinging velocity on splashing is to be examined with fixed film parameters and a fixed impinging droplet size. Figure 4 and Figure 5 show the impacts with the same droplet diameter (2.0 mm) and film parameters (angle 20°, thickness 0.55 mm, surface velocity 0.37 m/s, other parameters see Table 1) but with different impinging velocities.

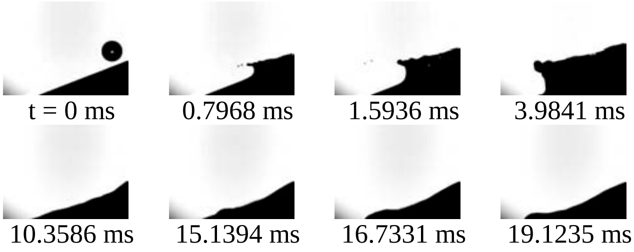
t = 0 ms
0.7968 ms
1.5936 ms
3.9841 ms
10.3586 ms
15.1394 ms
16.7331 ms
19.1235 ms

Figure 4 Splashing with impinging droplet diameter 2.0 mm, velocity 3.4 m/s.

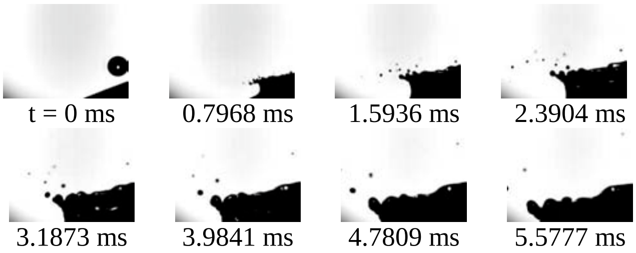
t = 0 ms
0.7968 ms
1.5936 ms
2.3904 ms
3.1873 ms
3.9841 ms
4.7809 ms
5.5777 ms

Figure 5 Splashing with impinging droplet diameter 2.0 mm velocity 3.9 m/s.

Comparing the first row of Figure 4 with Figure 5, one can readily see the differences that an increased velocity makes – more released secondary droplets from the crown breakup and also higher evoked crown height. It can also be seen that the released secondary droplets in Figure 5 have greater velocity components in the normal direction than the two released secondary droplets shown in Figure 4.

Figure 4 shows that the maximum crown height (of the leading edge thereinafter) is reached at around t = 3.9841 ms, and in Figure 5, the maximum crown height is reached at t = 4.7809~5.5777 ms, which is 1-2 frames delayed compared to the lower velocity case. This is because that all the secondary droplets in Figure 4 are formed at a time-point (t = 0.7968 ms, defined as single-stage breakup), which should be noted that this is not the exact moment due to the non-continuity of the picture-taking but shall be characterized by a certain frame in a video, while in Figure 5, secondary droplets are released at multiple time-points (t = 0.7968, 1.5936 and 3.1873 ms, defined as multi-stage breakup). The multi-stage breakup leads to the postponement of reaching the maximum crown height.

Figure 4 also shows that a primary central jet is initially seen at approximately t = 10.3586 ms and reaches its maximum height at about t = 19.1235ms, and this time is dramatically longer than the jetting case shown in Figure 3 (at t = 15.9363 ms). Therefore, time required for reaching the maximum jetting height is prolonged in the splashing case perhaps due to the breakup of secondary droplets.

Splashing with different impinging drop sizes

In this section, we shall examine the effects of varying droplet size on splashing with fixed film parameters the same as in the above section and a fixed impinging velocity at 3.9 m/s. Figure 5 will be referred as the splashing with a larger droplet diameter (2.0 mm), and Figure 6 shows a splashing with a lower droplet diameter (1.6 mm).

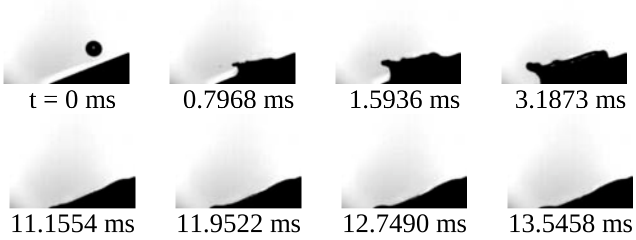
t = 0 ms
0.7968 ms
1.5936 ms
3.1873 ms
11.1554 ms
11.9522 ms
12.7490 ms
13.5458 ms

Figure 6 Splashing with impinging droplet diameter 1.6 mm and velocity 3.9 m/s.

It is obvious that a smaller droplet leads to the single-stage breakup of crown with less secondary droplets generation. The time for reaching the maximum crown height is at about t = 3.1873 ms, which is earlier than that in the splashing with multi-stage breakup in Figure 5.

Splashing with different film parameters

Effects of film parameters on splashing will be illustrated in this section, and Figure 5 will be employed to show the splashing with a liquid film flowing at a lower flow rate (thickness 0.55 and surface velocity 0.37 m/s). Figure 7 shows a splashing with the same impinging droplet diameter and velocity as those listed in Figure 5 but on a film with a higher flow rate (thickness 1.20 and surface velocity 0.62 m/s).

t = 0 ms 0.9843 ms 1.9685 ms 5.9055 ms

Figure 7 Splashing with film number 4: angle 20°, thickness 1.20 mm, surface velocity 0.62 m/s (other parameters see Table 1), droplet diameter and velocity are the same as those listed in Figure 5.

Figure 7 shows that the crown height is lower than that shown in Figure 5. Another noticeable difference is that the leading edge of the crown is more stretched towards the tangential direction as shown by the "filaments" at t = 0.9843 and 1.9685 ms.

The time required to reach the maximum crown height is at about t = 5.9055 ms, which is slightly delayed but not largely different from that in Figure 5, as both of the splashing cases experience multi-stage breakup.

EXPERIMENTAL ANALYSIS

Quantitative analysis of the impact evolutions

In this section, we shall analyze the crown height evolution of splashing. The normalized height of the leading edge of the crown (H_1^*) and the non-symmetry factor of the crown (S) as shown in Figure 8 are studied with the normalized time (t^*),

$$H_1^* = \frac{H_1}{D} \tag{3}$$

$$S = \frac{H_1}{H_2} \tag{4}$$

$$t^* = \frac{t \cdot V_n}{D} \tag{5}$$

where t and V_n are elapsed time and normal component of impinging velocity.

Figure 9 shows the crown development for splashing on a flowing liquid film (angle 20°, thickness 0.55 mm, surface velocity 0.37 m/s, other parameters see Table 1).

Figure 8 Sketch of splashing heights of leading edge (H_1) and trailing edge (H_2).

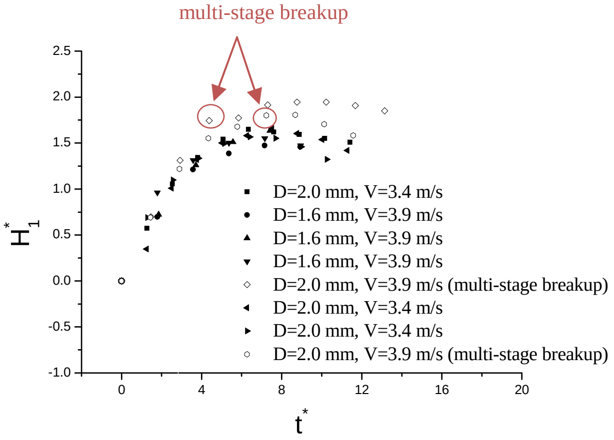

Figure 9 Crown evolution of splashing on a flowing liquid film (No. 1 in Table 1): effect of multi-stage breakup.

Figure 9 shows that crown evolutions with single-stage breakup follow nearly the same path, while the crown evolutions with multi-stage breakup deviate from that path at the moment that multi-stage breakup is formed. Due to the multi-stage breakup, a delayed maximum crown height is obtained. It can also be noted that the earlier multi-stage breakup tends to maintain the crown height at maximum, while the crown height drops faster in the case with the later multi-stage breakup during the collapse of crown.

Figure 10 illustrates the non-symmetry factor during the crown evolutions. As can be seen from the figure, this factor is maintained at about $S = 2$ while the crown height is growing (approx. for $t^* < 10$), and it increases fast as the crown starts to collapse. It reveals that the leading edge and trailing edge grow with a similar scale, while the trailing edge collapses with a larger scale.

Figure 11 shows the crown evolution for splashing on a flowing liquid film with a higher flow rate (angle 20°, thickness 1.20 mm, surface velocity 0.62 m/s, other parameters see Table 1), and the data shown in Figure 9 is plotted with grey colour. It is obvious that the increase of liquid film velocity and depth leads to a lower crown height formation. Multi-stage breakup is also observed, and it behaves in the similar way which makes the evolutionary curves of crown height deviate from the splashing with single-stage breakup.

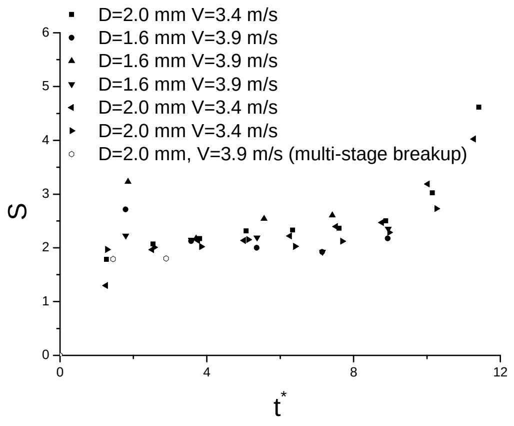

Figure 10 Non-symmetry factor of splashing on a flowing liquid film (No. 1 in Table 1).

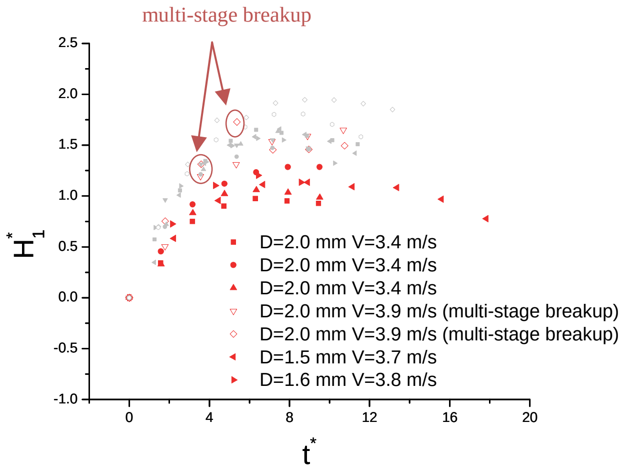

Figure 11 Crown height evolution of splashing on a flowing liquid film (No. 4 in Table 1), and grey symbols present the crown height evolution shown in Figure 9.

Figure 12 shows the non-symmetry factor for splashing on a flowing liquid film (angle 20°, thickness 1.20 mm, surface velocity 0.62 m/s, other parameters see Table 1), and the data shown in Figure 10 is plotted in grey colour. Little difference is seen between the non-symmetry factors of splashing on the two films during the crown height increase (approx. for $t^* < 10$), while the non-symmetry factor for the flowing film with a higher velocity and depth tends to continually stay at around $S = 2$ during the collapse of crown.

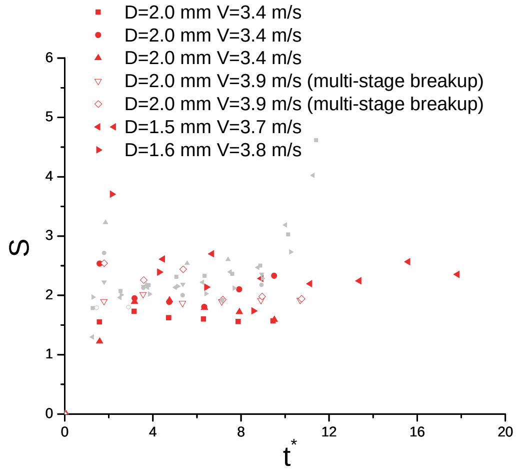

Figure 12 Non-symmetry factor of splashing on a flowing liquid film (No. 4 in Table 1), and grey symbols present the non-symmetry factor shown in Figure 10.

Splashing threshold

In the analysis of the threshold between splashing and jetting, only the data of splashing and jetting is of interest. The Ohnesorge number ($Oh = \mu / (\rho\sigma D)$, $\sigma = 72$ mN/m denotes the surface tension of water) range in the present investigation is $Oh \in [0.0023, 0.0036]$, and the dimensionless thickness is $\Delta^* \in [0.2, 0.9]$. Both of the parameters were comparable with the experiments of water in Ref. [4], which presented a model (6) for the critical Weber number (We_c), which distinguishes splashing and non-splashing.

$$We_c = \frac{2100 + 5880 \cdot \Delta^{*1.44}}{Oh^{-0.4}} \tag{6}$$

In the present investigation, the impact of droplets on to a 20°-tilted board was close to the normal impact condition regarding the comparison between the normal vector and the composite vector of the impinging Weber number. With a 20°-tilted board, the ratio between the normal vector ($We_{c,n}$) and the composite vector (We_c) of the critical Weber number is as follows.

$$\frac{We_{c,n}}{We_c} = \sin^2 70^\circ \approx 0.9 \tag{7}$$

Thus, if the motion of the liquid film is assumed to be not influential under the quasi-normal impact condition, the critical Weber number for a 20°-tilted board should be close to the critical Weber number predicted for a horizontal film-covered surface in Ref. [4].

Figure 13 shows the Weber number against the dimensionless thickness of the flowing liquid film. For comparison, the critical Weber number calculated using model (6) is plotted in the figure.

Figure 13 shows that the threshold of splashing and jetting for droplets impinging with a 20°-tilted board is, in general, well characterized by model (6). In fact, the threshold fits better the calculated value for $\Delta^* < 0.5$, and the experimental thresholds become to be overestimated by the model as dimensionless thickness increases. This agrees well with Ref. [4], in which the agreement between the model and experimental results is better for $\Delta^* < 0.3$ than for $\Delta^* > 0.5$, where the calculated threshold starts to be overestimated. Thus, the assumption is true that the effects of the liquid film motion on the threshold of splashing are not obviously seen for droplets impinging with a tilted flowing liquid film with a quasi-normal impact condition such as the 20° board inclination in the present study.

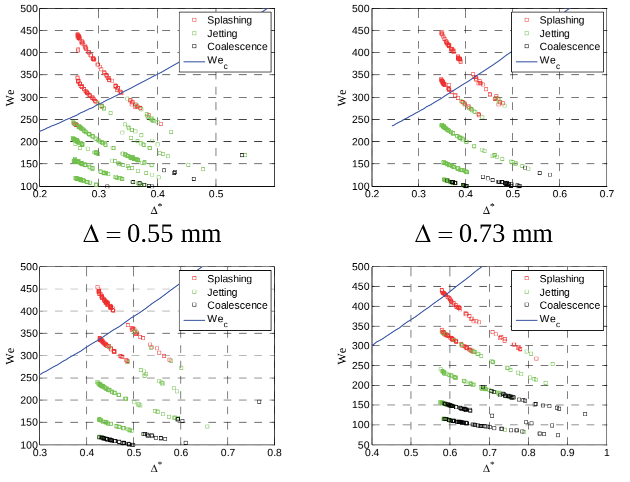

$\Delta = 0.55$ mm

$\Delta = 0.73$ mm

$\Delta = 0.89$ mm

$\Delta = 1.20$ mm

Figure 13 Weber number (We) versus dimensionless thickness (Δ^*) with comparison to the critical Weber number (We_c) calculated using model (6).

CONCLUDING REMARKS

An experimental investigation of water droplets impinging with a liquid film of water flowing on a 20°-tilted board was made with the focus on splashing evolution and threshold. The investigation showed that, for a given liquid film, an increase in either droplet diameter or velocity resulted in more secondary droplets from crown breakup. The crown evolutions with single-stage breakup followed a similar path, while those with multi-stage breakup deviated from this path with higher crown heights and delays in reaching the maximum crown heights. An increase in the film velocity and depth led to lower crown height.

The non-symmetric crown was characterized by a non-symmetry factor S , which was steady ($S \approx 2$) during the crown growing and increased during the crown collapse for a thin and slow-flowing film (NO. 1 in Table 1). With a thicker and faster-flowing film (NO. 4 in Table 1), this factor tended to maintain stable ($S \approx 2$) throughout both the crown growing and collapse.

The impact condition in this investigation was quasi-normal, and little difference in the splashing threshold from the normal impact was noticed as the critical Weber numbers can be well characterized by using the model (6) presented in Ref. [4]. However, the threshold model became less robust as the normalized film thickness is above 0.5.

ACKNOWLEDGMENT

This publication is based on results from the research project Enabling low emission LNG systems, performed under the Petromaks program. The authors acknowledge the project partners; Statoil and GDF SUEZ, and the Research Council of Norway (193062/S60) for support.

NOMENCLATURE

Symbol	Quantity	SI Unit
Δ	Film thickness	m
Δ^*	Dimensionless film thickness	
μ	Viscosity of water	Pa·s
ρ	Density of water	kg/m^3
σ	Surface tension of water	N/m
τ_r	Relaxation time	s
D	Droplet diameter	m
H_1	Crown height, leading edge	m
H_1^*	Dimensionless crown height, leading edge	
H_2	Crown height, trailing edge	m
Oh	Ohnesorge number	
Q	Flow rate	m^3/s
Re_f	Film Reynolds number	
S	Non-symmetry factor	
t	Elapsed time	s
t^*	Dimensionless time	
V	Impinging velocity	m/s
V_f	Film velocity	m/s
V_m	Mean velocity of film	m/s
V_n	Normal component of impinging velocity	m/s
V_s	Surface velocity of film	m/s
W	Width of channel	m
We	Weber number	
We_c	Critical Weber number	
$We_{c,n}$	Normal component of critical Weber number	

REFERENCES

[1] A.M. Worthington, On the Forms Assumed by Drops of Liquids Falling Vertically on a Horizontal Plate, *Proc. R. Soc. Lond.*, vol. 25, pp. 261-272, 1876.

[2] A.L. Yarin, Drop Impact Dynamics: Splashing, Spreading, Receding, Bouncing…, *Annu. Rev. Fluid Mech.*, vol. 38, pp. 159-192, 2006.

[3] C. Mundo, M. Sommerfeld and C. Tropea, Droplet-Wall Collisions: Experimental Studies of the Deformation and Breakup Process, *Int. J. Multiphase Flow*, vol. 21 (2), 151-173, 1995.

[4] G.E. Cossali, A. Coghe and M. Marengo, The Impact of a Single Drop on a Wetted Solid Surface, *Exp. Fluids*, vol. 22, pp. 463-472, 1997.

[5] H. Zhao, A. Brunsvold and S.T. Munkejord, Investigation of Droplets Impinging on a Deep Pool: Transition from Coalescence to Jetting, *Exp. Fluids*, vol. 50 (3), pp. 621-635, 2011.

[6] A. Bisighini, G.E. Cossali, C.Tropea and I.V. Roisman, Crater Evolution after the Impact of a Drop onto a Semi-infinite Liquid Target, *Phys. Rev. E*, vol. 82 (3), pp. 036319, 2010.

[7] F. Blanchette and T.P. Bigioni, Partial Coalescence of Drops at Liquid, *Nat. Phys.*, vol. 2, pp. 254-257, 2006.

[8] K.L. Pan and C.K. Law, Dynamics of Droplet-Film Collision, *J. Fluid Mech.*, vol. 587, pp. 1-22, 2007.

[9] H. Zhao, A. Brunsvold and S.T. Munkejord, Transition between Coalescence and Bouncing of Droplets on a Deep Liquid Pool, *Int. J. Multiphase Flow*, 2011, Accepted.

[10] D. Bartolo, F. Bouamrirene, É. Verneuil, A. Buguin, P. Silberzan and S. Moulinet, Bouncing or Sticky Droplets: Impalement Transitions on Superhydrophobic Micropatterned Surfaces, *Europhy. Lett.*, vol. 74 (2), pp. 299, 2006.

[11] Š. Šikalo and E.N. Ganića, Phenomena of Droplet–Surface Interactions, *Exp. Therm. Fluid Sci.*, vol. 31 (2), pp. 97-110, 2006.

[12] V.G. Sister, O.A. Eliseeva, and A.K. Lednev, Study of the Features of Impact Reaction of a Droplet with a Liquid Surface, *Chem. Pet. Eng.*, vol. 45 (5-6), pp. 271-274, 2009.

[13] V.G. Sister, O.A. Eliseeva, and A.K. Lednev, Formation of Secondary Drops upon Collision of a Drop with a Liquid Surface, *Chem. Pet. Eng.*, vol. 45 (7-8), pp. 473-477, 2009.

[14] S.K. Alghoul, C.N. Eastwick and D.B. Hann, Normal Droplet Impact on Horizontal Moving Films: an Investigation of Impact Behaviour and Regimes, *Exp. Fluids*, vol. 50 (5), pp. 1305-1316, 2011.

[15] S.K. Alghoul, C.N. Eastwick and D.B. Hann, Normal Droplet Impact on Horizontal Moving Films: an

Investigation of Impact Behaviour and Regimes, *Exp. Fluids*, vol. 50 (5), pp. 1305-1316, 2011.

[16] D.A. Weiss and A.L. Yarin, Single Drop Impact onto Liquid Films: Neck Distortion, Jetting, Tiny Bubble Entrainment, and Crown Formation, *J. Fluid Mech.*, vol. 385, pp. 229-254, 1999.

[17] A.B. Wang and C.C. Chen, Splashing Impact of a Single Drop onto Very Thin Liquid Films, *Phys. Fluids*, vol. 12 (9), pp. 2155-2158, 2000.

Author index

ISBN - 978 88 97413 03 5